ARCHITECTURALLY DEFINED SCAFFOLDS FROM SYNTHETIC COLLAGEN AND ELASTIN ANALOGUES FOR THE FABRICATION OF BIOENGINEERED TISSUES

A Dissertation
Presented to
The Academic Faculty

by

Jeffrey Morris Caves

In Partial Fulfillment
of the Requirements for the Degree
Doctor of Philosophy in Bioengineering

Georgia Institute of Technology
December 2008

ARCHITECTURALLY DEFINED SCAFFOLDS FROM SYNTHETIC COLLAGEN AND ELASTIN ANALOGUES FOR THE FABRICATION OF BIOENGINEERED TISSUES

Approved by:

Dr. Elliot Chaikof, Advisor
The Wallace H. Coulter Department of Biomedical Engineering
Georgia Institute of Technology
Department of Surgery
Emory University School of Medicine

Dr. Ajit Yoganathan
The Wallace H. Coulter Department of Biomedical Engineering
Georgia Institute of Technology

Dr. Mark Allen
School of Electrical and Computer Engineering
Georgia Institute of Technology

Dr. Marc Levenston
Department of Mechanical Engineering
Stanford University

Dr. Larry McIntire
The Wallace H. Coulter Department of Biomedical Engineering
Georgia Institute of Technology

Date Approved: October 22, 2008

ACKNOWLEDGEMENTS

I would like to thank my research advisor and the members of the thesis reading committee for the guidance, comments, and inspiration that have shaped this project into much more than it might have been. I would also like to thank the members Laboratory of Bio/Molecular Engineering and Advanced Vascular Technologies for the advice, assistance, effort, and camaraderie. Numerous other caring and diligent individuals at Georgia Tech and Emory University have contributed generously.

My spouse, Diane, has shown the utmost supportiveness, good cheer, and tolerance before and throughout my tenure in graduate school. My siblings, parents, and grandparents deserve enormous credit for laying the foundation upon which this work could be achieved, and for celebrating those periods when work was not achieved at all.

My role in this research was financially supported by a National Science Foundation Graduate Research Fellowship, and by the Technological Innovation: Generating Economic Results (TI:GER) program at Georgia Tech and Emory University.

TABLE OF CONTENTS

LIST OF TABLES

LIST OF FIGURES

LIST OF SYMBOLS AND ABBREVIATIONS

ΔH	Apparent enthalpy
μDSC	Micro-differential scanning calorimetry
T_m	Apparent temperature of melting
AC	Automatically collected fiber
AC-FIB	Automatically collected fiber treated with fiber incubation buffer
AC+FIB	Automatically collected fiber not treated with fiber incubation buffer
AC+FIB+GLUT	AC+FIB crosslinked with glutaraldehyde
DMSO	Dimethyl sulfoxide
DMTA	Dynamic mechanical thermal analyzer
DVI	Digital volumetric imaging
FIB	Fiber incubation buffer
F/B	Forward-to-backward ratio in second harmonic generation experiments
HCl	Hydrochloric acid
HE	Hematoxylin eosin stain
ICP	Inductively coupled plasma
KOH	Potassium hydroxide
LSM	Laser scanning microscopy
MC	Manually collected fiber
MC-0%, MC-15%, MC-30%	Manually collected fiber with an applied strain during mechanical annealing
MRTC	Monomeric rat tail tendon collagen
MLU	Medial lamellar unit

NaCl	Sodium chloride
PBS	Phosphate buffered saline
PDMS	Polydimethylsiloxane
PEG	Poly(ethylene glycol)
PFCS	Protien fiber composite sheet
PU	Polyurethane
PVC	Poly(vinyl chloride)
RTT	Rat tail tendon
SHG	Second harmonic generation
SEM	Scanning electron microscopy
TRITC	Tetramethylrhodamine isothiocyanate
WSB	Wet spinning buffer
UTS	Ultimate tensile strength

SUMMARY

The microstructure and mechanics of collagen and elastin protein fiber networks dictate the mechanical responses of all soft tissues and related organ systems. In this project, we endeavored to meet or exceed native tissue biomechanical properties through mimicry of these extracellular matrix components with synthetic collagen fiber and a recombinant elastin-like protein polymer. Significantly, this work led to the development of a framework for the design and fabrication of protein-based tissue substitutes with enhanced strength, resilience, anisotropy, and more.

We began with the development of a spinning process for scalable production of synthetic collagen fiber. Fiber with an elliptical cross-section of 53 ± 14 by 21 ± 3 μm and an ultimate tensile strength of 90 ± 19 MPa was continuously produced at 60 meters per hour from an ultrafiltered collagen solution. The starting collagen concentration, flowrate, and needle size could be adjusted to control fiber size. The fiber was characterized with mechanical analysis, micro-differential scanning calorimetry, transmission electron microscopy, second harmonic generation analysis, and subcutaneous murine implant.

We subsequently describe the scalable, semi-automated fabrication of elastin-like protein sheets reinforced with synthetic collagen fibers that can be positioned in a precisely defined three-dimensional hierarchical pattern. Multilamellar, fiber-reinforced elastic protein sheets were constructed with controlled fiber orientation and volume fraction. Structures were analyzed with scanning electron microscopy, transmission electron microscopy, and digital volumetric imaging. The effect of fiber orientation and

volume fraction on Young's Modulus, yield stress, ultimate tensile stress, strain-to-failure, and resilience was evaluated in uniaxial tension. Increased fiber volume fraction and alignment with applied deformation significantly increased Young's Modulus, resilience, and yield stress.

Highly extensible, elastic tissues display a functionally important mechanical transition from low to high modulus deformation at a strain dictated by the crimped microstructure of native collagen fiber. We report the fabrication of dense arrays of microcrimped synthetic collagen fiber embedded in elastin-like protein lamellae that mimic this aspect of tissue mechanics. Microcrimped fiber arrays were characterized with scanning electron microscopy, confocal laser scanning microscopy, and uniaxial tension analysis. Crimp wavelength was 143 ± 5 μm. The degree of crimping was varied from 3.1% to 9.4%, and corresponded to mechanical modulus transitions at 4.6% and 13.3% strain. Up to 1000 cycles of tensile loading did not substantially alter microcrimp morphology.

We designed and prototyped a series of small-diameter vascular grafts consisting of elastin-like protein reinforced with controlled volume fractions and orientations of collagen fiber. A pressure-diameter system was developed and implemented to study the effects of fiber distribution on graft mechanics. The optimal design satisfied target properties with suture retention strength of 173 ± 4 g-f, burst strength of 1483 ± 143 mm Hg, and compliance of 5.1 ± 0.8 %/100 mm Hg.

INTRODUCTION

OBJECTIVE, CENTRAL HYPOTHESIS, and SPECIFIC AIMS

The objective of this project was to combine collagen fiber and a recombinant elastin-like protein to fabricate composite structures with mechanical properties appropriate for heart valve leaflet and vascular graft substitutes. Our central hypothesis was that by mimicking the constituent materials and structure and of native soft tissues, we could meet or exceed the mechanical responses of those tissues. The specific aims of the project were:

Specific Aim 1. Develop a method for the scalable manufacture of collagen fibers that approximate the structure of native fiber, with mechanical properties sufficient for use as a reinforcing element in tissue substitute. Motivated by the pervasive mechanical role of collagen fiber in soft tissues, we sought to create fiber using a modified wet spinning approach. Although a variety of methods of collagen fiber production have been explored, a simple, scalable means to generate continuous fiber with the banded fibrillar ultrastructure of native fibrous collagen was not available. The development of our approach is described in Chapter 2.

Specific Aim 2. Fabricate and characterize anisotropic protein polymer lamellar elastic structures (APPLES) for potential application to heart valve leaflet. Our first concept for heart valve leaflet replacement consisted of ten-layer laminates of recombinant, elastin-mimetic protein polymer reinforced with oriented collagen fiber. Chapter 3 describes the fabrication, structural analysis, mechanical analysis, and of several flexible composite designs with varying fiber volume fraction and orientation. In

Chapter 4, a microcrimping technique is developed to enhance the compliance of the flexible composite sheets.

Specific Aim 3. Fabricate and evaluate the mechanics of small-diameter vascular grafts from elastin-mimetic protein reinforced with collagen fiber. This aim is addressed in Chapter 5.

BACKGROUND

Our central hypothesis can be restated as the concept of biomimetics applied to the development of soft tissue substitutes that mimic or expand upon the biomechanics of the extracellular matrix. We hypothesized that because the key non-living constituents of these structures are fibrous networks of collagen and elastin, it may be possible to fabricate suitable artificial structures from fibrous collagen and elastin analogue materials. As a first step, we proposed to investigate the fabrication of structures without living cells. The elastin analogs, elastin-mimetic triblock copolymers, were previously reported [1] and have been a topic of continuing research [2-6]. A suitable analogue for the fibrous collagen component of soft tissues was not available; the first part of this project was therefore the development of artificial collagen fiber. To provide additional background, the structure and mechanics arteries and heart valve leaflet, the application of collagen as a biomaterial, and the properties of elastin-mimetic triblock copolymers are briefly described below.

The elasticity and structure of arteries. The arterial side of the circulatory system carries blood from the heart to the tissues of the body. To perform this role smoothly, continuously, and efficiently, arteries act as both conduits and pressure reservoirs. As the left ventricle contracts, arteries expand under pressure, and as the

ventricle relaxes, arterial diameters recoil. Thus, arteries are compliant tubes that elastically absorb a portion of the energy from ventricular contraction, and return this energy to aid in blood circulation when the ventricle relaxes. This role is most pronounced in the aortic arch, which has been described as the "auxiliary pump" of the circulatory system [7]. The central arteries are precisely tapered along the length of the aortic arch, thoracic aorta, and abdominal aorta and in terms of decreasing size and increasing stiffness. The taper appears to result in destructive interference between outgoing and reflected pressure waves, further smoothing pressure and reducing the load on the heart [8, 9].

The arterial wall is a laminated structure, consisting of the inner *tunica intima* followed by the *tunica media*, and the *tunica adventitia*. The intima is only 0.2 – 2 μm thick. In many arteries, the intima consists of a single layer of endothelial cells supported by the basil lamina, a collagenous layer. In some arteries, the intima includes more connective tissue and some smooth muscle cells. By mass, the aortic intima is reported to be 65% water, 16% type I collagen, 8% type III collagen, 5% cellular components, and lesser amounts of other collagens and proteoglycans [7].

The intimal layer is followed by an elastic sheet, the internal elastic lamina, and then by the media. Of the three layers, the media contributes the most to arterial mechanics. The structure-function units of the media are concentrically arranged sheets termed medial lamellar units (MLU). The MLU of the mammalian aorta has been studied most extensively. An aortic MLU is a ~15 μm thick sheet consisting of one or occasionally two layers of smooth muscle cells surrounded by dense sheets of elastic fibers. The elastic sheet boundaries of the MLU appear severely wrinkled when cross-

sections are taken in the absence internal pressure. However, when vessels are fixed under a small amount of internal pressure, below physiologic pressure, the vessel diameter expands considerably, the wall thins, and the elastic sheets become smooth concentric arcs [10]. Close examination reveals that the elastic layers demarcating two MLU are double layers; one layer is associated with each MLU. Bundles of collagen fibers run between the MLU. Collagen bundles tend follow a wavy or helical path even when fixed at physiologic pressures that eliminate the wrinkled path of the elastic layer. Most of the bundles run circumferentially around the aorta, within plus or minus about 5˚. All bundles associated with a particular MLU are essentially parallel; variability in orientation is thought to be between rather than within the MLU. In smaller aortas, such as the rat and immature rabbit, a single MLU can wrap entirely around the circumference of the vessel to form a ring. In larger animals such as pigs, a single MLU attains a maximal circumferential length of 4 to 5 mm, and does not encircle the entire aorta [11]. The width of an MLU, measured along the axis of the aorta, varies with vessel and animal size from 100-200 μm in the rabbit to 1-3 mm in the pig. At bend or branch points in the vessel, the concentric MLU layout is abandoned for more complex structural arrangements [11].

The aortic MLU is considered a functional unit because it is specialized to bear a tension of 1.1 to 3.0 N/m in most mammals [12]. This calculation was motivated by the observations that (i) the aortic MLU thickness is roughly constant, and (ii) the thickness of the aortic media is closely related to aortic diameter and total wall tension. Therefore, when total wall tension is divided by number of MLU through the thickness of the media, a roughly constant tension per MLU results. Consequently, the rat aorta has an average

of approximately 5 MLU layers while the sow has 72, corresponding to their different aortic wall tensions [13]. The difference in wall tension is directly related to the difference in vessel diameter.

A recent study using serial block-face scanning election microscopy to examine rat abdominal aorta MLU has permitted enhanced structural resolution and volume calculations [14]. These estimates revealed that the MLU volume was 29% elastin, 24% smooth muscle cell, and 47% collagen and ground substance. Of the elastin, 71% was part of the lamellar sheets, 27% occurred as fine fibers protruding into the MLU, and 2% as thick radial struts spanning between the lamellar sheets. Smooth muscle cells inside the MLU were encased in cages of thin elastic fibers. The cell nuclei were elliptical, aligned circumferentially, but tilted 20˚ in the radial direction. The cytoplasm shape was highly irregular. Collagen was present between elastic layers in dense, parallel, coiled bundles of 24 ± 15 fibers, and as thinner bundles and single fibers. Within the MLU collagen fibers were closely associated with the smooth muscle cell nucleus.

After a final elastin sheet, the external elastic lamina, comes the adventitial layer. The adventitia is largely a collagen fiber network, but also contains fibroblasts, elastin, and the vessels the supply blood to the arterial tissue, the vasa vasorum.

Arterial structure and composition varies substantially throughout the vascular tree. The largest central vessels are elastic arteries, which tend to be more compliant, contain more elastin in the media, and a relatively small adventitia. The next group includes the carotid, coronary, iliac, and brachial arteries and others, known as the muscular arteries. These contain more smooth muscle cells in the media and a

proportionally larger adventitia. The smallest arteries are the arterioles, which contain abundant smooth muscle, but less elastin, except for a thick internal elastic lamina.

The mechanics and structure of aortic valve leaflets. The three leaflets of the aortic valve are thin, semi-circular tissues. The thickness of the human aortic leaflet varies significantly, from the central belly region, which is approximately 0.250 mm, to the Node of Arantius, approximately 1.330 mm thick [15]. The functional implications of thickness are significant because the flexural rigidity of the leaflet is closely tied to thickness. The leaflet consists of three distinct tissue layers, the ventricularis, spongiosa, and fibrosa. The central spongiosa is a loose, semifluid layer thought to facilitate shear deformation between the other two layers [16]. Because the spongiosa is largely water and glycosaminoglycans (GAGs), it cannot bear significant mechanical loads [17]. The fibrosa layer, termed the "backbone of the leaflet," contains some elastin [18], but consists predominantly of crimped collagen fibers running in a circumferential direction [16]. In addition, the fibrosa is textured with macroscopic wrinkles, or corrugations, so the aortic face of the leaflet is quite rough. The ventricularis layer is thinner than the fibrosa, but contains significantly more elastin. The layer is not ridged or wrinkled, making the ventricular side of the leaflet much smoother than the aortic side. The layer is contiguous with the endocardial lining of the left ventricle [17].

The leaflets stretch dramatically during normal function: surface area increases by up to 50% when the valve closes. The strain is anisotropic, with typical strains of 9% in the circumferential direction and 24% in the radial direction [17]. The large radial stretching during valve closure allows significant areas of contact, or coaptation, between neighboring leaflets. These areas can be up to 40% of total leaflet area [19]. When the

valve is closed, the leaflets must withstand about 100 mmHg of pressure, and coaptation areas play a stabilizing role. They also seal the valve against backflow. Importantly, initial radial stretching occurs with relatively little stress, but as stretching continues the leaflet stiffness sharply increases. This increase occurs at a level of strain known as the transition point. Higher stiffness prevents further deformation, stabilizing the leaflet against prolapse. When the valve opens, much of the leaflet strain is recovered. Recovery of strain diminishes leaflet area, opens a wide orifice for flow, and prevents the development of sharp folds or wrinkles in the leaflet. Therefore, it is accepted that leaflet stretch facilitates a highly stable position during valve closure, and recovery of stretch permits smooth, non-obstructive opening [19, 20]. In summary, leaflet anisotropy and the characteristic transition point strains are the salient features revealed in tensile tests of leaflets. In addition to this behavior in tension, bending behaviors and elasticity are important features of valve mechanics.

Many elements of leaflet mechanics may be traced to tissue microstructure. First, anisotropy is caused by the circumferential orientation of collagen fibers and the macroscopic wrinkles in the fibrosa. Collagen orientation makes the leaflet stiff in the circumferential direction and compliant in the radial direction, while the macroscopic wrinkles increase radial compliance because they are positioned to unfurl as the leaflet stretches in the radial direction [19]. Second, elasticity of the leaflet is mostly attributed to the elastin-rich ventricularis [21]. In the unstressed leaflet, the fibrosa is actually pre-stressed in compression and the ventricularis is in tension [22]. This observation strongly suggests that the ventricularis functions to elastically retract the fibrosa after the leaflet is extended. Third, transition point behavior is related to microstructural features such as

the crimp of the collagen fibers. Crimp allows the fibers to stretch easily during initial deformation, but resist further deformation as they are pulled taut. In addition to the collagen crimp, realignment of the collagen fibers during deformation also contributes to the increased stiffness. Fourth, during flexure, the laminated structure of the leaflet is important. Slippage, or shear deformations, between layers is facilitated by the spongiosa, and prevents the accumulation of large compressive stresses near the concave surface as the leaflet bends [23].

Networks of collagen and elastin proteins act in concert to bear leaflet stress and permit deformation. Elastin is highly compliant and capable of relatively large deformations. Therefore, it is associated with leaflet strain before the transition point, when substantial deformation occurs and the mechanical modulus is very low. Collagen is relatively stiff and inextensible, so it is associated with the stiffening of the leaflet [24]. Microscopic observations suggest that elastin fibers and sheets surround and connect the collagen fiber bundles [18]. The close association between elastin and collagen suggests elastin recruits collagen fiber bundles as the tissue approaches transition point strain. During recovery of deformation, the elastin network functions to recoil the collagen fiber network into its relaxed, slightly compressed, state [18]. Broom referred to this mechanism as a *complementary* system because the two fiber networks seem evolved to share stresses and transfer loading, generating highly specialized mechanical behavior. Broom also noted that collagen, like elastin, is an elastic material. Although elastin is probably mostly responsible for elastic recoil below the lock-up strain, collagen contributes elasticity at high strains [24]. These observations all confirm that, in addition

to the mechanical properties of the constituent materials, the three-dimensional microstructure of the two fiber networks determines leaflet mechanical response.

Fibrillar collagen as a biomaterial. The collagens are a family of at least 19 proteins characterized by triple helical macromolecular structure and by the structural role they play in the extracellular matrix (ECM) [25]. The collagen types are most broadly categorized as fibril forming and non-fibril forming, and further differentiated by specific functions and tissue distributions. Collagens consist of three amino acid chains, the α-chains. To assume triple helical structure, the α-chains each coil in a left-handed helix and simultaneously coil about one another in a right-handed super helix. The α-chains may be identical or distinct, but generally consist of the Gly-X-Y repeated amino acid sequence, where X and Y are frequently hydroxylated lysine and proline residues. Many of the prolines and lysines are enzymatically hydroxylated after the α-chains have been transcribed but before formation of triple helical structure. Following hydroxylation and in some cases additional modifications, triple helical fibrillar collagen monomers are secreted into the extracellular space as procollagens. After secretion, propeptides regions are cleaved and the collagen monomers self-assembly into fibrils and are ezymatically crosslinked [25]. Type I collagen is the most abundant fibrillar collagen; often when the collagen type is not specified, type I is implied.

The available methods to extract type I collagen from animal tissue result in different yields and alterations to the material at the fibrillar and macromolecular level. Fibrillar extraction methods mechanically separate tissue into fibril dispersions, removing non-collagenous components with the aid of selective proteolysis and washes [26]. Native assembly and crosslinking is not extensively disrupted as the insoluble fibrils are

processed into suspensions. Other methods exist to isolate and purify collagen into solutions of monomeric collagen or small macromolecular aggregates. From some tissues, soluble collagen can be extracted at very low yield with dilute salt solutions. Higher yields are achieved with dilute acid solutions, which disrupt native aldimine crosslinks [26]. Following acid extraction, collagen may be separated from other tissue components by centrifugation and filtration. Sequential filtration stopping at the 0.45 μm level yields aggregates of an average of 2.85 molecules, while filtration to the 0.22 μm level yields monomeric collagen [27]. Solutions completely free of aggregates are difficult to obtain, and aggregates are usually present in the absence of 0.22 μm filtration. Alkali and enzymatic protocols more aggressively disrupt native crosslinks, cleave most of the non-helical ends of the collagen monomer, termed the telopeptides, and result in higher yields [26]. After removal of the telopeptide regions, the material is referred to as atelocollagen. Solutions of both acid-solublized and atelocollagen can be triggered to reassemble into fibrillar structures.

In addition to the isolation of animal collagens, homologous, autologous, and recombinant human collagens are either in use or development. Homologous and autologous collagens are used clinically as for tissue augmentation, although the supply of both is inevitably limited [28]. Recombinant human collagens have been generated, and may be coexpressed with the enzyme prolyl 4-hydroxylase. This enzyme converts proline to 4-hydroxyproline, after which recombinant collagens have been shown to adopt triple helical structure and self-assemble into fibrils [29].

Collagen has been extensively studied as a biomaterial and successfully employed clinically. A small percentage of patients will mount an immune response against bovine

or porcine collagen implants, although the risk of adverse reaction can be minimized by screening for collagen allergy in advance [30]. Collagen is prepared for implant either by techniques that retain the fibrous architecture of the ECM or by protocols that purify collagen into a solution or dispersion and then process it into a physical form, such as an injectable, fiber, gel, sheet, membrane, or coating. Processes that retain the native ECM architecture include steps that destroy and remove the remnants of living cells, and crosslink and sterilize the remaining ECM. Many non-collagen components remain after processing. Example devices include bioprosthetic heart valves and small instestinal submucosa, a sheet used to repair and reinforce soft tissue. Preparation of an implant from collagen solutions or dispersions generally consists of precipitation, sterilization, and crosslinking. During precipitation, collagen monomers and aggregates can be triggered to self-assemble to approximate the fibrillar assembly in the ECM; alternatively solutions can be air dried, freeze dried, or otherwise deposited without fibrillar structure [31]. Capacity to recreate the complex and spatially varying density and orientations of native fibril networks is limited. Significantly, fibrillar structure determines the mechanical response of many tissues and in some cases may regulate cell proliferation, migration, and matrix synthesis [32].

Elastin-mimetic protein triblock copolymers. Several elastin-mimetic protein polymers based on variations of the [VPGVG] pentapeptide repeat sequence of native elastin have been designed and evaluated. Results have been positive with regards to biostability in the absence of chemical crosslinks [2], nanofiber formation and tunable mechanical properties [3], drug-release and micelle formation [4, 5], and non-thrombogenic coatings [6].

The properties of an elastin-mimetic protein polymer may be tailored by modifying of the (VPGVG) consensus repeat sequence, combining different repeat sequences, and/or introducing other bioactive peptide sequences. Adjustment of the repeat sequence alters the solubility and mechanical character. For example, the elastin pentapeptide displays temperature dependent solubility in water; it is extended and solvated at low temperatures but collapses and aggregates when warmed above the transition temperature (T_t). The value of T_t depends on the polarity of the sequence, and is usually adjusted by altering the identity of the fourth residue in the pentapeptide [1]. Increasing polarity of the fourth residue strengthens polymer solvent interactions, predictably increasing T_t. The mechanical character of the sequence has been adjusted from elastic to plastic by changing the third residue from glycine to alanine.

Application of the block copolymer design framework has generated additional control over the properties of elastin-mimetics. Hydrophilic and hydrophobic protein polymer blocks were created from variations of the consensus pentapeptide repeat and combined as diblocks and triblocks. The 209 kDa triblock used in this project, **LysB10**, has a midblock 28 with repeats of the elastic, hydrophilic $(VPGAG)_2VPGEG(VPGAG)_2$ sequence of pentapeptides. Both endblocks contain 170 repeats of the plastic, hydrophobic (IPAVG) sequence. The triblock has the capacity to form reversible virtual crosslinks and chemical crosslinks [2]. Dissolving the protein polymer in cool (4°C) water and warming it introduces virtual crosslinks as the hydrophobic endblocks self-associate as they approach room temperature. The midblock remains elastic and soluble at room and body temperatures. Consequently, self-association transforms concentrated solutions of the material into elastomeric gels. Chemical crosslinks may be introduced by

modification of lysine residues that are available between the mid- and endblocks of **LysB10** [2]. The addition of chemical crosslinks is expected to enhance biostability and has been shown to enhance strength and resistance to creep.

CHAPTER 2

LARGE SCALE PRODUCTION OF CONTINUOUSLY SPUN SYNTHETIC COLLAGEN FIBER

INTRODUCTION

Collagen fiber serves well-known structural roles in many tissues, and has been a candidate for tissue repair and replacement for decades. The earliest version of manufactured collagen fiber, catgut suture, consisted of sheep or bovine intestine, chemically and mechanically processed into strands that were ground and polished to create suture [33]. The processing introduced non-uniformities and potential mechanical failure points. Catgut also generated variable tissue reactivity and often a highly inflammatory response [34]. Following catgut, reconstituted collagen fiber processes were developed to improve thread uniformity and reduce non-collagen tissue remnants to decrease the inflammatory response. In these protocols, tendon was processed into gels or dispersions consisting of collagen fibrils and extruded it into acetone-based solutions to generate fiber [35, 36]. However, animal studies indicated inferior performance of chromic reconstituted collagen compared to chromic catgut, seemingly due to suture fragmentation and chemical irritation [37].

Subsequent to reconstituted fibers, others processed collagen into more highly pure fiber explicitly for medical fabrics and tissue engineering. Collagen was formulated into dispersions or solutions and extruded into aqueous buffers instead of acetone. After an incubation period, fibers were dehydrated in alcohol and air-dried [38]. Before fiber

fabrication, these protocols purified the collagen into ultrafiltered solutions of aggregates of a few molecules or monomeric collagen, instead of the collagen fibril dispersions of earlier processes [39, 40]. These and similar methods also employed longer buffer incubations, totaling 30 min [41] to 48 hr [42]. Longer incubation provided ample time for collagen molecules or aggregates to reassemble into fibrils. These incubations usually limited the length the self-assembled collagen fiber to short 10-20 cm segments instead of continuous fiber. For example, if fiber was continuously extruded at 1 m/min, and 30 minutes of incubation were required, then 30 meters of the nascent protein filament had to be threaded through a series of incubation baths without breaks or tangles. To avoid this difficulty, long incubations were truncated in continuous fiber spinning systems [43-45]. However, in one such case, inferior properties were reported when comparing continuous fiber to short fiber segments made with longer incubations [43]. In another instance, electron micrographs showed that banded collagen fibrils had only self-assembled on the outer shell of continuously spun fiber [44].

In this study, we report a process in which the requirements for continuous fiber spinning were decoupled from the long incubations required for fibril self-assembly. The continuous spinning system included an extrusion tube and 2 m rinsing bath. After the fiber was dried, collected, and stored on rollers it was subjected to a separate off-line incubation step. The decoupled system resulted in scalable production of continuous fiber, with evidence of fibril formation throughout the fiber cross-section.

MATERIALS and METHODS

Isolation and purification of monomeric collagen. Acid-soluble, monomeric rat-tail tendon collagen (MRTC) was obtained from Sprague-Dawley rat tails following

Silver and Trelstad [46]. Frozen rat tails (Pel-Freez Biologicals, Rogers, AK) were thawed at room temperature and tendon was extracted with a wire stripper, immersed in 10 mM HCl (pH 2.0; 150 mL per tail) and stirred for 4 hr at room temperature. Soluble collagen was separated by centrifugation at 30,000 *g* and 4°C for 30 minutes followed by sequential filtration through P8, 0.45 µm, and 0.2 µm membranes. Addition of concentrated NaCl in 10 mM HCl to a net salt concentration of 0.7 M, followed by 1 hr stirring and 1 hr centrifugation at 30,000 *g* and 4°C, precipitated the collagen. After overnight re-dissolution in 10 mM HCl the material was dialyzed against 20 mM phosphate buffer for at least 8 hr at room temperature. Subsequent dialysis was performed against 20 mM phosphate buffer at 4°C for at least 8 hr and against 10 mM HCl at 4°C overnight. The resulting MRTC solution was stored at 4°C for the short-term or frozen and lyophilized.

Production of a synthetic collagen microfiber by continuous co-extrusion. A modified wet spinning device facilitated collagen fiber production (Figure 2.1). A collagen solution (2, 5, or 7.5 mg/ml in 10 mM HCl) and wet spinning buffer (WSB: 10 wt% poly (ethylene glycol) Mw = 35000, 4.14 mg/mL monobasic sodium phosphate, 12.1 mg/mL dibasic sodium phosphate, 6.86 mg/mL TES (N-tris (hydroxymethyl) methyl-2-aminoethane sulfonic acid sodium salt), 7.89 mg/mL sodium chloride, pH = 8.0) were extruded with a dual syringe pump (Harvard Apparatus, Holliston, MA). The collagen solution emerged through a 0.1 or 0.4 mm inner diameter blunt-tipped needle into the center of a vertical tube (1.6 mm inner-diameter x 1 m long fluoropolymer tubing) at rates 0.03, 0.06, or 0.1 mL/min. Wet spinning buffer simultaneously advanced through a bubble trap and down the fluoropolymer tube at a rate of 1.0 mL/min. As it

exited the extrusion needle, the collagen coagulated into a gel-like fiber and was carried downward by the WSB stream.

Upon emergence from the fluoropolymer tube, the fiber entered a 2 meter-long rinsing bath of 70% ethanol in water. Initially, 5 to 10 meter samples of manually collected fiber (MC) were collected by hand on rectangular frames. After optimization, automatically collected fiber (AC) was produced and collected by winding it out of the rinsing bath onto segments of polyvinyl chloride (PVC) pipe that rotated and translated automatically.

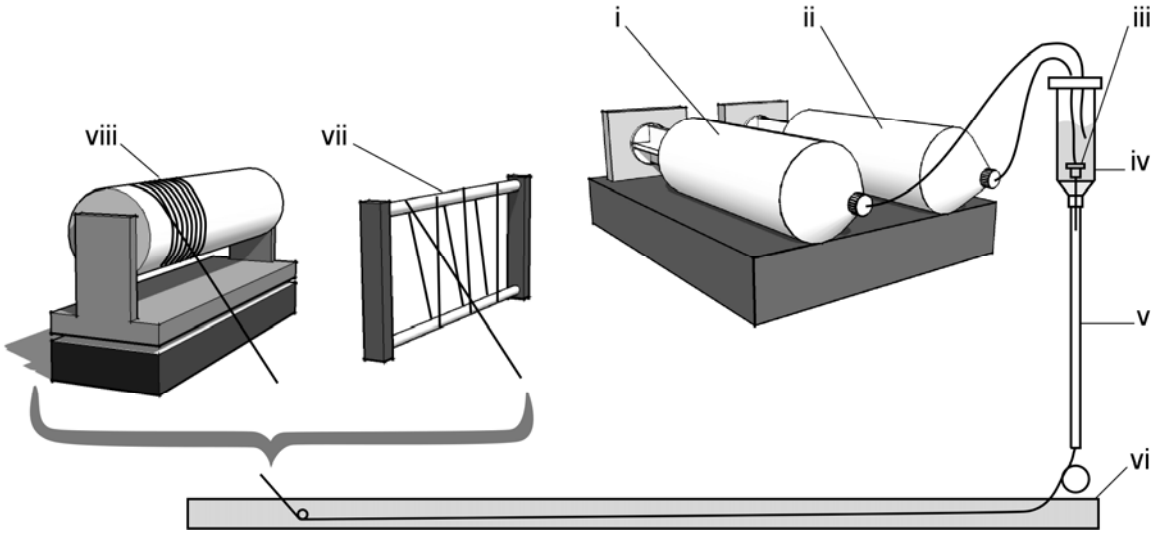

Figure 2.1. Wet spinning system. A syringe pump extruded WSB (i) though a bubble trap (iv) and into a coagulation column (v). The pump also drove the flow of the collagen solution (ii) through a needle (iii) and into the column. As the collagen stream emerged from the needle, it aggregated into a gel-like fiber due to the surrounding WSB. Flowing WSB carried the collagen fiber down the column, into the 70% ethanol rinse (vi). Short fiber segments were collected from the rinse with a hand-operated frame (vii). An automated roller system (viii) was installed to collect 30 to 60 m of continuous fiber.

Fiber incubation and drying. After spinning, the fiber was placed in fiber incubation buffer (FIB: 7.89 mg/mL sodium chloride, 4.26 mg/mL dibasic sodium

phosphate, 10 mM Tris, pH = 7.4) [47] at 37°C for 48 hr. Manually collected fiber was incubated on rectangular frames, while automatically collected fiber was incubated directly on PVC pipe segments. Rectangular frames containing MC were subsequently rinsed for 15 min in ddH20 and 2 min in 70% ethanol before drying in air. Pipe segments containing AC fiber were rinsed in ddH20 for 15 min before drying and collecting the fiber under tension with an automated system (Figure 2.2).

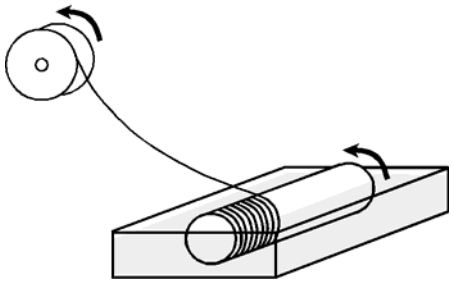

Figure 2.2. System for continuous fiber collection and drying. After FIB incubation, pipe segments were rinsed in ddH20 for 15 minutes and transferred to the collection and drying system. The pipe segment was partly immersed in 70% ethanol and the AC fiber was transferred through air to a second pipe segment. The fiber dried under tension as it traveled between the two pipe segments.

Fiber crosslinking. Some fibers were left in a desiccator on a ceramic plate above a pool of 25% (w/v) glutaradehyde in water for 18 - 24 hr. To remove excess glutaraldehyde, fibers were subjected three 4 hr rinses, gently rocking in PBS. Fibers were stored in PBS for immediate testing or rinsed in water and air dried.

Optimization of wet spinning parameters. Spinning parameters, including the concentration of the collagen solution, collagen solution flow rate, and extrusion needle size were varied and the diameter and strength of the resulting MC fiber was measured. Nine combinations of wet spinning parameters were investigated before the conditions

for AC fiber production were selected (Table 2.1). For each set of parameters that consistently produced fiber, samples were crosslinked with glutaraldehyde vapor and rinsed before diameter measurement and mechanical testing. Initial experiments showed that decreasing collagen flow rate and concentration lowered fiber diameter, resulting in more frequent fiber failure during processing. Conditions were selected for automatically collected fiber production to minimize fiber diameter while eliminating breaks during fiber spinning.

Mechanical annealing of collagen fibers. Some samples of fiber were subject to a mechanical annealing protocol similar to that previously reported by Pins et al. [48]. Specifically, fiber was collected manually from the spinning system on expandable rectangular frames and transferred to 37°C FIB solution for 24 hr. Adjustment to the expandable frames imparted 0, 15, or 30% strain to the fibers followed by 24 additional hours in buffer. These samples, referred to as MC-0%, MC-15%, and MC-30%, were rinsed and dried identically to non-annealed MC fiber and analyzed with transmission electron microscopy (TEM).

Analysis of fiber diameter and cross-sectional area. Optical microscopy permitted measurement of the crosslinked, hydrated fiber diameter. Preliminary examination revealed that the fiber cross-section was somewhat flattened and resembled an ellipse. Each fiber segment was twisted to display the widest and narrowest cross-section dimensions beneath a 20x objective and three measurements of each were recorded per sample. After analyzing six to ten samples from each type of fiber, the cross-sectional area was approximated using:

$$A_{cross\text{-}section} = \pi \, (D_{major} \cdot D_{minor}) / 4$$

where D_{major} and D_{minor} represent the diameters of the major and minor axes of the fiber cross-section.

Table 2.1. Wet Spinning Parameters†

MC Sample Number / AC	Needle Inner Diameter (mm)	Collagen Extrusion Rate (mL/min)	Collagen Concentration (mg/mL)
1	0.4	0.1	5
2	0.4	0.06	5
3	0.4	0.03	5
4	0.4	0.015	5
5	0.4	0.1	2
6	0.4	0.06	2
7	0.4	0.06	7.5
8	0.1	0.06	7.5
9	0.1	0.03	7.5
AC	0.4	0.08	5

† MC sample numbers 4 – 6 were not analyzed further because the low collagen extrusion rate or concentration resulted in frequent breaks during fiber spinning.

Mechanical responses of single collagen fibers. A Dynamic Mechanical Thermal Analyzer V (DMTA V, Rheometric Scientific, Piscataway, NJ) enabled tensile strength analysis of crosslinked, hydrated fiber samples. Fiber was prepared by gluing either end of a segment of dry fiber between thin plastic shims with cyanoacrylate glue. Samples were hydrated in PBS overnight and loaded in the DMTA by clamping the plastic shims in the instrument grips. The DMTA was inverted with the sample submerged in a thermally jacketed beaker of 37°C PBS. Samples were loaded with a gauge length of 6 to 9 mm, pulled to 5% strain and relaxed in four preconditioning cycles, and pulled to failure at a rate of 5 mm/min. The force and strain at failure were

recorded and engineering ultimate tensile stress (UTS) was calculated using the cross-sectional area estimate for each fiber type.

Microdifferential scanning calorimetry (μDSC). Automatically collected fiber before or after the FIB treatment (AC-FIB and AC+FIB), after FIB treatment and glutaraldehyde crosslinking (AC+FIB+GLUT), and rat tail tendon (RTT) were pressed into 5 –8 mg pellets, dried under vacuum, massed, and hydrated for 10 hrs in 0.5 mL of PBS at 5°C. Similarly, MRTC was lyophilized, massed, and hydrated. Analysis in a μDSC III (Setaram Instrumentation, Caluire, France) permitted the investigation of triple-helix unfolding as samples were heated from 5 to 90°C at 0.5°C/min and returned to 5°C. Heat flow per unit mass was plotted against furnace temperature. The denaturation temperature, T_m, was determined from the peak of the denaturation transition, while the area of the transition was used to calculate the enthalpy of denaturation, ΔH. Lack of a similar thermal transition in a second identical heating cycle confirmed complete denaturation in the initial heating cycle.

Analysis of Second Harmonic Generation (SHG). The SHG system consisted of an Olympus IX71 inverted microscope coupled to a Ti-Sapphire laser (Spectra Physics, Mountain View, CA). A 60 x 1.2 NA (0.28 mm) water immersion objective focused and collected the backward signal, while a 1.4 NA oil immersion condenser (Olympus, Center Valley, PA) collected the forward signal. High sensitivity photomultiplier tube devices (Hamamatsu Photonics, Hamamatsu City, Japan) detected both the forward and backward signals. In preparation, AC fiber was hydrated in PBS for 2 hrs and mounted beneath a cover slip with PVA-Dabco mounting media. Ten-micron cryosections of RTT were also mounted with PVA-Dabco. Spectrometer analysis of the

emitted signal confirmed the presence of a steep intensity peak at 480 nm, half the excitation wavelength of 960 nm, indicative of SHG. The forward-to-backward (F/B) signal ratios were calculated for both rat tail tendon and continuous fiber.

Transmission electron microscopy. As previously described [47], bundles of approximately ten parallel, uncrosslinked fibers were tied at both ends with 4-0 prolene suture, hydrated for 1 hr in PBS, rinsed three times in 0.1 M cacodylate buffer (pH = 7.4), fixed (2.5% glutaraldehyde in 0.1 M cacodylate buffer, pH 7.4) for 90 minutes, and washed in 0.1 M cacodylate water followed by ddH_20. Samples were partly dehydrated in 30% ethanol followed by staining en bloc with filtered 2% uranyl acetate in 50% ethanol. Preparation continued with ethanol series dehydration, 100% resin infiltration, and polymerization for 3 days at 60°C. Using an RMC MT-7000 ultramicrotome (Boeckeler, Tucson, AZ) and a diamond knife, ultrathin sections (60-80 nm) were cut to reveal cross and axial perspectives of the fiber interior. Following a post-stain with 3% uranyl acetate and Reynold's lead citrate, sections were examined and photographed with a JOEL JEM-1210 TEM (JOEL, Tokyo, Japan) at 90 kV. Samples investigated included MC-0%, MC-15%, MC-30%, and AC. The diameter of collagen fibrils in continuous fiber was estimated from 40 measurements taken from four 50,000x magnification images of the fiber cross-section, and the result was expressed as the mean and standard deviation.

Murine subcutaneous implant studies. The host response and biostability of glutaraldehyde crosslinked and uncrosslinked continuous fiber was assessed by subcutaneous implant in 10 wk old, 25-30 g, inbred male C57BL/6 mice (Jackson Laboratory, Bar Harbor, ME), as approved by the Emory University Institutional Animal

Care and Use Committee (IACUC). To prepare the implants, bundles of 160 fibers, 2 cm in length, were aligned and tied at both ends with 7-0 prolene suture. Crosslinked bundles were exposed to glutaraldehyde vapor for 18 hr, followed by a 24 hr rinse in sterile water and a 1 hr incubation in PBS immediately before the implant. Uncrosslinked bundles were incubated in PBS for 1 hr immediately prior to implant. Three bundles of crosslinked and uncrosslinked fiber were implanted for a 6 wk period.

Following sedation with ketamine (95 mg/kg, IM) and xylazine (5 mg/kg, IM), a subcutaneous pouch was created through a dorsal midline incision and the fiber bundle implanted. After 3 or 6 wks, animals were sacrificed, fiber bundles excised with overlying skin, and samples photographed to qualitatively assess gross local tissue responses. All samples were fixed overnight in 10% neutral buffered formalin and processed for parafin embedding. Five-micron sections were stained with hematoxylin and eosin (HE) to visualize tissue morphology and Gomori's Trichrome to distinguish collagen. Immunohistochemical staining was performed with rat monoclonal antibody [CI:A3-1] which recognizes the F4/80 antigen expressed by murine macrophages (Abcam, Inc., Cambridge, MA).

Statistics. Tests for statistically significant differences between the means of two groups were conducted with the Student's *t*-test (two-tailed, homoscedastic). Tests between three or more groups were conducted with the one-way ANOVA followed by the Tukey HSD test.

RESULTS

Development of a scalable system for continuous collagen fiber formation. For AC fiber production, PVC pipe segments (outer diameter = 48 mm) were typically rotated at 6 rpm and translated at 6 mm/minute, leading to the deposition of consecutive loops of 15.2 cm of fiber along the 20 cm length of the pipe segment. Each pipe segment

was therefore loaded with about 30 m of fiber in 33 min. Although production rate was not maximized, this supply proved adequate for characterization and production of experimental collagen fiber assemblies.

Collagen fibers can be produced without loss of triple helical structure. The μDSC study (Table 2.2, Figure 2.3) demonstrated that wet spinning without FIB treatment did not change ΔH, and increased T_m by 8.4°C on average. Treatment with FIB increased ΔH to the level of RTT and slightly increased T_m. Samples of RTT display a substantially higher T_m.

Table 2.2. Apparent Temperature and Enthalpy of Collagen Denaturation[†]

	MRTC	AC-FIB	AC+FIB	AC+FIB+GLUT	RTT
T_m (°C)	36.2 ± 0.6	44.8 ± 0.2	46.9 ± 1.7	78.6 ± 4.0	58.9 ± 0.4
ΔH (J/g)	49.4 ± 0.8	48.9 ± 2.1	57.4 ± 0.9	26.0 ± 3.6	56.3 ± 0.8

[†]Purified collagen (MRTC), continuous fiber without FIB treatment (AC-FIB), continuous fiber with FIB treatment (AC+FIB), continuous fiber with FIB treatment and glutaraldehyde crosslinking (AC+FIB+GLUT), and rat-tail tendon (RTT). Both the process of spinning collagen into fiber and the FIB treatment increased the thermal stability of the material, as shown by the elevated T_m and ΔH values. Values are averages and standard deviations from three scans.

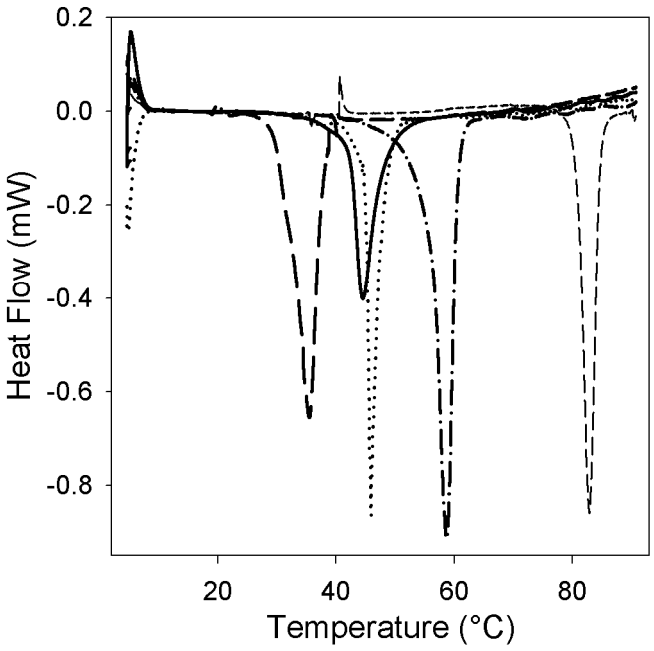

Figure 2.3. Micro-differential scanning calorimetry of MRTC (long dash), AC-FIB (solid), AC+FIB (dotted), RTT (dash-dot), and AC+FIB+GLUT (short dash). Representative results from three experiments are shown.

Collagen fiber size is influenced by selection of wet spinning parameters. The average major fiber cross-section dimension increased significantly ($p < 0.05$) with increasing needle size, collagen flow rate, and collagen concentration (Figure 2.4). Average UTS of manually collected samples was between 54 and 90 MPa. Differences in UTS were not significant at the $p < 0.05$ level for the samples compared in Figure 2.4. Automatically collected fiber displayed the highest mean UTS (Figure 2.5, Table 2.3).

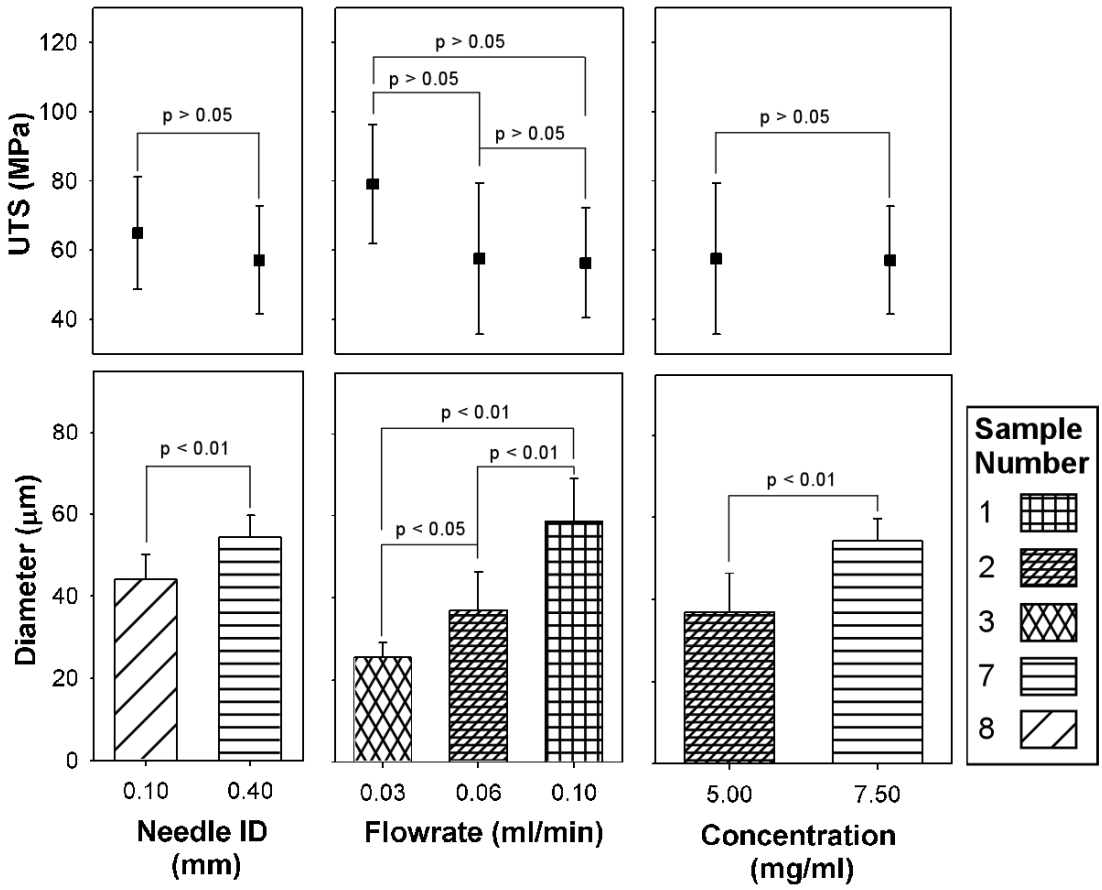

Figure 2.4. Selected comparisons of UTS and major diameter of crosslinked MC with varied wet spinning parameters. All differences in mean diameter resulting from altered spinning parameters were statistically significant ($p<0.05$), while all differences in UTS were not. Error bars represent standard deviations.

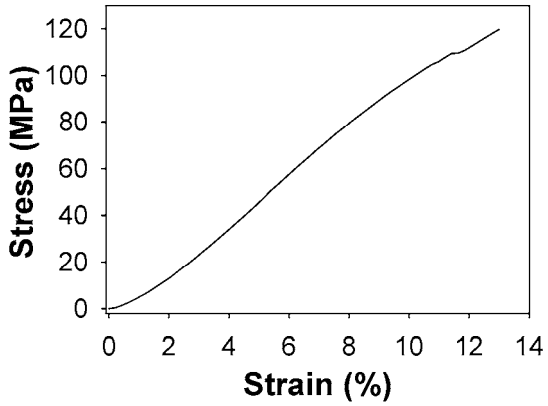

Figure 2.5. Representative stress-strain data for automatically collected fiber.

Table 2.3. Size and Mechanical Properties of Collagen Fiber

MC Sample Number / AC [†]	Needle ID (mm)	Extrusion Rate (mL/min)	Concentration (mg/mL)	Major Diameter (mμ)	Minor Diameter (mμ)	UTS (MPa)	Modulus (MPa)	Strain-to-failure (%)
1	0.4	0.1	5	59 ± 10	22 ± 3	54 ± 12	556 ± 120	11.2 ± 2.9
2	0.4	0.06	5	37 ± 9	17 ± 2	60 ± 16	529 ± 157	12.4 ± 3.1
3	0.4	0.03	5	25 ± 4	12 ± 2	77 ± 16	673 ± 100	12.6 ± 1.8
7	0.4	0.06	7.5	55 ± 6	27 ± 2	55 ± 14	575 ± 66	11.2 ± 2.5
8	0.1	0.06	7.5	44 ± 6	25 ± 2	67 ± 19	608 ± 54	12.2 ± 3.2
9	0.1	0.03	7.5	29 ± 3	20 ± 2	90 ± 37	837 ± 133	11.7 ± 3.5
AC	0.4	0.08	5	53 ± 14	21 ± 3	94 ± 19	775± 173	14.3 ± 1.9

[†]Samples 4 through 6 did not consistently produce fiber.

Collagen fibers can be produced as a close packed assembly of axially oriented D-peridodic fibrils. The axial sections of FIB-treated MC samples revealed banded fibrils while the sections from untreated samples did not (Figure 2.6). With no axial stretching (MC-0%), the fibrils were disorganized, although isolated areas of alignment with the fiber axis could be identified. Fibers mechanically annealed to 15 or 30% displayed qualitatively more alignment (Figure 2.7). The automatically collected fiber sections displayed an aligned, densely packed fibril structure even without mechanical annealing (Figure 2.8). Fibril diameter average and standard deviation were 54 ± 13 nm. Fiber samples also displayed an SHG signal (Figure 2.9). The F/B ratio was 0.039 for continuous fiber and 3.75 for rat-tail tendon.

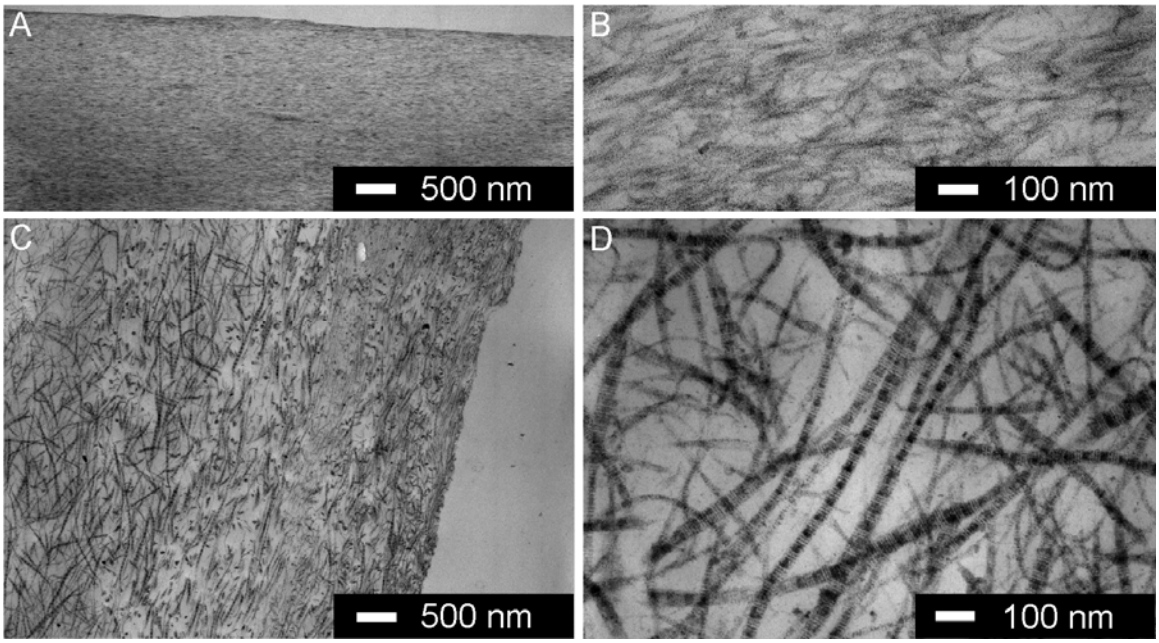

Figure 2.6. Incubation in FIB results in the assembly of collagen fibrils. Banded collagen fibrils were not visible in axial sections of the untreated fiber (A, B), but were broadly evident following incubation (C, D).

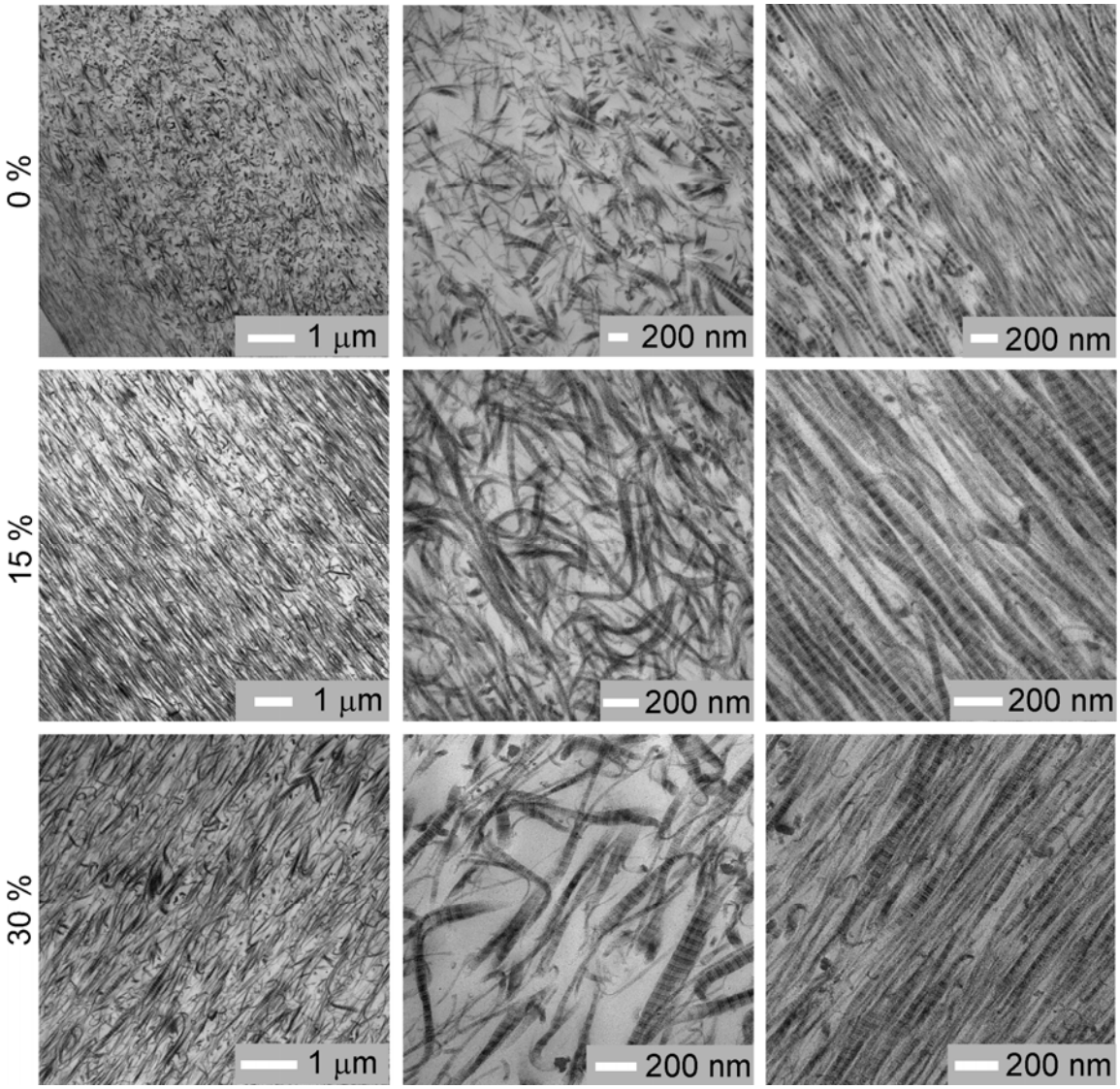

Figure 2.7. Mechanical annealing during incubation enhances fibril alignment. Lower magnification axial sections of MC-0%, MC-15%, and MC-30% (left column) showed a trend toward enhanced fibril alignment in the stretched samples (middle and bottom rows). However, alignment was not uniform: in high magnification images of the samples, regions of low fibril alignment (center column) and high alignment (right column) could be identified.

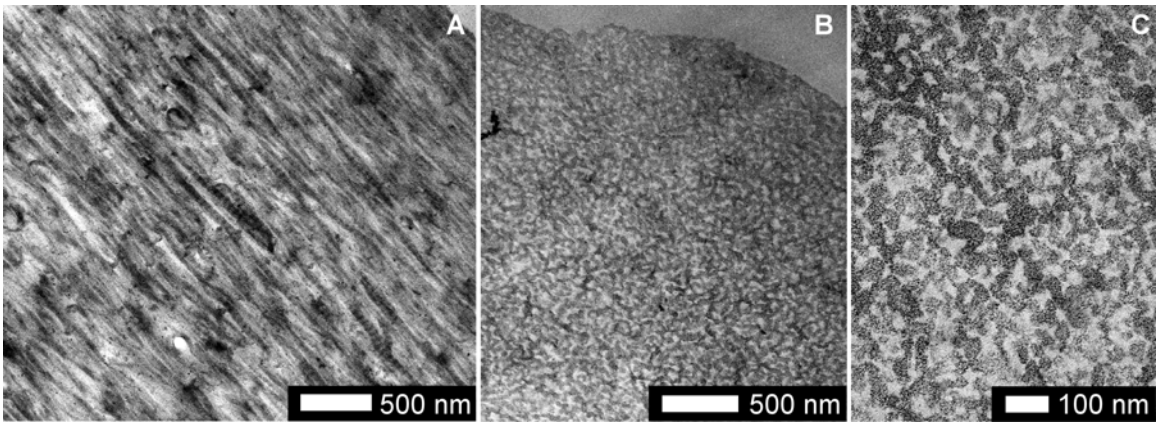

Figure 2.8. Fibrillar structure of AC imaged by TEM. Axial sections revealed an aligned pattern of fibrils, often displaying banding (A). Fiber cross sections consisted of tightly packed fibril cross sections (B, C).

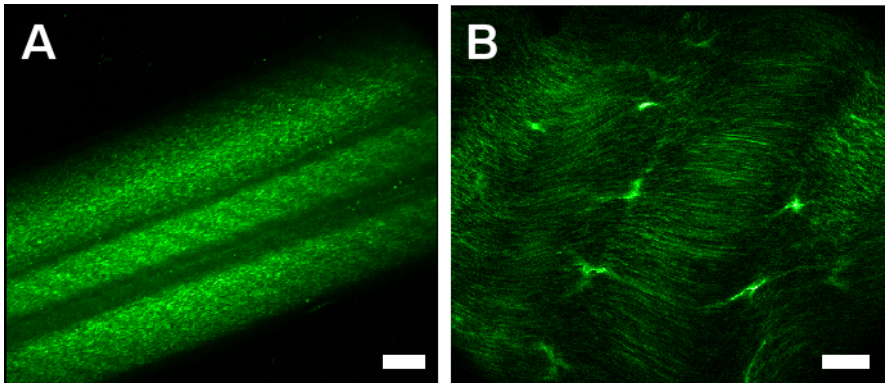

Figure 2.9. The second harmonic generated by FIB treated manually collected fiber and rat-tail tendon. A cluster of three wet spun fibers displayed a clear SHG signal but only short discontinuous fibrillar substructure was noted (A). The signal from rat-tail tendon revealed fibrillar structure (B). Scale bars are 20 μm.

Murine subcutaneous implant studies. After six weeks, all samples could be readily located and explanted. Uncrosslinked fiber bundles were firmly adhered to the skin, while crosslinked bundles were not adhered. Photographs before and after the implanting indicated that the length of the crosslinked bundles was unchanged, while the uncrosslinked bundles shrunk to approximately 30% of the original length during the implant period. Fiber diameter and bundle size were similar for both crosslinked and uncrosslinked samples (Figure 2.10). Gomori's Trichrome stained crosslinked and uncrosslinked fibers red and blue, respectively. More fibrous collagen was deposited around the perimeter of the uncrosslinked bundles, while the crosslinked bundles contained more fibrous material in the bundle interior, surrounding individual fibers. Fibers near the perimeter of the uncrosslinked bundles were smaller than those in the bundle center. Immunohistochemistry demonstrated that macrophages were also located predominantly at the perimeter of uncrosslinked bundles, and within the crosslinked bundles (Figure 2.11).

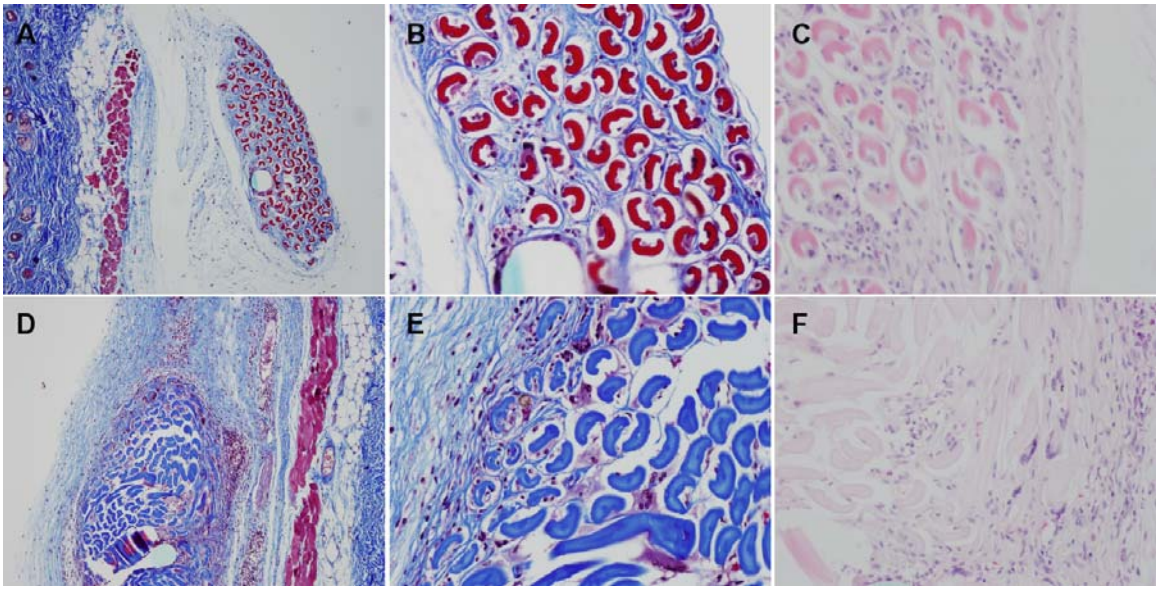

Figure 2.10. Morphology of explanted fiber bundles after 6 weeks. Upper three panels show crosslinked bundles while the lower panels are uncrosslinked bundles. Sections are stained with Gomori Trichrome (A, B, D, E) or HE (E, F). Original magnifications were 10X (A, D) or 40X (B, C, E, F).

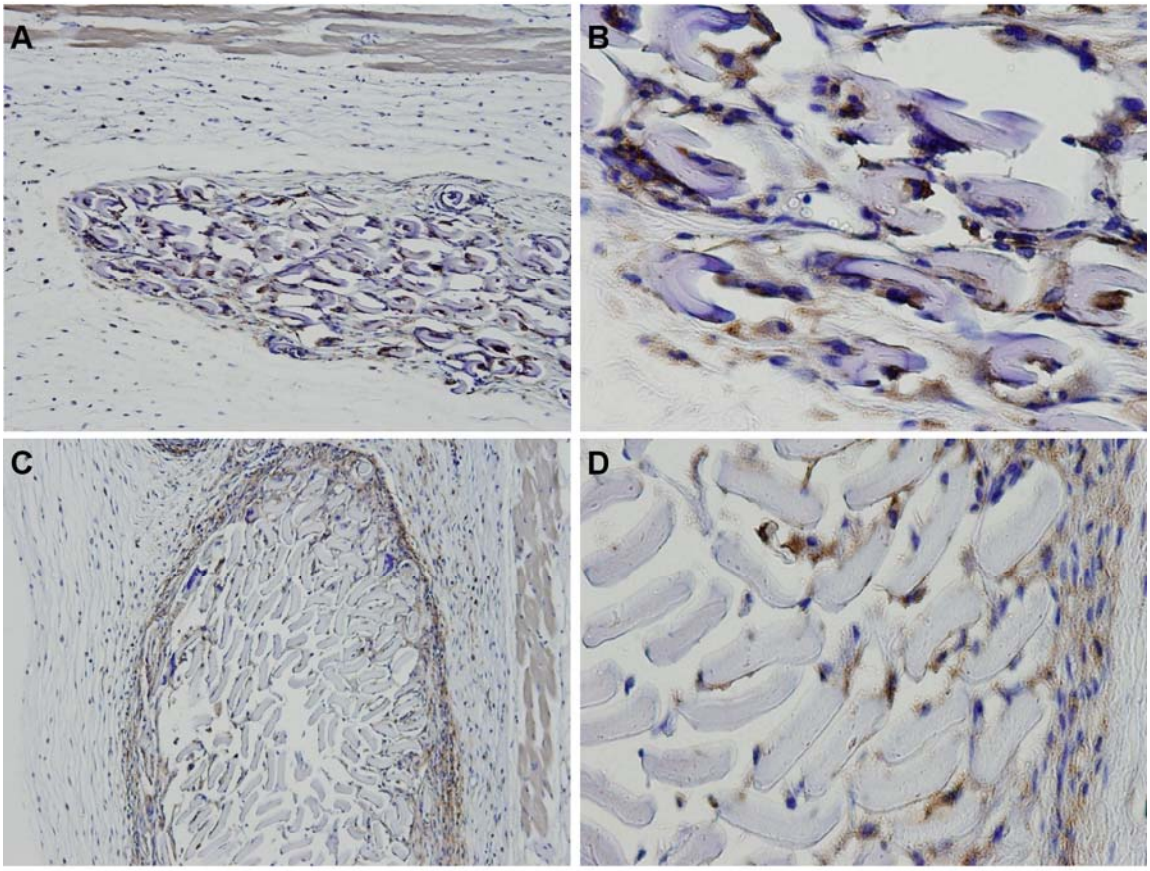

Figure 2.11. Macrophage distribution in crosslinked and uncrosslinked fiber bundles. Macrophages were present inside the crosslinked bundles of fiber (A, 10x, and B, 40x) but collected primarily around the perimeter of the uncrosslinked bundles (C, 10x, and D, 40x)

DISCUSSION

This report describes large scale production of collagen fiber with fibrillar substructure that closely mimics that of native collagen fibers. In the first stage of spinning, a purified, acid-soluble, MRTC solution and a buffered PEG solution were continuously co-extruded through fluoropolymer tubing to form a fiber that was passed into a rinsing trough, through air, and onto a collection roller. Although the first spinning

stage failed to reformulate the banded, fibrillar structure of native collagen, TEM demonstrated that an additional 48 hr incubation drove fibrillar self-assembly throughout the fiber cross-section. Without specialized equipment, the system spun 60 m/hr of fiber, which compares favorably to fiber production rates of 100 m/hr, previously reported for experimental collagen textile production systems that did not display fibrillogensis throughout the fiber cross-section [44].

Techniques for producing collagen fiber may be categorized either as processes that yield continuous fiber or short discontinuous fiber segments suitable for laboratory analysis. Excluding catgut production and older methods of spinning fibril dispersions, several scalable, continuous fiber-spinning methods have recently been proposed [43-45]. Silver and Kato compared discontinuous and continuous methods and observed that fiber produced by a continuous process displayed somewhat inferior mechanical properties and faster biodegradation [43]. Both their continuous and discontinuous processes consisted of extrusion into a fiber formation buffer at 37ºC, a rinse in isopropyl alcohol, a rinse in water, and air drying. However, during the continuous process the temperature of the fiber formation buffer was noted to fall below 37ºC, and all of incubations and rinses were shorter than in the discontinuous process. Also, less tension was applied to the fiber during the air drying step of the continuous process. These factors, in particular, shorter incubation time in the fiber formation buffer, may not permit optimal collagen self-assembly and fibril formation, contributing to sub-optimal mechanical properties and biostability [43]. Pins and coworkers have also reported a discontinuous fiber process using longer incubation periods, and were able to generate fibrils throughout the fiber cross-section [40, 42]. In another discontinuous fiber system, Zeugolis and colleagues

recently demonstrated fibril formation after three relatively short incubations of 10-15 min [41, 49-51]. Adaptation of this protocol to continuous spinning may be feasible but would be more complex in nature with a lower overall production rate, given the requirement for a total incubation time of up to 45 min. This group studied fibril formation in fibers extruded from both pepsin and acid extracted collagen. Pepsin treated collagen can be harvested in higher yield and contains fewer antigenic determinants due to cleavage of most of the telopeptide regions and, thus, may offer certain advantages as compared to acid extracted collagen. Unfortunately, fibril banding and density was significantly reduced in discontinuous fibers produced from pepsin extracted collagen [41].

Others have developed a microfliudic system to characterize fibril formation by real-time x-ray microdiffraction and birefringence during collagen fiber spinning [52]. Data generated from this technology may eventually enable the selection of temperatures, flowrates, and buffer systems for scalable production of fiber with aligned, banded fibrils without any additional incubation required. However, at present no process for spinning purified collagen solutions into continuous fibers with adequate fibrillar structure is available. By appending an off-line incubation step to a relatively simple continuous spinning process, we have created a process that is both scalable and results in fibrillogenesis throughout the fiber.

Thermal and optical analysis demonstrates conservation of collagen triple helical structure. Triple helical structure defines the collagen family of proteins, is a prerequisite for fibril self-assembly, and, critically, shields antigenic and proteolytic cleavage sites [30]. Use of unsuitable solvents and high temperatures, for example in

early collagen wet spinning processes and electrospinning [53], destabilizes the triple helix and may be expected to compromise biocompatibility, biostability, and strength of the resulting material. In this study, μDSC demonstrated that spinning monomeric collagen into fiber, before fibrillogenesis, did not disrupt triple helical structure, and raised the apparent helix T_m by 8.4°C. This increase may largely be attributed to the enhanced stability of the collagen aggregated in the fiber compared to the monomeric collagen in solution. However, the different hydrating solutions used during the calorimetry measurement also caused a portion of the T_m difference. The fiber was hydrated with PBS (pH 7.4), while the monomeric collagen was dissolved in 10 mM HCl (pH 2.0). The stability of the triple helix is related to pH, and increasing pH from 2 to 7.4 which would account for more than a 2°C increase in T_m [54, 55]. Comparing results for fibers before and after fibrillogenesis demonstrates that fibril formation moderately raised T_m and elevated ΔH by 15%. The greater thermal stability observed after fibrillogenesis is likely due to hydrophobic interactions in the fibril and greater surface energy associated with the melting of a larger fibrillar structure [55]. The T_m of AC+FIB was 12°C less than that noted for native tendon, since the tendon is further stabilized by native covalent crosslinks.

SHG emission is consistent with retention of triple helical structure and fibril assembly. Second harmonic generation occurs when laser light passes through a molecularly noncentrosymmetric, highly polarizable material. The wavelength is halved and the frequency is doubled in a coherent optical process [56]. SHG in extruded fiber and other reformulated collagens confirms the retention of triple helix structure with loss of triple helical structure eliminating the SHG signal [53]. Although the collagen triple

helix is necessary to produce an SHG signal, this feature alone, in the absence of fibrillar assembly is insufficient for signal generation. For example, triple-helical, non-fibrillar collagen (type IV) does not produce SHG [57, 58]. Furthermore, reports have proposed that only a portion of the collagen in a fibril, possibly in the fibril's outer shell, can generate SHG scattering [59, 60]. High SHG forward to backward signal ratios have been correlated with increased collagen fibril thickness. This has been attributed to the accumulation of the forward signal as light travels through the fibril with limited accumulation of the backward signal due to destructive interference [59]. Therefore, the low F/B ratio observed in continuous fiber may be due to lower fibril diameters compared to RTT. The reconstituted fibril diameters in this study were 54 ± 13 nm, while the fibrils from RTT are reported to have a bimodal diameter distribution with average diameters of 70 and 250 nm [61].

Wet spinning parameters can be adjusted to optimize continuous fiber diameter and strength. Optical microscopy revealed that continuous fibers were produced with an elliptical cross-section with a ratio of major to minor axis diameters of approximately 2:1. Reduction of collagen extrusion rate or the collagen concentration reduced the diameter of the fiber, presumably because in both cases less collagen was supplied to produce a given length of fiber. Reducing the diameter of needle used for extrusion of the collagen solution by a factor of four led to only slight reduction of fiber diameter, probably because the decrease in needle size did not change the flow rate of the collagen solution. The smallest fibers produced were 12 by 25 μm in cross-section, however, parameters ultimately selected for automatically collected fiber yielded larger

fibers to eliminate breaks during wet spinning. Dimensions of fiber produced by other strategies are summarized in Table 2.4.

The ultimate tensile strength of the automatically collected fiber is compared collagen fiber in other reports in Table 2.4. Automatically collected fibers were on average stronger than manually collected fibers of a similar diameter in this study. Qualitatively, TEM showed enhanced fibril alignment and density in AC, possibly generated by greater tension applied during the spinning, drying and collection of AC. After drying and collection, the length of the dried fiber is approximately 5% more than the length of the incubated, hydrated fiber. However, the total strain induced in the drying step includes both the 5% observed strain and the reduction in fiber length that would occur if the fiber were dried without tension, at least 5 to 10%. Therefore, the drying and collecting step imparts 10 to 15% strain to the fiber. Indeed, mechanical drawing and related techniques have been shown to increase strength in other collagen fiber systems [40, 62]. In addition to mechanical force, others have employed magnetic and electric fields [63, 64], magnetic beads [65], thermal convection currents [66], blow drying [67], microfluidics [52, 68], and cell-based collagen synthesis and assembly [69-73] to align collagen. The goals of these studies are related either to enhanced mechanics or contact guidance in cell culture and tissue engineering systems.

Table 2.4. Summary of Collagen Fiber Diameter and Strength In Prior Reports and in the Current Study†

Ref.	Fiber Scheme	Diameter (μm)	UTS (MPa)	Crosslinking Scheme
[38]	DF	-	66.2 ± 17.20 (Wet)	Glut Vapor
[43]	CF	70.3 ± 8.6 (Wet) 56.8 ± 7.4 (Dry)	36.9 ± 7.90 (Wet)	Glut Vapor
[74]	DF	20 – 40 (Dry)	42.9 ± 9.55 (Wet)	Glut Vapor
[39]	DF	-	91.8 ± 31.4 (Wet)	DHT
[42]	DF	55.5 ± 5.17 (Dry) 88.72 ± 8.57 (Wet)	56.62 ± 11.17 (Wet)	DHT
[75]	DF	59 (Wet)	50.0 ± 13.4 (Wet)	EDC
[41]	DF	52 ± 8 (Dry)	255 ± 89 (Dry)	None
[51]	DF	153 ± 7 (Dry) 270 ± 8 (Wet)	182 ± 18 (Dry) 5.86 ± 1.01 (Wet)	None
[50]	DF	119 ± 15 (Dry)	208 ± 57 (Dry)	None
[49]	DF	306 ± 29 (Wet)	10.85 ± 2.85 (Wet)	Glut Solution
[44]	CF	25 (Dry)	27.7 ± 23.1 (Wet)	Glut Vapor
Current Study	CF	53 ± 14 by 21 ± 3 (Wet)	93.9 ± 19.2 (Wet)	Glut Vapor

†The strength of hydrated, glutaraldehyde crosslinked fibers is provided when available. XL refers to crosslinking method and Glut, DHT, and EDC refer to glutaraldehyde, dehydrothermal, and 1-Ethyl-3-[3-dimethylaminopropyl]carbodiimide hydrochloride crosslinking. Fiber schemes are indicated as discontinuous fiber (DF) and continuous fiber (CF) processes.

Local tissue responses to collagen fibers. Crosslinked fiber implants displayed short-term biostability and a local inflammatory response consistent with previous reports [74, 76]. While others have quantified biodegradation as a reduction in the number of intact fibers [77], we also observed an overall shortening of the uncrosslinked fiber bundles by approximately 70%, while the length of crosslinked bundles did not appreciably change. However, the uncrosslinked bundles could still be identified and explanted. In contrast, others have found that even after dehydrothermal-cyanamide crosslinking, many fibers were completely degraded after 10 days and all fibers were degraded after 6 wk in a rat intramuscular implant [74]. Similarly, Kato and Silver reported that crosslinked fiber bundles were degraded 2 weeks after implantation in the subcutaneous tissue of a rat animal model [43]. The greater stability we observed may be partly due to our use of a mouse model rather than any property of AC fiber. Khouw et al. compared the response of mice and rats to subcutaneous collagen implants and found more giant cells and substantially increased evidence of implant phagocytosis in rats when compared to mice [78].

CONCLUSIONS

Although collagen fiber has been manufactured for decades, techniques that are easily scalable for textile production, begin with a purified solutions rather than fibril dispersions, and yield fibrillar assembly throughout the fiber have been slow to materialize. Here we report a process for continuous spinning followed by off-line incubation. This system did not disrupt the triple helical macromolecular structure, and

triggered fibrillogenesis. Bundles of crosslinked fiber generated a typical healing response in a mouse implant. Uncrosslinked fiber exhibited relatively biostablility.

CHAPTER 3
ANISOTROPIC PROTEIN POLYMER LAMELLAR ELASIC STRUCTURES

INTRODUCTION

In this report, we describe a new, scalable, semi-automated, fabrication process that yields elastin-like protein sheets reinforced with synthetic collagen fibers that can be positioned in a precisely defined three-dimensional hierarchical pattern. To our knowledge, this is the first description of an artificial collagen fiber reinforced composite within an elastin-like matrix protein that displays many of the biomechanical properties of native tissues. Significantly, the flexible nature of the fabrication process lends itself to varying fiber orientation and volume fraction within and between individual lamellae of a planar sheet. Moreover, it is evident that such structures can be used as acellular tissue analogues or incorporated within schemes that integrate cells within the analogue prior to or after implantation in vivo.

The composition and hierarchical structure of collagen and elastin protein fiber networks dictates the mechanical responses of all soft tissues and related organ systems. In turn, the biomechanical properties of a tissue dictate a variety of performance characteristics that affect function and durability, including local cellular behavior. As a prototypical soft tissue, the composite nature of the vascular wall was first highlighted in 1957 when Roach and Burton demonstrated that as pressure is increased within an iliac artery, the vessel initially behaves as a highly compliant tube, which displays a rapid

increase in material stiffness as the physiologic range of normal blood pressure is exceeded. The highly compliant responses at relatively low pressures could be attributed to elastin, while the collagen fiber network was identified as the primary feature that dictated increasing tissue stiffness at high pressure [79]. This unique arrangement of collage and elastin networks afforded a tissue of substantial strength that is both compliant and resilient. Significantly, in the case of arterial blood vessels, these properties contribute to the dampening of peak pulsatile blood pressure, reduction of the mechanical work of the heart, and enhanced resistance of blood vessels to fatigue and catastrophic failure in response to repetitive cyclic loading forces [80].

The vessel wall provides a useful starting point for the consideration of the integrated structure and significance of collagen and elastin networks. However, nearly all other soft tissues are dependent upon the presence of such networks, whose uniquely site-specific composition and structure profoundly influences organ specific function. For example, as heart valve leaflets close during ventricular diastole and are subject to increasing strain, the mechanical response transitions from compliant to stiff due to the mechanics and geometry of a coordinated network of collagen and elastin fibers. Broom described the process of collagen fiber straightening and aligning with applied stress and the role of elastin in returning the collagen to its relaxed formation, as a complementary deformation processes [81]. This relationship is thought to facilitate efficient stretching of leaflets as the valve closes, providing large coaptation regions that limits retrograde bloodflow, as well as rapid leaflet opening in response to forward flow [82].

The biological and biomechanical significance of the extracellular matrix (ECM) has motivated the development of analogues as candidate scaffolds to replace diseased or

damaged tissues, including blood vessels, heart valves, skin, as well as fascia and tendon. Two design decisions, sourcing of materials and the fabrication method, are inherent to each approach. In practice, investigators have most often addressed the challenge of generating a matrix substitute through the use of decellularized xenogeneic tissues, which have been used clinically in various forms for nearly 50 years. Although clinically effective devices have been processed from xeneogeic tissues, including bovine mesenteric vein and bioprosthetic porcine heart valves, the flexibility in designing a tissue to meet a desired set of conditions is limited by a fixed set of starting tissue properties, as well as matrix composition and architecture. Natural tissue variability and potential contaminants also pose challenges.

Alternative approaches, that remain largely preclinical in nature, include the use of living cells to assemble extracellular matrices, as well as other fabrication methods, such as molding, lyophilizing, and electrospinning to process purified native proteins. Cell-based extracellular matrix assembly strategies include molding of cells in degradable polymers [83] and biopolymers [84] and blood vessel substitutes fabricated from rolled sheets of cells and their endogenous matrix [85]. Living tissue substitutes offer numerous advantages, but acknowledged limitations include long production times, cell sourcing, and the inability to create devices that display prolonged shelf life. Moreover, although collagen fiber networks produced by cells can be generated with some degree of alignment, the capacity to assemble fiber composites containing a substantial elastin network has not achieved nor has it been possible to create 3-D structures with precisely defined architecture that provides the flexibility to tailor related biomechanical responses [85-87]. The development of a convenient process for the large-scale production of

continuous synthetic collagen fibers composed of D-periodic fibrils facilitated the investigation if such an approach.

Our laboratory has synthesized several elastin-mimetic protein polymers based on variations of the [VPGVG] peptide repeat sequence of native elastin. In particular, recombinant triblock copolymers containing an elastomeric, hydrophilic midblock flanked by rigid hydrophobic, plastic-like, endblocks have emerged as a promising biomaterial platform with the capacity to undergo either reversible, physical crosslinking or chemical crosslinking. These materials exhibit excellent biostability in vivo, even in the absence of chemical crosslinks [2], can be processed as nanofibers with tunable mechanical properties [3], micelles [4, 5], or used for drug-release applications. Primate shunt studies have confirmed that these elastin protein polymers can form non-thrombogenic blood contacting coatings [6]. In this report, we employ an elastin-mimetic protein polymer with an integrated, oriented system of synthetic collagen fibers to fabricate APPLES (Anisotropic Protein Polymer Laminated Elastic Structures).

MATERIALS and METHODS

Synthesis of a recombinant elastin-mimetic triblock protein polymer. Genetic engineering, expression, purification, and characterization of the elastin-mimetic protein polymer, designated **LysB10,** has been described elsewhere [2]. Briefly, the flanking 75 kDa endblocks of the protein polymer contained 33 repeats of the hydrophobic pentapeptide sequence $[IPAVG]_5$, and the central 58 kDa midblock consisted of 28 repeats of the elastic, hydrophilic sequence $[(VPGAG)_2VPGEG(VPGAG)_2]$. The

sequences between blocks and at the C terminus include the residues, [KAAK], provides amine groups for chemical crosslinking.

The protein polymer sequence was contained a single contiguous reading frame within the plasmid pET24-a, which was used to transform the *E. coli* expression strain BL21(DE3). Fermentation was performed at 37°C in Circle Grow (QBIOgene) medium supplemented with kanamycin (50 μg/mL) in a 100 L fermentor at the Bioexpression and Fermentation Facility, University of Georgia. Cultures were incubated under antibiotic selection for 24 hr at 37°C. Isolation of the **LysB10** consisted of breaking the cells with freeze / thaw cycles and sonication, a high speed centrifugation (20,000 RCF, 40 min, 4°C) with 0.5% poly(ethyleneimine) to precipitate nucleic acids, and a series of alternating warm / cold centrifugations. Each cold centrifugation (20,000 RCF, 40 min, 4°C) was followed by the addition of NaCl to 2M to precipitate the protein polymer as it incubated for 25 min at 25°C. This was followed by warm centrifugation (9500 RCF, 15 min, 25) and resuspension of the pellet in cold, sterile PBS on ice for 10 – 20 min. After 6 to 10 cycles, when minimal contamination was recovered in the final cold centrifugation, the material was subject to a warm centrifugation, resuspended in cold sterile PBS, dialyzed, and lyophilized.

Isolation and purification of monomeric collagen. Acid-soluble, monomeric rat-tail tendon collagen (MRTC) was obtained from Sprague-Dawley rat tails following Silver and Trelstad [46]. Frozen rat tails (Pel-Freez Biologicals, Rogers, AK) were thawed at room temperature and tendon was extracted with a wire stripper, immersed in 10 mM HCl (pH 2.0; 150 mL per tail) and stirred for 4 hr at room temperature. Soluble collagen was separated by centrifugation at 30,000 *g* and 4°C for 30 minutes followed by

sequential filtration through P8, 0.45 µm, and 0.2 µm membranes. Addition of concentrated NaCl in 10 mM HCl to a net salt concentration of 0.7 M, followed by 1 hr stirring and 1 hr centrifugation at 30,000 *g* and 4°C, precipitated the collagen. After overnight re-dissolution in 10 mM HCl the material was dialyzed against 20 mM phosphate buffer for at least 8 hr at room temperature. Subsequent dialysis was performed against 20 mM phosphate buffer at 4°C for at least 8 hr and against 10 mM HCl at 4°C overnight. The resulting MRTC solution was stored at 4°C for the short-term or frozen and lyophilized.

Production of a synthetic collagen microfiber by continuous co-extrusion. A modified wet spinning device facilitated collagen fiber production. A collagen solution (5 mg/mL in 10 mM HCl) and wet spinning buffer (WSB: 10 wt% poly (ethylene glycol) Mw = 35000, 4.14 mg/mL monobasic sodium phosphate, 12.1 mg/mL dibasic sodium phosphate, 6.86 mg/mL TES (N-tris (hydroxymethyl) methyl-2-aminoethane sulfonic acid sodium salt), 7.89 mg/mL sodium chloride, pH 8.0) were extruded with a dual syringe pump (Harvard Apparatus, Holliston, MA). The collagen solution emerged through a 0.4 mm inner diameter blunt-tipped needle into the center of a vertical tube (1.6 mm inner-diameter x 1 m long fluoropolymer tubing) at 0.08 mL/min. Wet spinning buffer simultaneously advanced through a bubble trap and down the fluoropolymer tube at a rate of 1.0 mL/min. As it exited the extrusion needle, the collagen coagulated into a gel-like fiber and was carried downward by the WSB stream. Upon emergence from the fluoropolymer tube, the fiber entered a 2 meter-long rinsing bath of 70% ethanol in water. Continuous fiber was produced and collected by winding it out of the rinsing bath onto segments of polyvinyl chloride (PVC) pipe that rotated and translated automatically.

After spinning, the fiber was placed in fiber incubation buffer (FIB: 7.89 mg/mL sodium chloride, 4.26 mg/mL dibasic sodium phosphate, 10 mM Tris, pH = 7.4) [47] at 37°C for 48 hr. Fiber was incubated directly on the PVC pipe segments used for collection. Subsequently, pipe segments containing continuous fiber were rinsed in ddH20 for 15 min before drying and collecting the fiber under tension with an automated system.

Fabrication of anisotropic protein polymer lamellar elastic structures from synthetic collagen fibers within an elastin-like protein polymer matrix. Several APPLES were designed and fabricated by winding defined collagen fiber layouts onto rectangular frames and implementing the transition temperature fiber embedding and lamination protocol illustrated in Figure 3.1. To arrange the fiber with the desired spacing and angle, the frame translation speed, translation distance, and rotation speed were computed with a MATLAB script. An automated linear actuator (Velmex, Inc, Bloomfied, NY) and a DC gear motor translated and rotated the frames. After winding, each fiber layout was transferred onto a sheet of ultrasoft polyurethane, secured with tape, and photographed. Images from at least three regions of each layout enabled the measurement of average fiber spacing and angle.

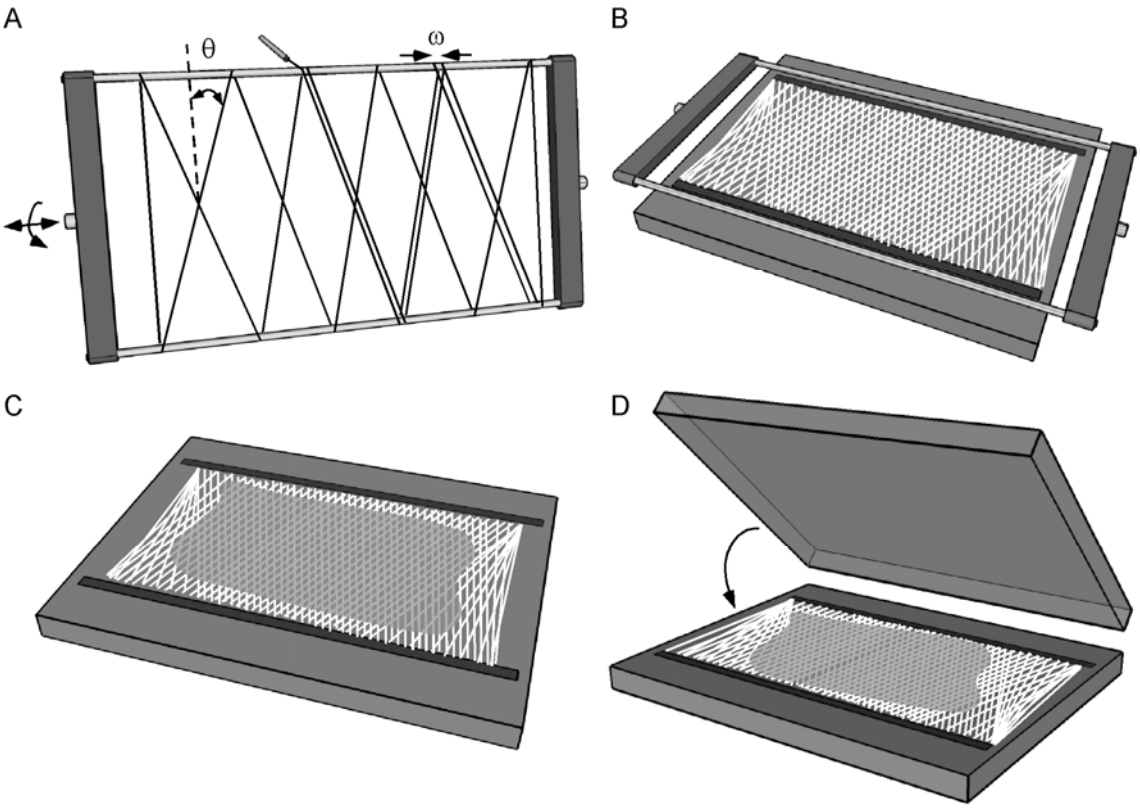

Figure 3.1. The process for embedding a fiber layout in a elastin-like protein matrix. Fiber was wound about rectangular frames to obtain the desired fiber orientation angle, θ, and average spacing, ω (A). The fiber layouts were transferred to sheets of ultrasoft polyurethane (B), and the **LysB10** solution was distributed over the layout (C). An acrylic sheet was placed over the layout to spread the **LysB10** solution into a film reinforced with the fiber layout (D).

Solutions of **LysB10** were prepared at 10 wt% concentration in ice-cold ddH_2O. Argon was bubbled through the solutions, followed by centrifugation at 4°C and 500g for 5 min to remove bubbles. To embed the fiber layouts, precision 50 μm thick plastic shims (Precision Brand, Inc., Downers Grove IL) were placed around the layouts, and all embedding materials were cooled to 4°C. The **LysB10** solution was distributed over the fibers and a sheet of acrylic was pressed on top of the solution. The fibers and the

LysB10 solution were located within a 50 μm space, sandwiched between the acrylic sheet and polyurethane base that were separated by precision shims. The embedding assembly was left at 4°C for one hour to allow the **LysB10** solution to hydrate the fiber layout, followed by transfer of the assembly to 37°C incubator for 30 min. When the polyurethane and acrylic sheets were peeled apart, the fiber layout remained embedded in a solid film of **LysB10**, adherent to the polyurethane base. After a 5-minute incubation in 37°C ddH_2O, the fiber-reinforced film could be separated from the polyurethane base.

Each APPLES design consisted of a stack of ten 40 μm thick layers. The eight central layers contained embedded fiber while the top and bottom layers contained only **LysB10**. Ten-layer stacks were covered with plastic wrap to prevent drying, cooled to 4°C for 12 hr, and transferred to 37°C for 30 min to facilitate interlamellar bonding with formation of a cohesive sheet. The sheet was removed, rinsed in 37°C PBS for 30 min, and crosslinked in 0.5% glutaraldehyde in PBS for 24 hr at 37°C. Vigorous shaking in PBS for 6 hr at 37°C with three buffer changes served to remove excess glutaraldehyde.

Analysis of collagen fiber orientation and volume fraction. Six different fiber layouts were analyzed. To study fiber spacing, we prepared samples with fiber orientations of 15° and spacing equal to 0.15 mm, 0.45 mm, or 1.3 mm, as well as a sample without fiber. Fiber volume fraction was calculated from measurements of average fiber spacing taken from digital photographs of the fiber layouts, the fiber diameter of 40 μm, and the thickness of the multilamellar sheet (400 μm). The fiber spacings above corresponded to 17, 7, 3, and 0% fiber volume fractions. The effect of fiber orientation was demonstrated by setting fiber volume to 17% and adjusting fiber orientation to 0°, 15°, or 90°. The primary orientations of the fiber layouts were

measured from digital photographs of the fiber layouts using the Inverse Fast-Fourier Transform tool from ImageJ software [88].

Digital volumetric imaging of fiber orientation and packing density. For digital volumetric imaging (DVI), fiber was first conjugated to tetramethyl rhodamine isothiocyanate (TRITC) [89]. Fiber was wound about a PVC pipe segment placed inside a larger pipe. This arrangement created a 100 mL annular volume in which 20 – 40 m of fiber could be reacted without tangles or breaks. A 1 mg/mL solution of TRITC in DMSO was added to a 0.1 M sodium carbonate solution to a concentration of 0.05 mg/mL. This solution was added between the pipe segments and stirred for 12 hr at 4°C, after which the fiber was rinsed four times with ddH2O for 2 hr and for 5 min with 70% ethanol, and then dried as it was transferred to a second pipe segment (Figure 3.2). Composite sheets re-enforced with TRITC-conjugated fiber were prepared for DVI by serial dehydration in ethanol and xylene. Samples were embedded in Spurr's epoxy modified with an optical opacifier, Sudan Black B, and imaged with a DVI Microimager (Microscience Group, Inc. Redwood City, CD).

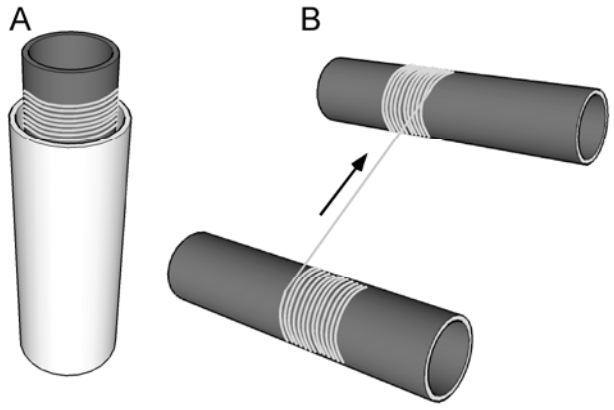

Figure 3.2. Fiber was reacted in a co-axial pipe system (A) and dried by transferring it through air to a second roller (B).

Transmission electron microscopy. Transmission electron microscopy was used to investigate the ultrastructure of the composite. Samples of the APPLES were rinsed twice in 0.1 M cacodylate buffer (pH 7.4), fixed (2.5% glutaraldehyde in 0.1 M cacodylate buffer, pH 7.4) for 90 minutes, washed in 0.1 M cacodylate water and then dH_20, postfixed with 1% osmium tetroxide for one hour, and stained en bloc with filtered 2% uranyl acetate in 50% ethanol. Samples were then dehydrated with an ethanol series, pre-infiltrated with propylene oxide, and embedded in Spurr's epoxy. Using an RMC MT-7000 ultramicrotome and a diamond knife, ultrathin sections (60-80 nm) were cut to display planes perpendicular to the x, y, and z directions (Figure 3.2). For the TEM analysis, these planes were referred to as the x, y, and z sections. Sections were post-stained with 3% uranyl acetate and 2% lead citrate, and examined and photographed using a JOEL JEM-1210 TEM at 90 kV.

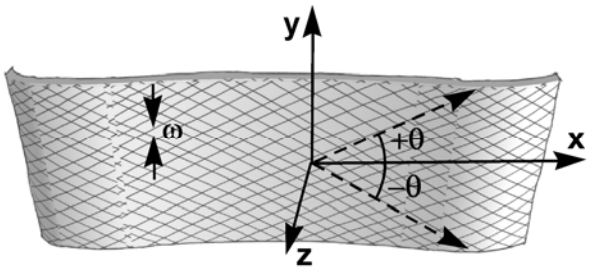

Figure 3.3. Fiber composite sheet geometry. Fibers made an angle of ± θ with the x direction of the sheet. The y direction was through the width of the sheet, and the z direction was through the sheet thickness. Fiber spacing, ω, was measured in the y direction.

Scanning electron microscopy. Samples for scanning electron microscopy were cut with a razor blade to expose x and y sections of the sheet. The z face, or the top of the sheet, was also imaged. Samples were critical point dried (E3000, Energy Beam Sciences, Inc., East Granby, CT), sputter coated with gold (Emscope SC-500, Emitech, Kent, England), and examined and photographed with a DS-150 F scanning electron microscope (Topcon Co., Tokyo, Japan) operated at 15 kV.

Mechanical responses of anisotropic protein polymer lamellar structures. The effects of fiber orientation and volume fraction on APPLES mechanical properties were evaluated under uniaxial tension. Conditioning and tensile analysis were conducted on a dynamic mechanical thermal analyzer DMTA V (Rheometric Scientific, Inc., Newcastle, DE) with a 15 N load cell in the inverted orientation, so that samples could be immersed in a jacketed beaker of 37 °C PBS. For each fiber layout, 5 to 7 replicates of the APPLES were tested. Samples that were 4 mm in width and 0.4 mm in thickness were mounted on the mechanical testing equipment with gauge lengths of 12 to 13 mm. Force was applied in the x direction indicated in Figure 3.2. Samples were extended to 8% strain for 16 cycles and then to 30% strain. Samples that did not fail when stretched to 30% were remounted on a miniature materials tester, the Minimat 2000 (Rheometric Scientific Inc., Newcastle, DE), and tested to failure. All tests were performed at a rate of 5 mm/min. For each APPLES design, resilience was calculated from the 8% strain data by dividing the area beneath the loading curve by the area beneath the unloading curve and multiplying by 100%, and reported as the mean and standard deviation from all samples. To characterize fiber failure modes, samples were treated after testing with Van Gieson's stain to distinguish the collagen fiber and photographed.

Suture retention strength of protein fiber composite sheets. Sutures (Prolene 4-0) were passed through 4 mm square APPLES segments at a distance of 2 mm from the sheet edge. Samples had a fiber orientation of 15° and volume faction of 17%. The APPLES was clamped in the DMTA, and the suture was fastened to the actuating arm of the instrument and pulled at a rate of 1 mm/sec. The maximum force measured before the suture tore out of the sheet was recorded as the suture retention strength, reported in grams-force (g-f). For seven samples, the suture was pulled in the y direction, and for four samples the suture was pulled in the x direction.

Statistics. Tests for statistically significant differences between the means of two groups were conducted with the Student's *t*-test (two-tailed, homoscedastic). Tests between three or more groups were conducted with the one-way ANOVA followed by the Tukey HSD test.

RESULTS and DISCUSSION

Rigid fiber-reinforced composites are widely known to offer a combination of high stiffness, strength, and toughness at low weight. Flexible composites display an alternative property set. This class of materials has long been applied as steel or Kevlar-reinforced rubber composites common in pneumatic tires, and is under investigation for applications such as morphing aircraft wings, flexible body armor, and stretchable electronics [90-92]. Advanced passive mechanical properties associated with flexible composites includes an enormous usable deformation range, the propensity to store and return strain energy, to limit crack propagation and fatigue, to tailor mechanical anisotropy and Young's Modulus [93], and to engineer nonlinear mechanical responses [94]. The APPLES presented here provide a protein-based biomaterial platform that incorporates the mechanical characteristics of flexible composites.

Structural analysis of a protein polymer composite. Multilamellar sheets were initially translucent and colorless, but acquired a slightly tan color after glutaraldehyde crosslinking. Fiber angle and spacing were measured from photographs of the fiber layouts and fiber volume fraction calculated by assuming an average fiber diameter of 40 μm, a sheet thickness of 400 μm, and the presence of eight fiber-reinforced layers in the composite sheet (Table 3.1). Observed fiber orientation and spacing based on image analysis of 2-D photographic images were close to expected values and consistent with the three-dimensional geometry of the fiber layout reconstructed from digital volumetric imaging (Figures 3.4 and 3.5). Transmission electron microscopy revealed that fibers were comprised of axially aligned, D-periodic fibrils resembling native collagen (Figure 3.6). High resolution SEM images demonstrated that composite sheets were uniformly bonded without evidence of voids or delamination between individual 40 μm membrane layers within each sheet (Figure 3.7).

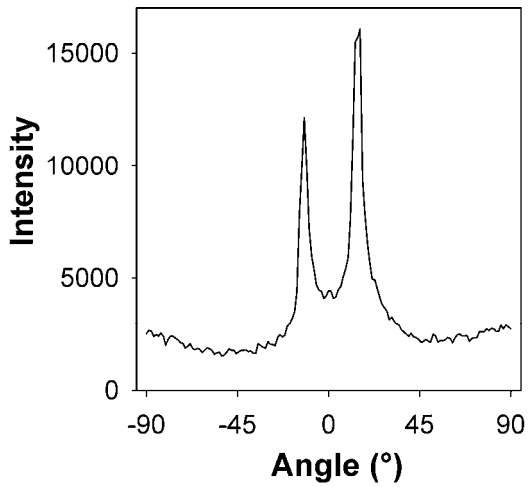

Figure 3.4. Representative plot from fiber orientation analysis of a layout with a fiber orientation of 15° and volume fraction of 7%. Intensity peaks at –12.0 and 15.6° correspond to the nominal fiber orientations of ±15°.

Table 3.1. Assessment of Fiber Layout

Design Number	Fiber Orientation (°)		Fiber Spacing (mm)		Volume fraction (%)
	Nominal	Measured	Nominal	Measured	
1	0	0.8 ± 3.7	0.15	0.19 ± 0.01	16.3 ± 0.6
2	90	90.8 ± 1.4	0.15	0.19 ± 0.01	16.7 ± 0.5
3	15	13.4 ± 0.9	0.15	0.18 ± 0.01	17.7 ± 0.8
4	15	13.2 ± 0.8	0.45	0.47 ± 0.02	6.8 ± 0.3
5	15	13.0 ± 0.9	1.30	1.03 ± 0.03	3.1 ± 0.1

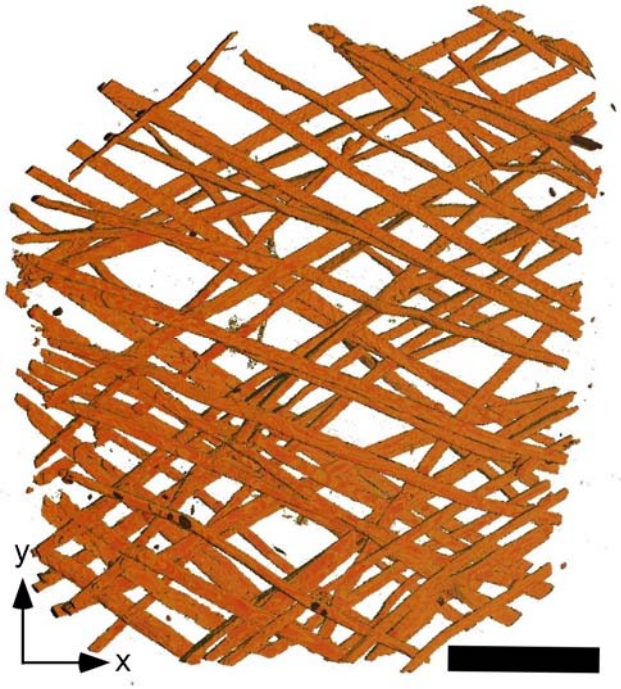

Figure 3.5. Fiber layout reconstructed by digital volumetric imaging. The x and y directions are as indicated. Scale bar is 500 μm.

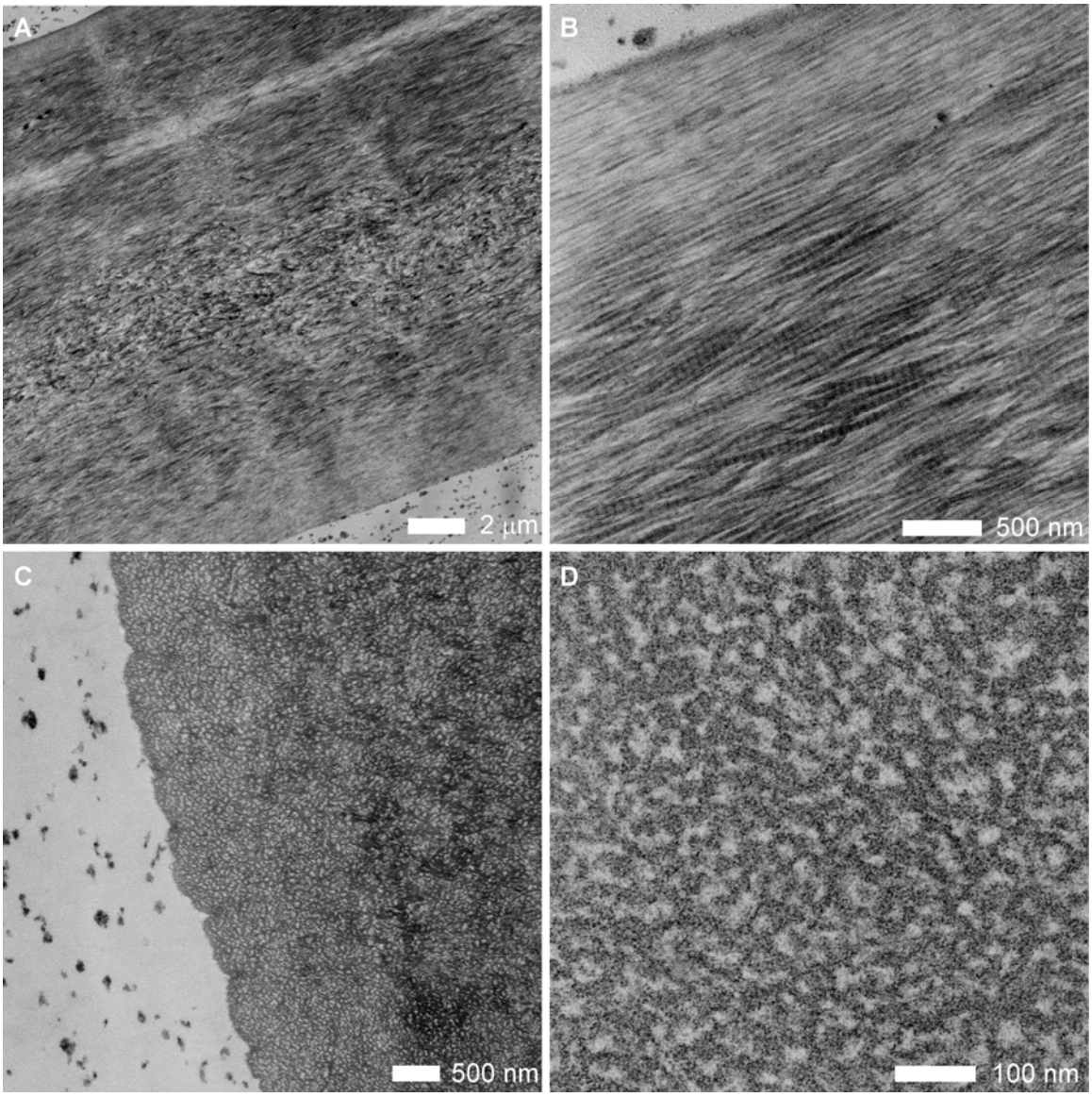

Figure 3.6. Transmission electron microscopy of a multilamellar sheet. Stain localized in irregularly shaped 50 – 200 nm areas that speckled the **LysB10** matrix. Z sections of the composite displayed wet spun collagen fibers with a banded fibrillar structure, generally aligned with the overall fiber axis (A, B). In the x section views of the sheet, the collagen fiber consisted of densely packed fibrils in cross section (C, D).

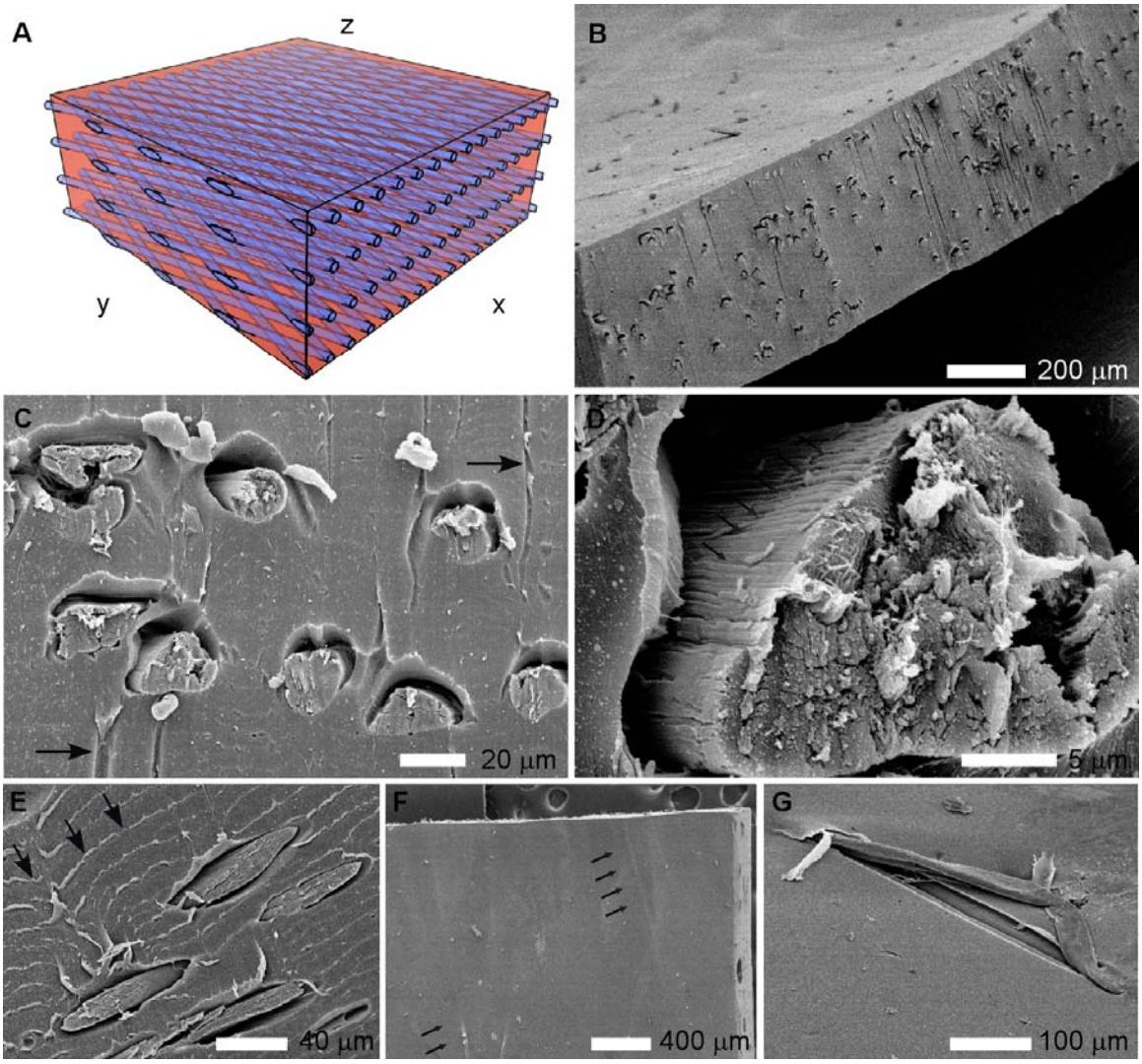

Figure 3.7. Scanning electron microscopy of a multilamellar sheet. As illustrated, the fiber cross-section will appear circular or elliptical when the sheet is sectioned along the x- or y-plane, respectively (A). Synthetic collagen fibers can be visualized within a cross-section through the x-plane of the composite sheet (B, C). The exterior of the fibers display a fibrillated texture (arrows, D). Fibers protruding within a cross-section through the y-plane appear elliptical due to the oblique angle they made with the section plane. Sectioning artifacts appeared in (C) as vertical microgrooves and in (E) as feathered horizontal ridges in the protein polymer. The number and spacing of the ridges indicated that they did not correspond directly to the lamellar interfaces. Some fibers appear beneath the z-plane of the sample, and in rare instances, protrude through the surface (arrows, F).

Uniaxial mechanical responses of composite sheet. Samples were initially preconditioned to 8% strain to obtain stable mechanical responses. Preconditioning enhanced resilience, and introduced a small amount of residual strain (Figure 3.8). The effect of fiber fraction and orientation was apparent in average tensile responses (Figures 3.9, 3.10). When fiber was oriented parallel or at 15° to the loading direction, stress-strain curves were linear between 2 and 12 or 14% strain. The initial non-linearity up to 2% strain reflected artifact due sample misalignment and slack due to residual strain induced by preconditioning. Young's Modulus was measured from a linear fit between 4 and 10% strain. The slope of the stress-strain response above a strain of 12 to 14 % decreased for samples in which fibers were orientated at 0° or 15°. This transition reflected yielding of the fiber network at average stresses 1.31 to 2.87 MPa depending on the fiber layout. Substantial hysteresis between the loading and unloading curves was observed upon yielding of the fiber network due to irrecoverable loss of mechanical energy in this loading cycle (Figure 3.9 and 3.10, panel B). Similar yielding behavior was not observed in designs without fiber, or when fibers were perpendicular to the loading direction. Mechanical parameters including yield stress, Young's Modulus, ultimate tensile stress, and strain-to-failure for all fiber layouts are summarized in Table 3.2. Designs with greater fractions of fiber, or with fiber parallel rather than perpendicular to the loading direction, demonstrated enhanced resilience (Figure 3.11). Increasing fiber fraction also elevated the Young's Modulus and yield stress but did not significantly alter ultimate tensile stress (Figure 3.12). Layouts with fiber orientation more closely aligned to the loading directions also displayed increased Young's Modulus and ultimate tensile strength. Collectively, mechanical analysis indicated the capacity to increase Young's

Modulus by up to a factor of five, and enhance resilience from 53.1 ± 1.4% to 76.1 ± 2.9%. Resilience, or elastic efficiency, measures the energy stored and returned during a loading-unloading cycle. The high resilience of many tissues contributes to their ability to transmit energy and resist fatigue during cyclic loading, and native collagen and elastin are both highly resilient [80].

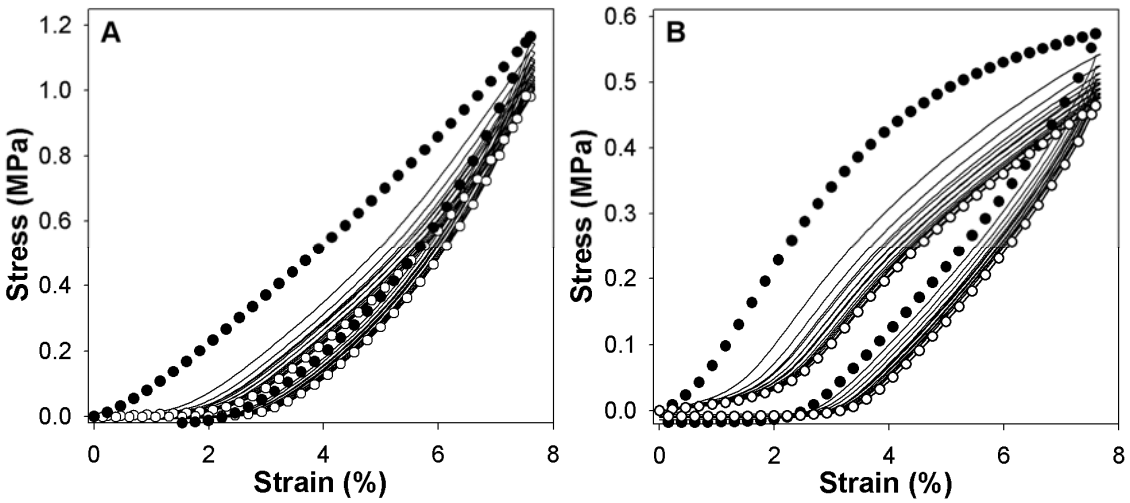

Figure 3.8. Uniaxial mechanical response of a composite sheet with (A) or without collagen fiber (B) over a period of cyclic loading to 8% strain. Collagen fiber was oriented at 15° and a volume fraction of 17% in (A). Between the first loading cycle (●) and sixteenth loading cycle (○), the material became less stiff, and 1-2% residual strain was introduced. The difference between intermediate cycles (—) diminished as the cycle number increased.

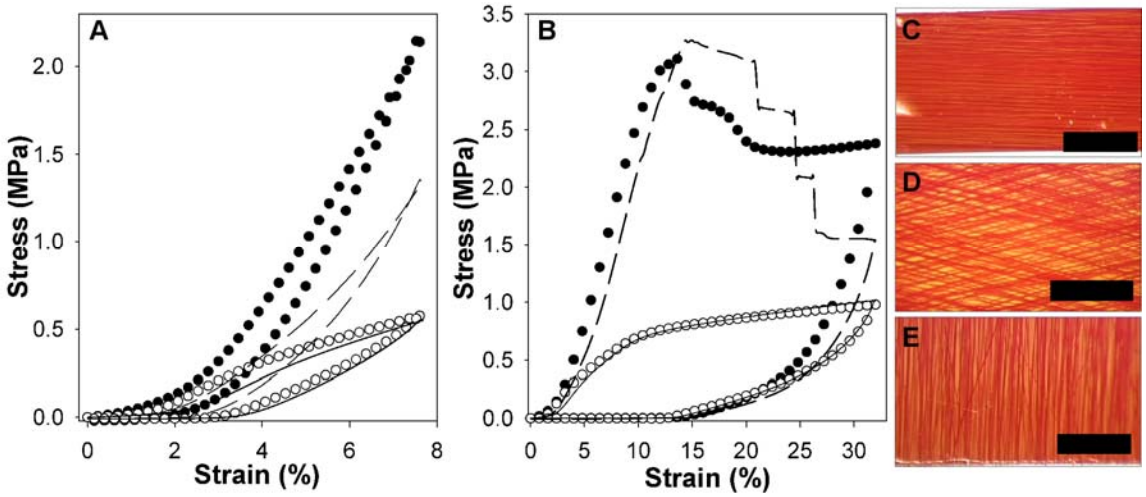

Figure 3.9. Stress-strain response of fiber composite sheets of varying fiber orientation, but with fixed fiber volume fraction. Composites with fiber angles of 0° (●), 15° (---), 90° (—), and without fiber (○) were tested at low and high strains (A, B). Photographs of collagen fiber layouts for 0, 15, and 90° layouts are shown in C, D, and E respectively. Scale bars are 2 mm.

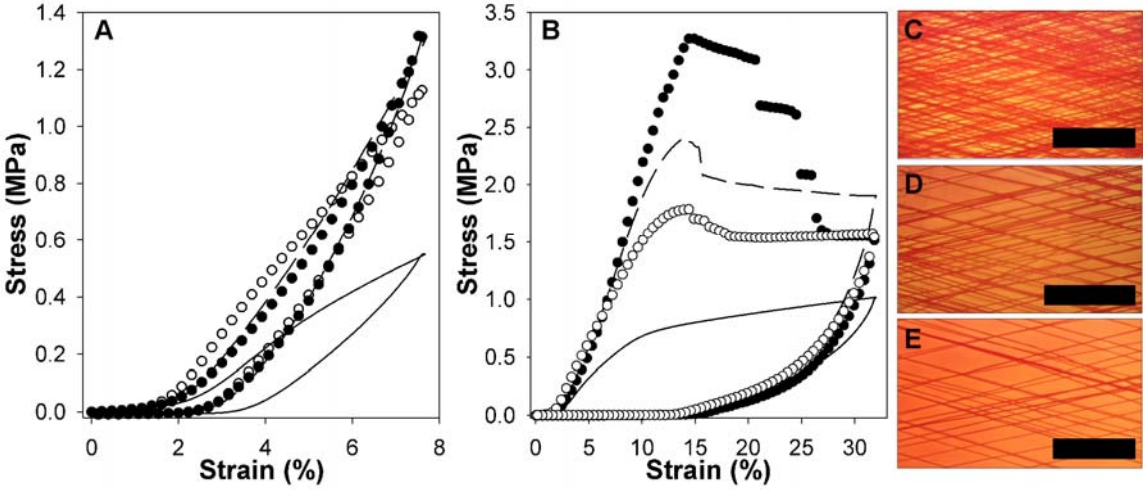

Figure 3.10. Stress-strain response at varying fiber volume fraction. Composites with average fiber fractions of 17% (●), 7% (---), and 3% (○), and without fiber (—) were tested at low and high strains (A, B). Photographs of collagen fiber layouts were taken after staining (C, D, and E). Scale bars are 2 mm.

Table 3.2. Mechanical Properties of APPLES Designs

Design	Volume Fraction (%)	Fiber Orientation (º)	Young's Modulus (MPa)	Yield Stress (MPa)	Yield Strain (%)	UTS (MPa)	Resilience (%)	Strain to failure (%)	n
1	16.3 ± 0.6	0	33.1 ± 3.9	2.87 ± 0.56	12 ± 1	3.62 ± 1.07	76.1 ± 2.9	31± 10	5
2†	16.7 ± 0.5	90	5.3 ± 0.6	-	-	1.99 ± 0.28	50.8 ± 0.6	184 ± 38	5
3	17.7 ± 0.8	15	26.0 ± 4.1	2.58 ± 0.37	14 ± 1	2.66 ± 0.72	75.8 ± 2.0	23 ± 3	6
4	6.8 ± 0.3	15	20.9 ± 2.0	1.87 ± 0.34	13 ± 2	2.41 ± 0.17	71.9 ± 2.1	47 ± 7	6
5	3.1 ± 0.1	15	13.9 ± 1.36	1.31 ± 0.19	12 ± 1	1.85 ± 0.66	66.8 ± 1.4	182 ± 135	7
6†	-	-	6.1 ± 0.7	-	-	4.08 ± 0.80	53.1 ± 1.4	314 ± 26	5

†Designs without fiber (6) or with fibers oriented perpendicular to loading (2) did not display abrupt yielding points.

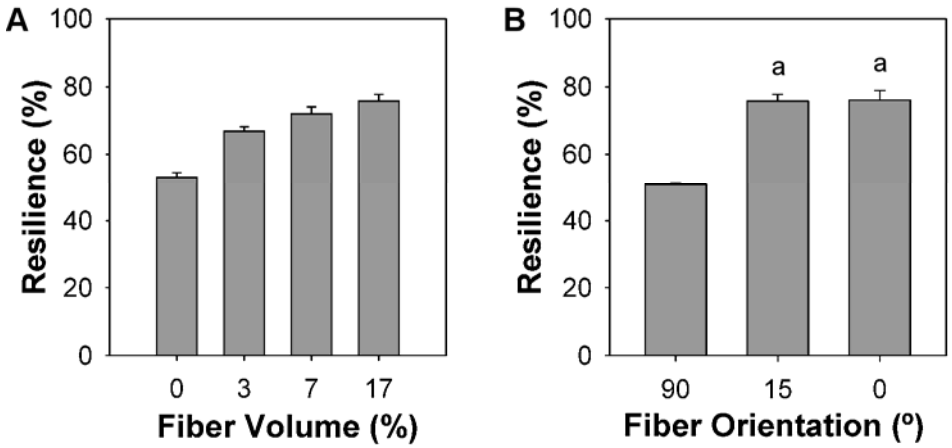

Figure 3.11. Dependence of resilience on fiber volume and orientation. Resilience increased with increasing fiber fraction (A). Layouts with fibers closer to the loading direction, with orientations of 15° and 0°, were more resilient than layouts with a fiber orientation of 90°, perpendicular to the loading direction (B). Bars without letter labels are significantly different from all other bars ($p<0.05$). Bars with the same letter are not statistically different from each other.

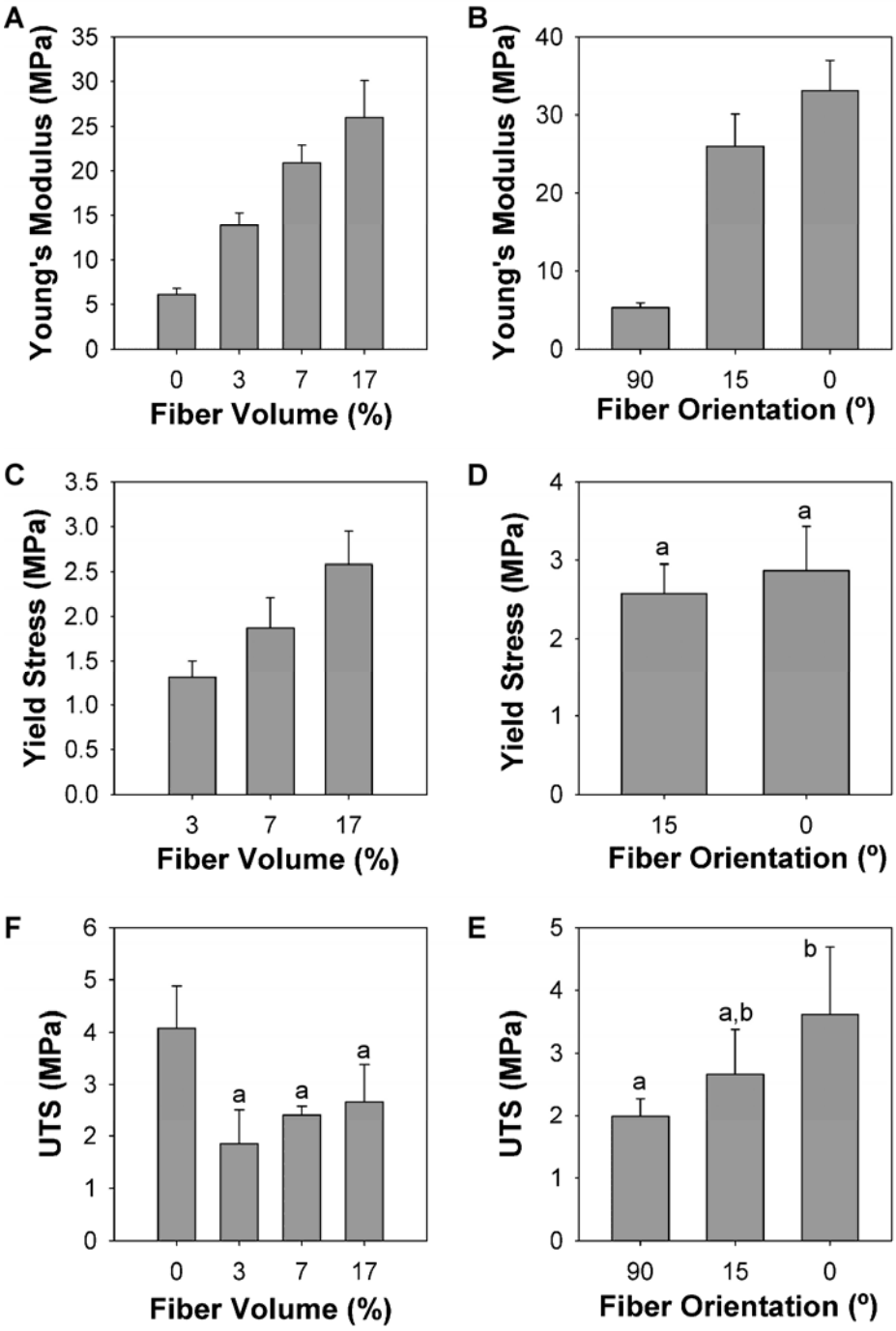

Figure 3.12. Dependence of mechanical properties on fiber fraction and orientation. Increased fiber fraction and alignment to the loading direction increased modulus (A, B). Increased fiber fraction elevated the yield stress, while adjusting fiber orientation from 15° to 0° did not significantly change yield stress (C, D). Increased fiber fraction did not significantly enhance UTS (F). Alignment of fibers in the loading direction resulting greater ultimate stress compared to alignment perpendicular to the load (E). Bars without labels are significantly different from all other bars ($p<0.05$). Bars with the same letter are not statistically different from each other.

Sample analysis after rupture revealed four modes of failure in tension related to fiber volume fraction and orientation (Figure 3.13). A primary failure of the elastin-like protein matrix was observed when the construct was fabricated without fibers or fibers that were oriented such that they were not the primary load bearing element of the sample. Typically, a 4.08 ± 0.80 MPa stress and 314 ± 26% strain resulted in the failure of the elastin matrix analogue. When fibers oriented perpendicular to the loading direction were added to the elastin-like matrix, the ultimate tensile stress and the strain-to-failure and the decreased to 1.99 ± 0.28 MPa and 184 ± 38%, although the stress-strain curve was similar prior to tensile failure. Layouts with 7 or 17% fiber fraction oriented at 0 or 15° to the loading direction demonstrated the fiber network yielding behavior discussed above, followed by strain-to-failure values of 20 to 50%. The relatively lower strain-to-failure in these samples occurred because the fiber network yielded in one or two discrete locations. After yielding, it is likely that local strains in these regions were higher than the overall sample strain, resulting in tensile failure in these regions. Voids left in the elastin-like protein matrix after fibers yielded and debonded from the matrix would also contribute to tensile failure [95]. A distinct failure mode was observed when fiber fraction was lowered to 3%. In this case, the fiber network demonstrated several yielding events with increasing strain before failure at strains of 182 ± 135%. This pattern occurs when the stress transferred from the ruptured fibers to the matrix is low enough that the matrix itself does not fail, and is known to occur at low fiber volume fractions [95]. Suture pulled out of the protein polymer flex composite in the y direction at 124 ± 8 gf, and in the x direction at 170 ± 36 gf.

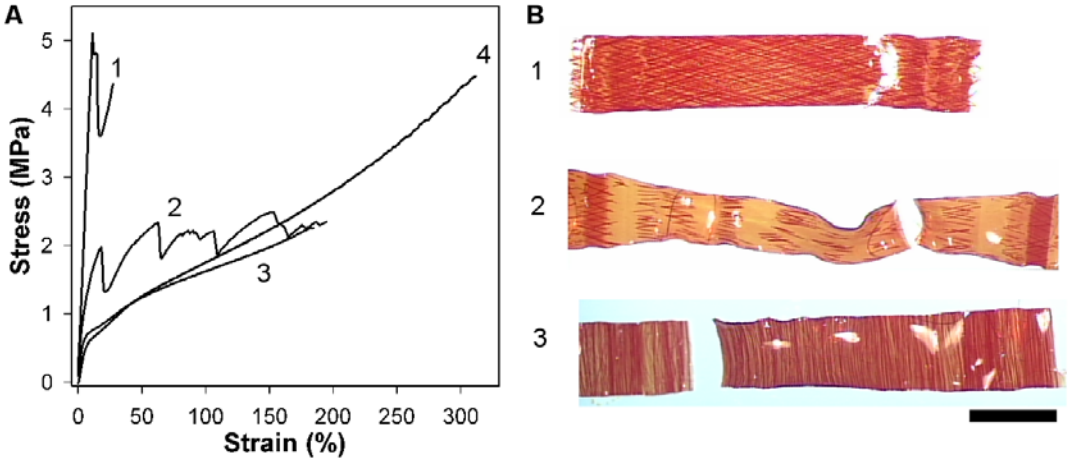

Figure 3.13. Four modes of failure were observed for composite sheets that reflected patterns of fiber orientation and volume fraction. At fiber orientations close to the loading direction and fiber fractions of 7 or 17%, samples exhibited failure soon after a single yielding (Mode 1 in panels A, B). At fiber fractions of 3%, the fiber network yielded at several different locations and levels of strain before tensile failure (Mode 2). Fiber oriented perpendicular to loading generated smooth deformation followed by failure at moderate strain (Mode 3). Samples without fiber deformed smoothly and tended to fail at higher levels of strain (Mode 4).

Aqueous solutions of the triblock elastin-mimetic protein polymer are capable of a sol-gel transition, which permits incorporation of a fiber layout into a single 40 μm thick membrane and subsequent bonding of a multilayer membrane stack. The fiber layouts consisted of closely spaced fibers with two predominate orientation angles, resembling several native tissues including the linea alba of the anterior abdominal wall [96], small intestinal submucosa [97, 98], and the annulus fibrosis of intervertebral discs [99]. The laminated geometry resembles cell sheet tissue engineering methods investigated by others [85, 100] and it may be possible to incorporate living cells at controlled spatial intervals through the sheet thickness. The use of a recombinant protein matrix and synthetic protein microfibers affords control over compliance, resilience, strength, and anisotropy not available with cell sheet tissue engineering strategies and obviates the long culture time required for the development of cell-secreted collagen layers.

CONCLUSIONS

The development of substitute extracellular matrix proteins, and technologies to produce the desired geometries in three dimensions, may enable improved non-living and tissue-engineered implants. The flexible, elastic protein polymer fiber composites developed in this study represents a step toward this goal. Through the development of a fiber embedding and lamination process, composite sheets with controlled mechanical anisotropy, and increased modulus, yield strength, resilience, and suture retention strength were created.

CHAPTER 4

MICROCRIMPED COLLAGEN FIBER COMPOSITES

INTRODUCTION

Collagen fibers exhibit a waviness, or crimp, in a diversity of tissues including tendon [101], ligament, intestine, blood vessel [102], heart valve leaflet, intervertebral discs, the intra-articular disc of the temporomandibular joint [103], and others [99]. The wavelength of crimp varies between 10 to 200 μm, and the shape has been characterized as a planar zig-zag [99], a planar sinusoid [102], and a 3D helix [104, 105]. In several instances, researchers have observed that crimp disappears as soft tissues are stretched, and simultaneously the tissue transitions from low to high stiffness [81, 101, 106]. Crimp is thought to represent redundancy in the collagen network, which only partially contributes to the overall resistance to deformation at low stretch levels. At higher stretch, collagen fibers un-crimp and/or rotate into alignment with the direction of tension, stiffening the tissue by bearing an increased share of the load. Consequently, crimping is one of the features of collagen fiber architectures that allow tissues to be both compliant and strong. This combination contributes to significant biomechanical phenomena such as the efficient opening and sealing of heart valves [82], the propensity of tendon to smoothly absorb load, and the compliance of arteries.

In Chapter 3 we developed protocols to fabricate laminated composites of collagen fiber embedded in elastin-mimetic protein. Although this fabrication scheme increased strength and resilience and presented the capacity to tailor mechanical anisotropy, the composites did not display the mechanical transition point behavior

observed in many native tissues. Although the laminated sheets differed from native protein fiber networks in several respects, we postulated that the lack of transition point was largely due to absence of crimp in the collagen fiber component.

The biomechanical significance of collagen fiber architectures motivated the development of a soft tissue substitute replicating crimp structure and function. The goal of this study was to develop a method to fabricate microcrimped sheets of collagen fiber embedded in elastin-mimetic protein.

MATERIALS and METHODS

Synthesis of a recombinant elastin-mimetic triblock protein polymer. Genetic engineering, expression, purification, and characterization of the elastin-mimetic protein polymer, designated **LysB10,** has been described elsewhere [2]. Briefly, the flanking 75 kDa endblocks of the protein polymer contained 33 repeats of the hydrophobic pentapeptide sequence $[IPAVG]_5$, and the central 58 kDa midblock consisted of 28 repeats of the elastic, hydrophilic sequence $[(VPGAG)_2VPGEG(VPGAG)_2]$. The sequences between blocks and at the C terminus include the residues, [KAAK], provides amine groups for chemical crosslinking.

The protein polymer sequence was contained a single contiguous reading frame within the plasmid pET24-a, which was used to transform the *E. coli* expression strain BL21(DE3). Fermentation was performed at 37°C in Circle Grow (QBIOgene) medium supplemented with kanamycin (50 μg/mL) in a 100 L fermentor at the Bioexpression and Fermentation Facility, University of Georgia. Cultures were incubated under antibiotic selection for 24 hr at 37°C. Isolation of the **LysB10** consisted of breaking the cells with freeze / thaw cycles and sonication, a high speed centrifugation (20,000 RCF, 40 min,

4°C) with 0.5% poly(ethyleneimine) to precipitate nucleic acids, and a series of alternating warm / cold centrifugations. Each cold centrifugation (20,000 RCF, 40 min, 4°C) was followed by the addition of NaCl to 2M to precipitate the protein polymer as it incubated for 25 min at 25°C. This was followed by warm centrifugation (9500 RCF, 15 min, 25) and resuspension of the pellet in cold, sterile PBS on ice for 10 – 20 min. After 6 to 10 cycles, when minimal contamination was recovered in the final cold centrifugation, the material was subject to a warm centrifugation, resuspended in cold sterile PBS, dialyzed, and lyophilized.

Isolation and purification of monomeric collagen. Acid-soluble, monomeric rat-tail tendon collagen (MRTC) was obtained from Sprague-Dawley rat tails following Silver and Trelstad [46]. Frozen rat tails (Pel-Freez Biologicals, Rogers, AK) were thawed at room temperature and tendon was extracted with a wire stripper, immersed in 10 mM HCl (pH 2.0; 150 mL per tail) and stirred for 4 hr at room temperature. Soluble collagen was separated by centrifugation at 30,000 *g* and 4°C for 30 minutes followed by sequential filtration through P8, 0.45 µm, and 0.2 µm membranes. Addition of concentrated NaCl in 10 mM HCl to a net salt concentration of 0.7 M, followed by 1 hr stirring and 1 hr centrifugation at 30,000 *g* and 4°C, precipitated the collagen. After overnight re-dissolution in 10 mM HCl the material was dialyzed against 20 mM phosphate buffer for at least 8 hr at room temperature. Subsequent dialysis was performed against 20 mM phosphate buffer at 4°C for at least 8 hr and against 10 mM HCl at 4°C overnight. The resulting MRTC solution was stored at 4°C for the short-term or frozen and lyophilized.

Production of a synthetic collagen microfiber by continuous co-extrusion. A modified wet spinning device facilitated collagen fiber production. A collagen solution (5 mg/mL in 10 mM HCl) and wet spinning buffer (WSB: 10 wt% poly (ethylene glycol) Mw = 35000, 4.14 mg/mL monobasic sodium phosphate, 12.1 mg/mL dibasic sodium phosphate, 6.86 mg/mL TES (N-tris (hydroxymethyl) methyl-2-aminoethane sulfonic acid sodium salt), 7.89 mg/mL sodium chloride, pH 8.0) were extruded with a dual syringe pump (Harvard Apparatus, Holliston, MA). The collagen solution emerged through a 0.4 mm inner diameter blunt-tipped needle into the center of a vertical tube (1.6 mm inner-diameter x 1 m long fluoropolymer tubing) at 0.08 mL/min. Wet spinning buffer simultaneously advanced through a bubble trap and down the fluoropolymer tube at a rate of 1.0 mL/min. As it exited the extrusion needle, the collagen coagulated into a gel-like fiber and was carried downward by the WSB stream. Upon emergence from the fluoropolymer tube, the fiber entered a 2 meter-long rinsing bath of 70% ethanol in water. Continuous fiber was produced and collected by winding it out of the rinsing bath onto segments of polyvinyl chloride (PVC) pipe that rotated and translated automatically. After spinning, the fiber was placed in fiber incubation buffer (FIB: 7.89 mg/mL sodium chloride, 4.26 mg/mL dibasic sodium phosphate, 10 mM Tris, pH = 7.4) [47] at 37°C for 48 hr. Fiber was incubated directly on the PVC pipe segments used for collection. Subsequently, pipe segments containing continuous fiber were rinsed in ddH20 for 15 min before drying and collecting the fiber under tension with an automated system. Before microcrimping, the fiber was arranged into dense parallel sheets by winding about rectangular frames. The frames were rotated at 40 rpm by a DC gearmotor and translated at 7 mm/min by an automated linear actuator (Velmex, Inc, Bloomfied, NY). Digital

photographs of the array of fibers on the frame showed that the average fiber spacing was 190 ± 10 μm. Two additional fiber layers were wound onto the frame, over the first layer, to reduce the average fiber spacing to 63 μm. For single-fiber mechanical testing, only ten fibers were crimped at a time. In this case the fibers were separated by 1 to 2 mm, so that after crimping individual fibers could be readily obtained.

Fabrication of defined patterns of parallel microridge arrays in flexible template membranes. Three microridge profiles patterns were designed and tested for the microcrimping system (Figure 4.1). The triangular microridge template was fabricated by spin coating a uniform layer of SU-8 2050 negative photoresist (MicroChem Corp, Newton, MA) onto a silicon wafer. A photomask was applied over the photoresist, and the SU-8 was exposed to 45º inclined ultraviolet light for 70 seconds. Exposure to inclined UV through the photomask crosslinked SU-8 in a 3D pattern consisting of an array of parallel micro-trenches with triangular cross-sections. After removal of the unexposed SU-8 with developer, a 1 μm parylene coating was vapor deposited. Polyurethane solution (PMC 121-30® and PMC® 780, Smooth-On, Inc., Easton, PA) was cast over the parylene-coated SU-8 micro-trench mold and allowed to crosslink for 24 hr, yielding the flexible triangular microridge template (Figure 4.2).

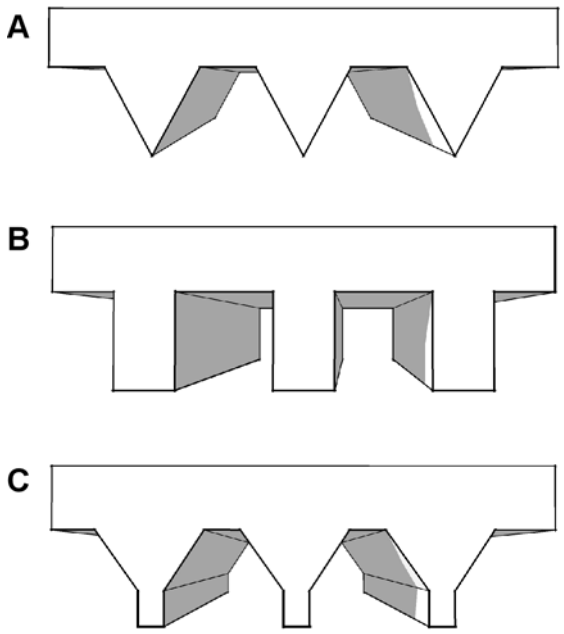

Figure 4.1. Microridge profile patterns included triangular (A), rectangular (B), and chamfered rectangular (C).

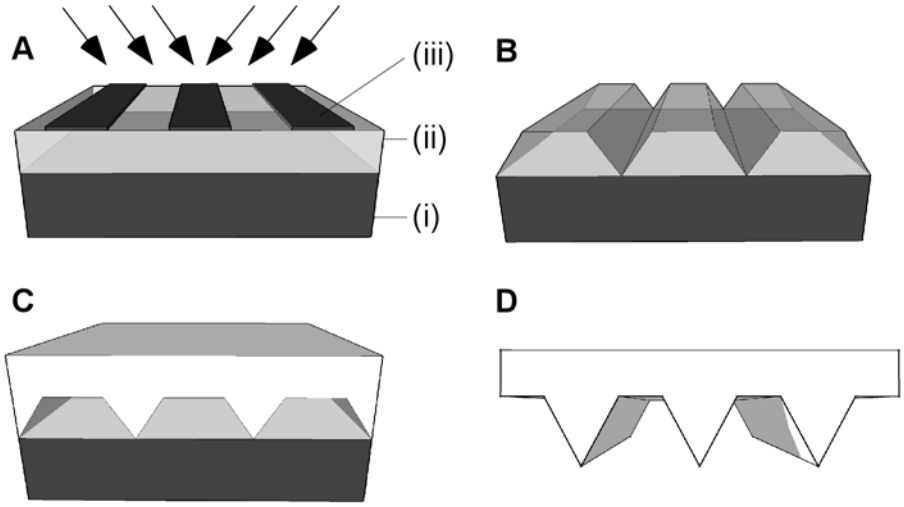

Figure 4.2. Fabrication of the triangular microridge template. A silicon wafer (i) was spin-coated with negative photoresist (ii), and exposed to inclined ultraviolet light through a photomask (iii, A). The repeating strip pattern of the photoresist and the incident angle of the ultraviolet light determined the 3D micropattern of the UV crosslinked photoresist (B). Polyurethane was micromolded over the photoresist to generate the flexible template (C, D).

Rectangular and chamfered rectangular profiles were generated by an alternative process (Figure 4.3). For the generation of rectangular microridges, a layer of positive photoresist (AZ® 4620, Clariant Corp.) was patterned into repeating strips on a silicon wafer, which served as a mask for inductively coupled plasma etching. Inductively coupled plasma etching generated rectangular micro-trenches in the regions of the silicon wafer not shielded by photoresist, at an etch rate of 0.6um/min following the Bosch process. After removal of the photoresist with an acetone rinse and cleaning of the wafer in piranha solution, a layer of parylene was vapor deposited over the micro-trenched silicon wafer. Following parylene deposition, polyurethane was cast over the wafer and allowed to crosslink for 24 hr, generating the flexible rectangular microridge template membrane.

The chamfered rectangular microridge template membrane was produced by a similar process, with the additional step of anisotropic wet etching in a KOH aqueous bath (40 wt%, 70 °C) and an additional molding step. The anisotropic etch was performed subsequent to the inductively coupled plasma etch, converting the rectangular micro-trench geometry into the desired chamfered geometery. After etching parylene was coated over the silicon and polydimethylsiloxane (PDMS, Dow Corning Sylgard 184) was cast over the patterned silicon wafer created a negative of the desired profile. Subsequently, parylene was coated over the PDMS and PU was cast over the coated PDMS to yield the flexible chamfered rectangular microridge template. These templates were fabricated from PU of 30A and 70A durometer.

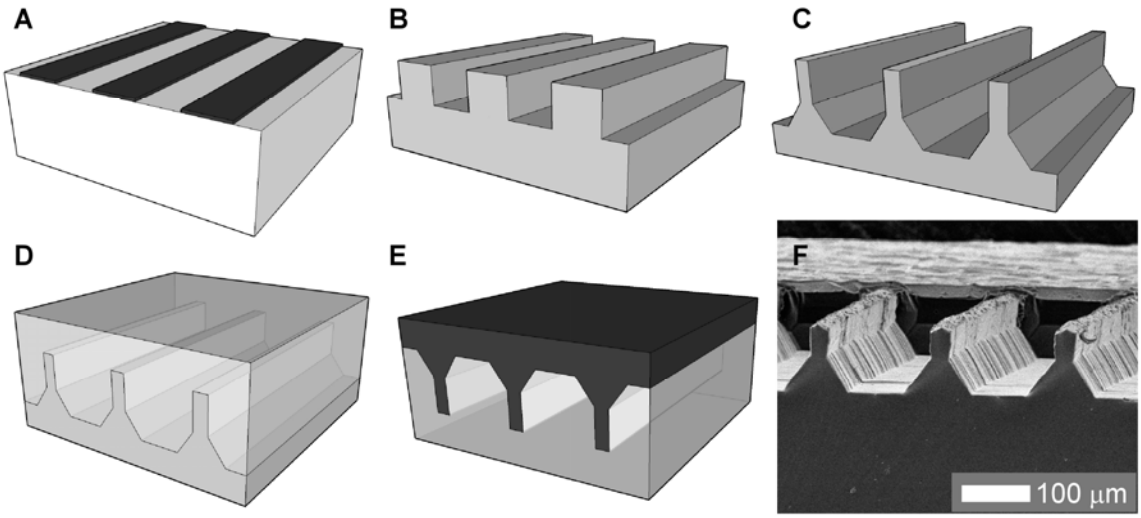

Figure 4.3. Fabrication of defined patterns of parallel chamfered rectangular microridge arrays. A layer of positive photoresist was patterned into strips on a silicon wafer with traditional photolithography techniques (A). The strips served as a mask for inductively coupled plasma etching, yielding rectangular micro-trenches in the silicon (B). To fabricate chamfered rectangular microridges, anisotropic wet etching in an aqueous KOH bath at was performed (C). After parylene coating, PDMS was molded over the template, followed by molding of polyurethane onto the PDMS to yield the parallel chamfered rectangular microridge membrane template (D, E, F). Rectangular microridged templates without the chamfered geometry were generated by a similar process, except after step (B) the silicon was coated with parylene and PU was cast over the silicon template.

Method for scalable microcrimping of synthetic collagen fibers. The microcrimping system consisted of a lead screw assembly, an ultrasoft smooth viscoelastic base membrane (60 OO durometer Sorbothane, Sorbothane, Inc., Kent, OH), the microridged template membrane, and a clamping assembly (Figure 4.4). The base membrane was fastened to the lead screw assembly and a pre-extention of 15 to 55% tensile strain was applied with the lead screw. A parallel array of collagen fiber was transferred from the rectangular winding frame onto the extended base membrane and fastened with tape. The fiber was hydrated with ddH_20 for 15 min, excess water removed, and the flexible microridged template membrane was applied over the hydrated

fiber array. When the microridged template was applied, it was manually extended to the same tensile strain as the pre-extended base membrane, and fastened to the lead screw assembly. Application of the clamping system then secured the collagen fiber between the pre-extended microridged template and the pre-extended base membrane with a normal templating force. Adjustment to the lead screw assembly relaxed the pre-extention simultaneously in both membranes and introduced the microcrimped geometry into the collagen fiber array. The system was frozen at -80°C for 2 hr, warmed to -20°C for 4 hr, and then the clamping assembly and the microridged template membrane were removed. The microcrimped collagen fiber array remained on the base membrane, and was transferred to a room-temperature desiccator saturated with vapor from a 25% glutaraldehyde solution to crosslink the fiber. The base membrane and microcrimped fiber array were remained frozen when placed in the dessicator, so that the hydrated, crimped shape of the fiber was largely held in place as the collagen began to crosslink. After one day, the fiber and the base membrane were removed from the dessicator and allowed to dry in air, yielding a dense, parallel array of microcrimped synthetic collagen fiber. For single-fiber mechanical tests, 8 mm lengths of dried fiber were removed from the base membrane with tweezers and mounted on plastic frames. Initial observations demonstrated that the amount of pre-extention tensile strain, from 15 to 55%, largely dictated the amount of deformation imparted to the fiber and thus the morphology of the microcrimp.

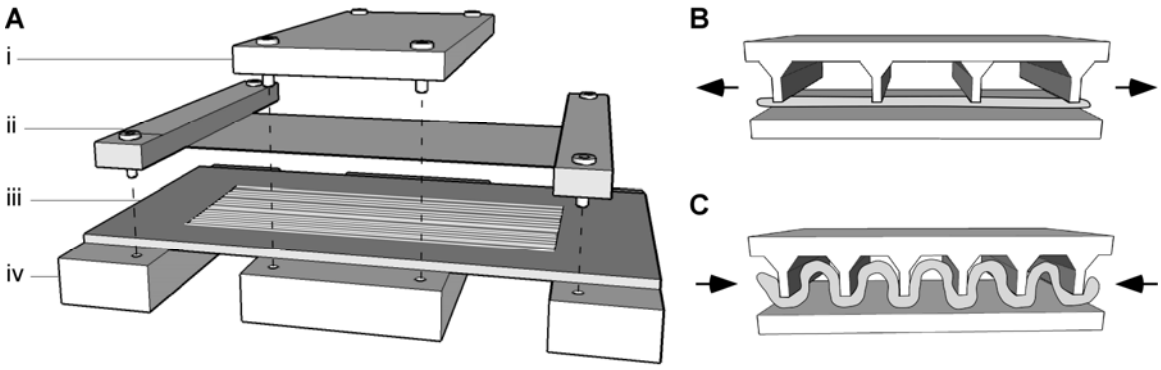

Figure 4.4. Microcrimping system and method. The system, diagrammed in an exploded view (A), consisted of the clamping assembly (i), microridged template membrane (ii), the base membrane (iii), and the lead screw assembly (iv). Pre-extension was applied to the base membrane (iii) with the lead screw assembly (iv). Then, the collagen fiber array was applied to the pre-extended base membrane and hydrated. The microridged template membrane was subsequently applied, with the same degree of pre-extension as the base membrane, and clamped with (i). The pre-extension was relaxed in both the base and the template membranes with the lead screw assembly to generate the microcrimped geometry. Panel (B) illustrates a single collagen fiber clamped between the two pre-extended membranes. After the pre-extension is simultaneously relaxed in both membranes, the fiber becomes microcrimped (C).

Formation of an elastin-like protein polymer lamella with an integrated array of microcrimped collagen fibers. A crimped fiber array, arranged on the base membrane and surrounded by 250 µm thick precision shims (250 µm, Precision Brand, Inc., Downers Grove IL), was frozen at -80°C. A 10 wt% solution of protein polymer was applied to the frozen crimped fiber array after it was initially purged with argon and centrifuged for 5 min at 4°C and 500 g to remove bubbles. An acrylic sheet was used to spread the protein polymer solution as a thin film, which when incubated at room temperature for 25 min gelled around and embedded the crimped fibers. This fiber-reinforced lamella was separated from base membrane after a 5 minute incubation in PBS at 37°C. Microcrimped fiber films were crosslinked in 0.5% glutaraldehyde for 24 hr at

37°C and then rinsed in PBS for 2 hr at 37°C, which was repeated three times. This yielded 80 μm-thick films of crosslinked protein polymer with an embedded array of parallel, microcrimped fiber.

Evolution of the microcrimping system and microridge design. Features of the microridges, including the width, height, spacing, and the stability of the microridge were important to the microcrimping process (Figure 4.5, Figure 4.6). The application of a normal templating force with the clamp assembly proved to be important to maintain parallel alignment of the fibers during microcrimping. We initially fabricated the microridge template membrane from a soft PU (30A durometer) in order to limit potential fiber damage from a stiff, inflexible ridge. However, significant microridge deformation was observed after removal of PU mold following fiber crimping (Figure 4.6). PU of higher durometer (70A) offered sufficient material flexibility to allow for defined membrane pre-extension along with adequate rigidity to prevent microridge collapse upon application of a normal templating force.

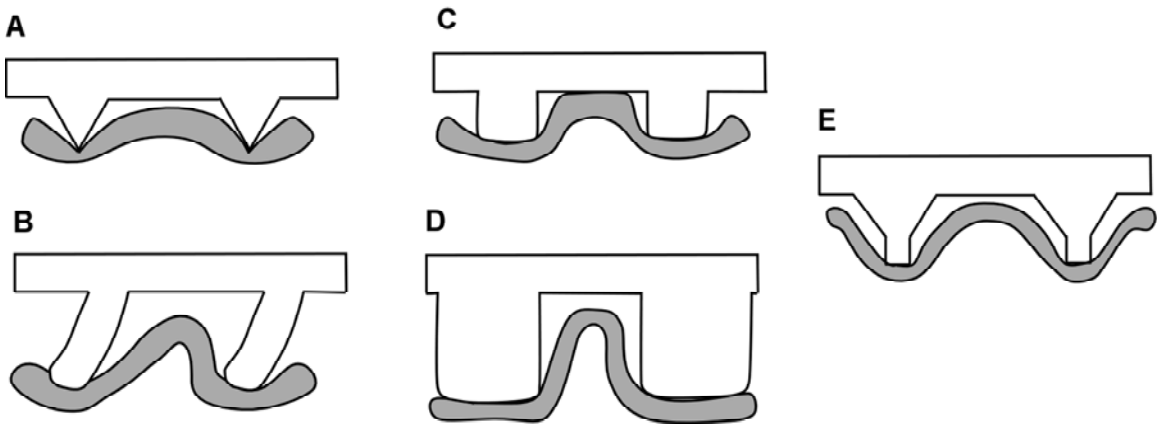

Figure 4.5. Microridge design considerations. The shape of the fiber contacting region of the triangular microridge was too sharp, leading to relatively sharp grooves across the fiber (A). This raised concerns of partial fiber disruption. Tall, thin microridges were unstable, and collapsed. This resulted in non-uniform and unsymmetrical microcrimp (B). If the rectangular microridges were too short, there was not enough overhead space for the fiber fully deform (C). If the microridges were too wide, the fiber contained relatively long, flat segments, limiting the degree of crimp that could be imparted to the fiber (D). Chamfered rectangular microfeatures were selected because the ample overhead space, the relative stability against microridge collapse, and the blunt fiber contacting region (E).

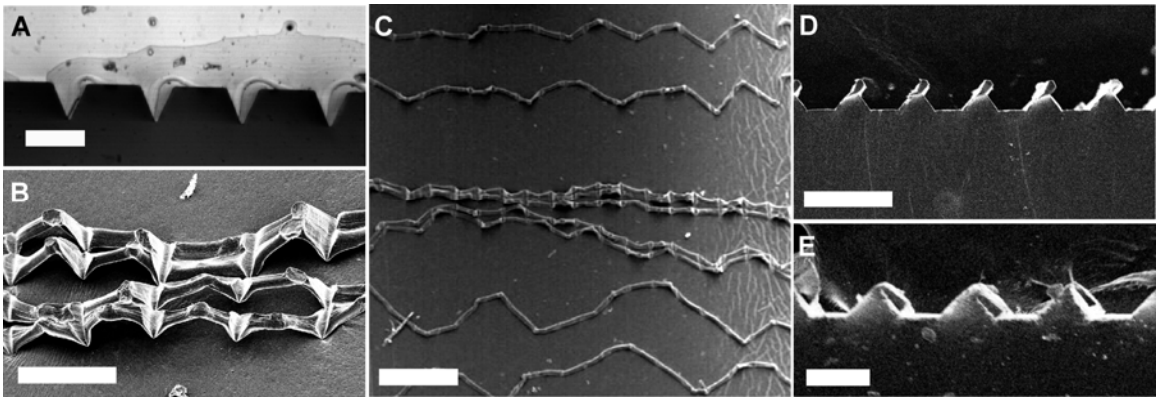

Figure 4.6. Development of the microcrimping process. The triangular micro-ridge (A, optical micrograph, scale = 100μm) inflicted damaging grooves on the collagen fiber (B, SEM, scale = 200μm). When crimped without clamping, fibers often slipped sideways instead of crimping (C, SEM, scale = 500μm). The tops of the chamfered rectangular microridge either tilted over or completely collapsed when the template membrane was fabricated from 30A durometer polyurethane (D and E, SEM, scales = 200 and 100 μm).

Microscopic analysis of fiber crimp. Microcrimped fiber arrays were prepared for scanning electrion microscopy by sputter coating with gold (Emscope SC-500, Emitech, Kent, England), and examined and imaged with a DS-150 F scanning electron microscope (Topcon Co., Tokyo, Japan) operated at 15 kV. Fiber was prepared for confocal laser scanning microscopy (CLSM) by conjugation to tetramethyl rhodamine isothiocyanate (TRITC) [89]. For TRITC conjugation, fiber was wound about a PVC pipe segment placed inside a larger pipe. This arrangement created a 100 mL annular volume in which up to 40 m of fiber could be reacted without tangles or breaks. A 1 mg/mL solution of TRITC in DMSO was added to a 0.1 M sodium carbonate solution to a concentration of 0.05 mg/mL. This solution was added between the pipe segments and stirred for 12 hr at 4°C, after which the fiber was rinsed four times with ddH2O for 2 hr and for 5 min with 70% ethanol and dried in air. Fiber conjugated to TRITC was microcrimped and embedded in elastin-like protein polymer as described above. Samples were examined with an LSM 510 Confocal (Carl Ziess MicroImaging, Oberkochen, Germany) using a 543 nm Helium-Neon laser and a 10x objective. Three-dimensional projections were created from stacks of 25 to 35 optical slices taken at 3 to 6 μm intervals using LSM Image Broswer software (Carl Ziess MicroImaging, Oberkochen, Germany). Projections of the crimped fiber were rotated to depict the profile of the microcrimp. The degree of crimp, C, of the embedding and hydrating the fiber assembly was defined as:

$$C = (l_c - l_s) / l_s \text{ x } 100\%$$

where l_c is the length of a line that traced the center of the crimped fiber and l_s is the straight-line distance along the path of the fiber.

Mechanical analysis. Fiber lamella samples, 5 mm in width, 80 μm in thickness and with a gauge length of 12 to 13 mm, were mounted on a dynamic mechanical thermal analyzer (DMTA V, Rheometric Scientific, Inc., Newcastle, DE) with a 15 N load cell in an inverted orientation and immersed in a jacketed beaker of PBS at 37°C. Samples were oriented such that the direction of tensile stress was parallel to the embedded fibers. Three to four samples of embedded, uncrimped fiber, fiber microcrimped with 15% pre-extention, and fiber microcrimped with 30% pre-extention were tested. Samples were allowed to equilibrate in PBS for 5 min and strained to failure. Engineering stress and strain were reported. The transition point strain, the level of strain at which the material progressed from compliant deformation to high modulus deformation, was quantified for all stress-strain curves. The transition point strain was defined as the x-intercept of a straight line fit to the last 4% strain prior to sample yielding.

To assess the effect of cyclic loading on microcrimp morphology, samples were examined by confocal laser scanning microscopy before and after 15 and 1000 cycles of loading to 10% strain. The failure strength of individual crimped fibers was also measured in tension. Non-embedded fibers were allowed to dry after microcrimping and crosslinking, removed from the base membrane and mounted on a plastic frame with cyanoacrylate glue. Fibers microcrimped with 15 and 30% pre-extenion were evaluated (n=8, n=4 respectively). Fibers were hydrated in PBS for 2 hr, and mounted in the DMTA. The plastic frame supporting the fiber was cut away and fibers were pulled to failure. All tests were performed at a rate of 5 mm/min in PBS at 37ºC.

Controlled deformation of a flexible template dictates periodic microcrimp morphology. Scanning electron microscopy indicated that after the crimping, vapor crosslinking, and drying on the base membrane, a regular crimp pattern was introduced into the fiber arrays (Figure 4.7, Figure 4.8). Upon pre-extension of the template to 30 or 40% beyond the resting length, the crimp consisted of relatively smooth arcs, while deforming to 45 and 50% led to some sagging of the crimp peaks. At low magnification, the crimp pattern appeared consistent over a scale of several millimeters (Figure 4.9). However, occasional irregularities at the peak of the crimp suggest that in some areas the fiber may have buckled. In addition, angular imprints were observed at contact points along the fiber, although less severe than those produced by triangular microridge features.

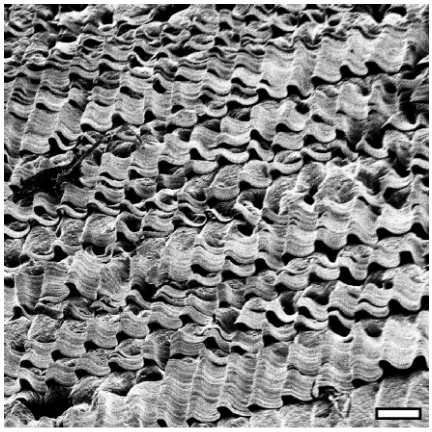

Figure 4.7. Scanning electron microscopy of a microcrimped collagen fiber array (scale 200 μm).

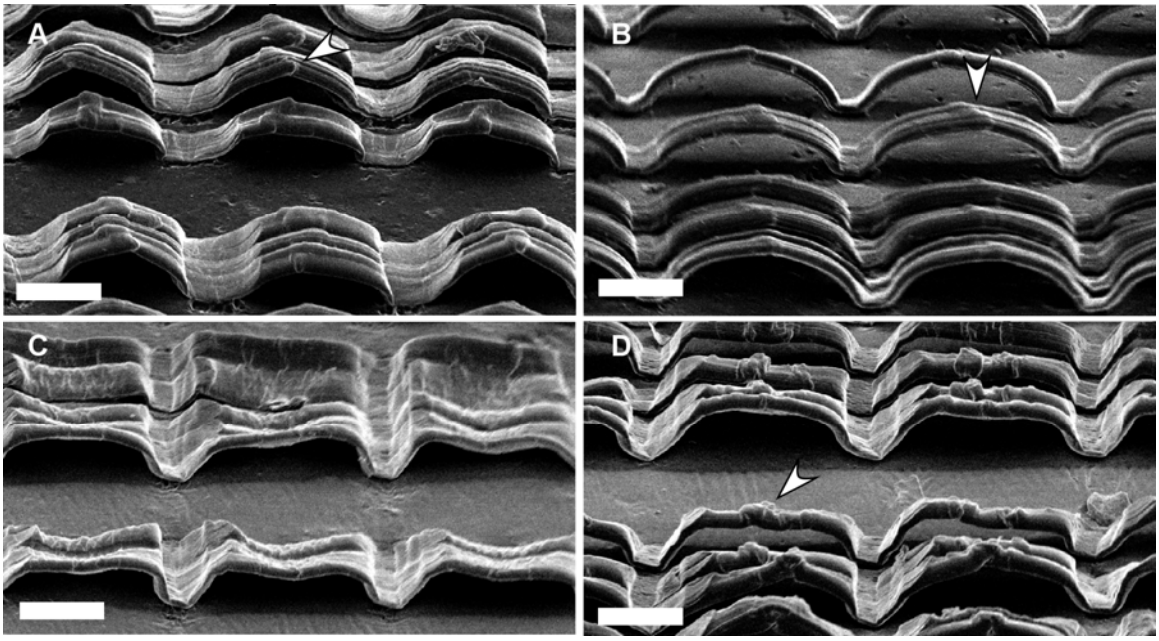

Figure 4.8. Dependence of crimp morphology on pre-extension. Fiber arrays microcrimped with 30, 40, 45, and 50% pre-extension of the chamfered rectangular template demonstrated varying morphologies (A-D, respectively. Scale = 50 μm). For 45 and 50% pre-extension, the crimp shape appeared flattened rather than bending upwards in a smooth arc. Evidence that the fibers buckled during crimping (white arrows) was more severe in the 50% pre-extension sample.

Three-dimensional reconstructions from CLSM of embedded fiber lamellae demonstrated that crimp geometry was preserved after fiber embedding in the elastin-mimetic protein polymer and imaging in the hydrated state (Figure 4.9). The induced crimp curvature depended upon the level of applied membrane pre-extension. For example, the degree of crimp as measured from CLSM reconstructions was 3.1 ± 0.4 % and 9.4 ± 2.9 % for fibers crimped by membrane deformation of 15 and 30%, respectively (Figure 4.10). Ideally, the applied pre-extension and the degree of crimp imparted to the fiber should be equivalent, however reduced crimp might be anticipated if the fiber length is not constant during microcrimping. Specifically, fiber length may have decreased during the crosslinking and drying steps. These steps were designed to

crosslink the fiber while the hydrated microcrimp morphology was frozen in place. However, during the 24 hr crosslinking period, the fiber arrays thawed and partly dried. The real crosslinked geometry was therefore in between the swelled, hydrated geometry and the contracted, dry geometry. If partial drying reduced fiber length, would have also reduced the degree of crimp. The hydrated geometry may not be fully restored during the embedding step if the elastin-like polymer gels before fully hydrating the fiber. The embedding step may also reduce the degree of crimp if the protein polymer lamella swells after release from the base membrane. Swelling would effectively pull a portion of the crimp out of the fiber. Notably, the microcrimped fiber wavelength before embedding was 127 ± 5 μm, as observed by SEM, and the wavelength hydrated, embedded microcrimped fiber was 143 ± 5 μm, observed by CLSM. This relative increase of 13% may indicate swelling of the protein polymer lamella that could reduce the degree of crimp.

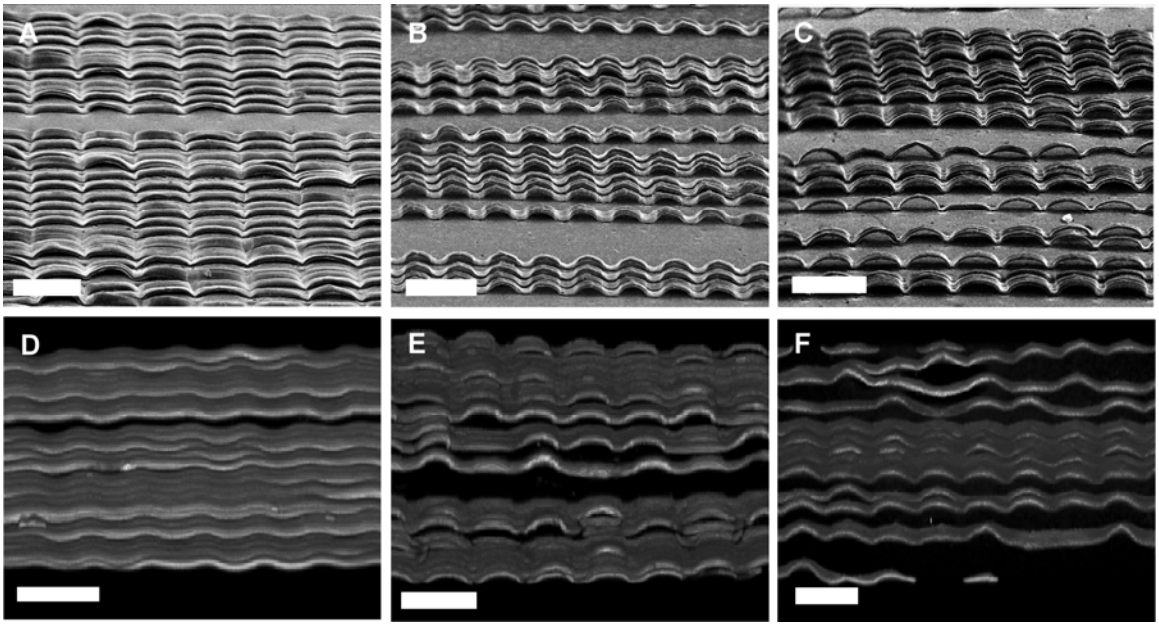

Figure 4.9. Scanning electron micrographs and 3D reconstructions of hydrated, embedded fibers crimped with 15 (A, D), 30 (B, E), and 40% (D, F) pre-stretch. Scale bars 200 μm.

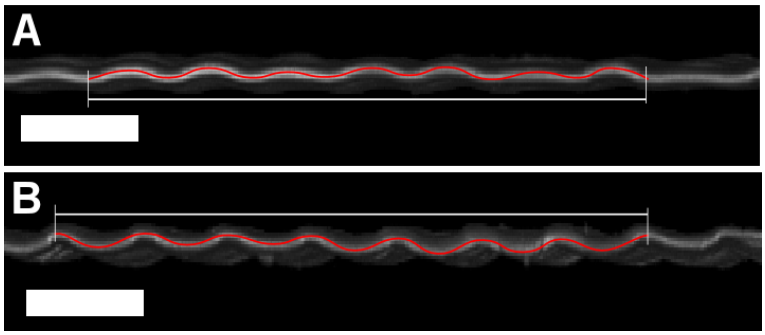

Figure 4.10. Determination of the degree of fiber crimp by rotating 3D images obtained from confocal laser scanning microscopy. Fibers were crimped by 15 (A) or 30% (B) pre-extension. The degree of crimp was defined as the difference in lengths between the straight fiber length (white line) and the path of the crimped fiber (red line) divided by the straight fiber length. Scales are 200 μm.

Microcrimping alters the mechanical response of fiber-reinforced elastin-like matrix composites. Composites displayed a transition between low and high modulus regimes at an extension that was dictated by the degree of fiber crimp (Figure 4.11). The observed level of strain at the calculated transition point was 1.1 ± 0.2 %, 4.6 ± 0.9 %, and 13.3 ± 0.7 % for fibers that were non-crimped or had been subject to a pre-extension of 15 % or 30%, respectively. Non-crimped fibers display a transition at very low strain due to imperfect sample loading and alignment. Notably, the strain at which each transition occurred was very close to the measured degree of crimp (0% vs 1.1%; 3.1% vs 4.6%; 9.4% vs 13.3%). Mechanical testing also demonstrated that the crimp structure was not lost during cyclic loading. Samples subjected to 15 and 1000 loading cycles did not demonstrate a notable change in the degree of crimp (Figure 4.12; 10.2 ± 2.0 %, 9.4 ± 2.9 %, and 8.8 ± 1.4% for zero, 15, and 1000 cycles).

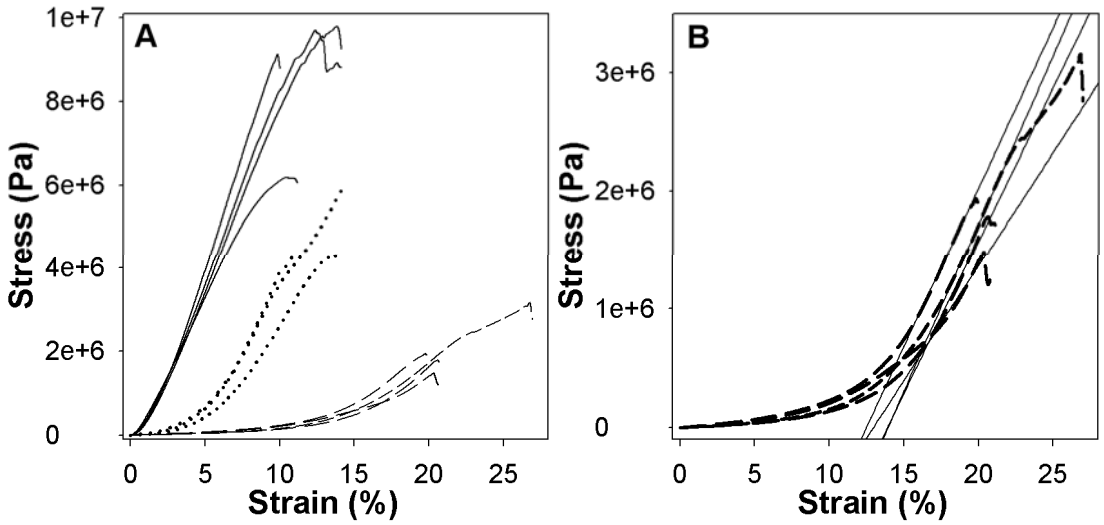

Figure 4.11. (A) Uniaxial stress-strain behavior for composite lamellae containing microcrimped fibers aligned parallel to the direction of the imposed load. The degree of crimp influenced the mechanical response. Non-crimped fiber (solid), 15% pre-stretch (dotted), and 30% pre-stretch (dashed). (B) Stress-strain response of a composite membrane reinforced with fibers in which crimp was induced by a pre-extension of 30%.

Table 4.1. Mechanical Properties of Microcrimped Lamellae†

Pre-extension (%)	Young's Modulus 1 (MPa)	**Young's Modulus 2 (MPa)**	**Transition (%)**	**UTS (MPa)**	**Strain-to-failure (%)**	**n**
0	-	90.8 ± 14.3	1.1 ± 0.2	8.56 ± 1.64	11.5 ± 1.9	4
15	9.1 ± 1.8	62.2 ± 10.4	4.6 ± 0.9	4.93 ± 0.92	13.1 ± 1.6	3
30	2.2 ± 0.5	25.3 ± 4.1	13.3 ± 0.7	2.08 ± 0.73	21.9 ± 3.3	4

†Young's Modulus 1 and 2 are the slopes of linear fits to the stress-strain response before the transition strain and for the final 4% strain before yielding, respectively.

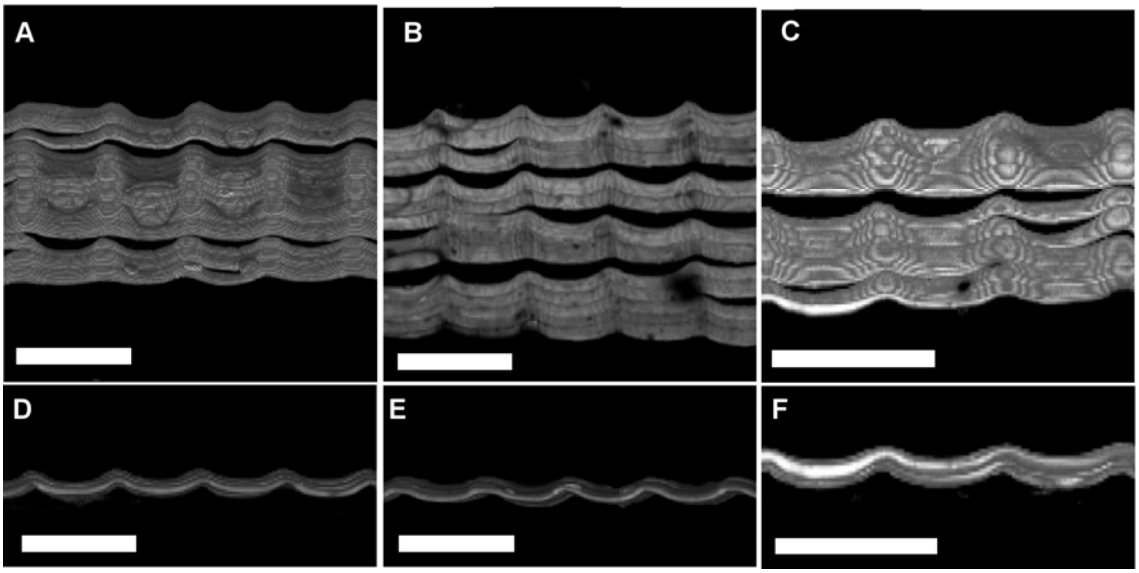

Figure 4.12. Effect of cyclic tensile loading on crimp. Three-dimensional reconstructions of crimped fiber before loading (A, D), after 15 cycles (B, E), and 1000 cycles (C, F) of loading to 10% strain demonstrated that the crimp shape was generally preserved. Scales bars 200 μm.

Fibers were weaker after crimping with an observed failure strength of 2.2 ± 0.5 and 2.1 ± 1.2 g-f for fibers crimped at 15 or 30% pre-stretch, as compared to 8.8 ± 1.7 g-f for non-crimped fibers. Although crimped fiber composites were weaker than their corresponding counterparts composed of non-crimped fibers, it is significant that composite membranes containing fibers crimped at 30% pre-stretch displayed an ultimate tensile strength of 2.08 ± 0.73 MPa, exceeding the strength of many native tissues, such as human urinary bladder (270 ± 140 kPa) [107], pulmonary artery (385 ± 45 kPa) [108], and aorta (1.72 ± 0.89 MPa) [109].

CONCLUSIONS

Oriented arrays of synthetic collagen fibers were created with a microcrimped structure similar in scale to naturally occurring collagen crimp. After embedding microcrimped collagen fiber arrays in a matrix consisting of recombinant, elastin-mimetic protein polymer film, crimp geometry was largely retained. The designed composites demonstrated transition points between low and high modulus regions at a strain that can be predicted by the degree of crimp. The observed mechanical responses for this acellular tissue analogue is similar to that observed for a number of native tissues.

CHAPTER 5

AN ARTIFICIAL BLOOD VESSEL FROM ELASTIN-MIMETIC PROTEIN POLYMER REINFORCED WITH COLLAGEN FIBER

INTRODUCTION

The lack of a clinically successful replacement for the diseased small-diameter artery represents a challenge and opportunity for the fields of biomaterials and tissue engineering. Small to medium (≤4 to ≤7 mm) prosthetic vascular grafts occlude due to peri-anastomotic intimal hyperplasia and surface thrombogenicity. Intimal hyperplasia, the formation of pannus tissue that narrows the lumen of the graft, is driven in part by a compliance mismatch between stiff prosthetics and compliant native artery. Disrupted flow and shear stresses are also driving factors [110]. In this study we developed compliant vascular grafts from recombinant elastin-mimetic protein polymers, reinforced with collagen fiber, as a platform from which to address these challenges.

Improved small-diameter vascular graft technology has been broadly sought and reviewed [111-113]. Research may be categorized as that related to alternative synthetic materials, decellularized allo- and xenogenic tissues, and cell-assembled or tissue engineered matrices. Synthetic materials, especially improved polyurethane, remain an area of interest despite set backs related to in vivo surface chemical modification, hydrolysis, and oxidative biodegradation encountered by early polyurethane formulations [113]. New polyurethanes have exhibited improved biostability, and drug release

strategies or endothelial cell seeding may lower the thrombogenic potential of these grafts. However, concerns remain regarding the carcinogenic potential of degradation products [113], delay of endothelialization caused by drug elution, and the propensity for infection that accompanies any long-term synthetic implant.

Decellularized tissues modified for vascular conduits have included vascular tissues such as human umbilical vein [114-116] and bovine carotid artery [117, 118], and the adaptation of non-vascular tissues, in particular porcine small intestinal submucosa (SIS). Enzymatic and detergent extraction of cells followed by glutaraldehyde crosslinking have been applied to vascular conduits to prevent antigenicity and biodegradation. However, poor patency rates and handling characteristics have limited the use of both human umbilical vein and bovine carotid artery. Tissue heterogeneity, incomplete cell extraction, biodegradation, and the potential risk of viral transmission from animal tissue may impede the application of decellularized tissues.

Technologies for cell-assisted matrix assembly have progressed although many challenges remain. These protocols begin with cells seeded on tubular biodegradable polymer scaffolds, cells suspended in molded biopolymer gels, or cell sheets rolled into tubes. The primary mechanical goal has been the strength to support suturing and arterial pressure levels. To this end, scaffolds were subject at least to 7 – 16 weeks of culture and maturation, yielding burst pressures ranging form 800 – 3500 mm-Hg [85, 87]. Although strong, these versions of the grafts were much stiffer than native artery. In this regard, arterial mechanics depend largely upon the amount and microstructure of collagen, elastin, and smooth muscle cells [119]. Elastin is credited with contributing elastic recoil and compliance to cardiovascular tissues, although more specifically the collagen and

elastin fiber networks may both need to be present with the correct complementary microstructure [81]. Vascular tissue engineers have thus investigated the cell-assisted assembly of elastin with mixed success [85-87], and evidence of organized, concentric sheets of elastin and the resulting resilience and compliance has not been reported. In addition to mechanical issues, cell-assisted matrix assembly technologies must overcome challenges related to the immunologic challenges of allogenic cells, as well as scale-up and quality issues associated with long incubation times.

Several alternative fabrication technologies have been explored in small-diameter vascular graft research to address strength and compliance issues, include filament winding, electrospinning, molding, and sheet wrapping. Filament winding, in which a filament is wrapped about a rotating, translating inner mandrel, allows the compliance and strength of the graft to be adjusted by modulation of the filament angle and density [120, 121]. Like conventional textile grafts, a filament wound structure is permeable and must be filled or coated with a second material. One potential disadvantage of the wound filament technique is that as the graft diameter expands under pulsatile flow, it may contract axially, repeatedly stressing the anastomosis sites [31]. Balancing high compliance and kink resistance with wound filament structures also presents a challenge because circumferentially oriented fibers prevent kinking but restrict compliance while fibers aligned more closely to the axis of the graft do the opposite [120].

In the electrospinning process, a high strength electric field pulls a jet of a charged polymer solution from an extrusion needle, through an air gap, and onto a grounded collecting target. The solution evaporates as it travels through the air gap, transforming the jet into a solid micro- or nanofiber that collects on the target as a

nonwoven fibrous mat. Tubular structures for vascular grafts have been created by electrospinning onto a rotating, translating mandrel. Fiber orientation may be achieved through an expanding library of strategies related to motion of the electrospinning target or shaping of the electric field [122]. In principle, adjustment of fiber orientation should allow control over graft compliance, similar to filament winding. Like other textile techniques, the tubular mesh is highly permeable and must be coated or sealed with a second material. Electrospun tubes have also been reinforced with wound filament, increasing the bursting strength [123]. Depending upon fabrication conditions, electrospinning can be a slow and inefficient process, even with multi-jet spinning heads [124]. We, and others, have electrospun elastin or elastin-mimetic recombinant proteins to serve as one element in an arterial substitute [3, 123, 125-128]. However, another of the seemingly most appropriate materials for a protein-based vascular graft scaffold, pure collagen, has not been electrospun without the use of solvents that denature the protein [53]. Collagen may be blended with polymers or biopolymers and electrospun from non-denaturing solvents, although these fibers may not have the strength of pure collagen [127, 129].

Polymers and some biopolymers such as collagen, fibrin, and elastin can be molded to create tubular structures. Changing the wall thickness of molded tubes results in limited compliance adjustment. Compliance and strength of molding structures has also been modulated by controlling the orientation of fibril networks that develop during the molding process [130] and excimer laser ablation to generate arrays of pores [131]. The desired combination of compliance and strength can also be tuned by surrounding a soft, elastic tube with one or more stiffer tubes [132].

Sheet wrapping approaches are clearly required for grafts fabricated from flat materials such as cell layers [133] and SIS. The technique also provides the opportunity to apply a variety of 2D fabrication techniques, and mimic the laminar structure of the native vessel wall. Automated wrapping devices may increase control and repeatability in these constructs [100]. Tubular elastin scaffolds, extracted from porcine carotid arteries, have been wrapped with SIS [134]. The SIS wrap enhanced burst pressure and suture retention, and although the compliance was not reported numerically the structure was visually similar to native artery under pulsatile conditions.

Here we report a sheet wrapping process that has some characteristics of filament winding. Sheets of the recombinant elastin-mimetic protein, **LysB10**, were reinforced with oriented collagen fiber described in Chapter 2, and wrapped to create a tubular structure. This method created a multi-layer tube reinforced by helical fiber arrays with controlled angle and spacing.

MATERIALS and METHODS

Fabrication of a small diameter vascular graft. Synthetic collagen fibers were arranged into parallel arrays, embedded within a thin membrane of a recombinant elastin analogue, and rolled into multilayered tubes (Figure 5.1). Synthetic collagen fiber was wet spun from rat-tail tendon collagen, as described in Chapter 2, about a rectangular frame rotated by a DC gearmotor and translated by an automated linear actuator (Velmex, Inc, Bloomfied, NY). Rotation and translation speeds were adjusted to control fiber spacing. Fibers underwent vapor phase glutaraldehyde crosslinking by placement in a desiccator containing a 25% (w/v) glutaraldehyde solution for 24 hrs. Two fiber arrays

were then transferred to a glass plate and secured with tape. A protractor beneath the plate was used to align the two arrays to a desired fiber angle or orientation.

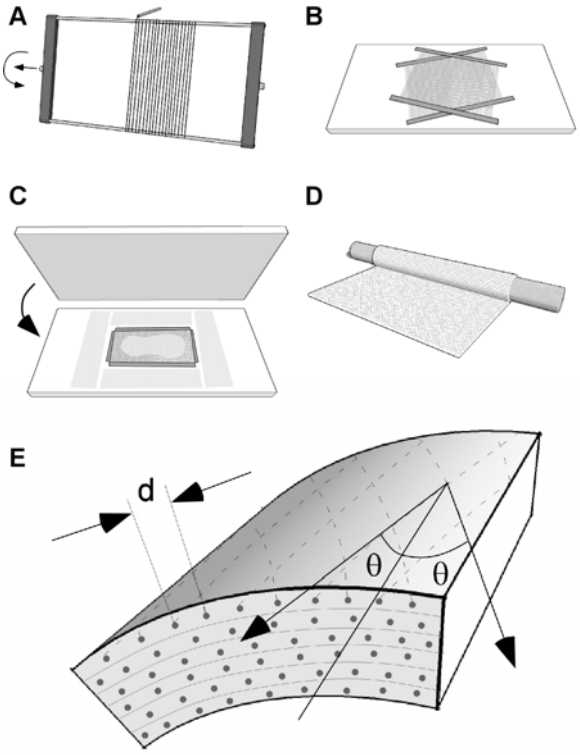

Figure 5.1. Fabrication of a fiber reinforced small diameter vascular graft from oriented synthetic collagen fiber arrays embedded in an elastin protein polymer matrix. (A) Parallel arrays of fiber were created by winding about a frame. (B) Two such arrays were oriented at the desired angle and transferred to a glass sheet. (C) Fiber arrays were surrounded with precision shims and a solution of elastin protein polymer was applied before a polycarbonate sheet was pressed over the fibers to spread the solution into a thin film (D) The gelled film was then rolled about a Teflon tube to create a six-layered tube. (E) Schematic illustrates average fiber spacing (d) and angle (θ).

The elastin-mimetic protein polymer, **LysB10**, was prepared as described in Chapter 3. Solutions of **LysB10** were prepared at 10 wt% concentration in ice-cold ddH_2O. Argon was bubbled through the solutions, followed by centrifugation at 4°C and 500 *g* for 5 min. To embed the fiber layouts, precision 130 μm thick plastic shims

(Precision Brand, Inc., Downers Grove IL) were placed around the layouts, and all embedding materials were cooled to 4°C. The **LysB10** solution was distributed over the fibers and a sheet of polycarbonate was pressed on top of the solution. The fibers and the **LysB10** solution were located within the 130 µm space, sandwiched between the polycarbonate sheet and a glass plate that were separated by precision shims. The embedding assembly was incubated for one hour at 4°C, followed by a 20 min incubation at room temperature. The glass and polycarbonate were pulled apart and the film was separated and trimmed to 5 by 8 cm. The polycarbonate and glass plates were separated affording a 100 µm thick fiber-reinforced protein polymer film.

A 5 x 8 cm film was rolled about a 4 mm diameter Teflon tube to form a 5 cm long, six-layer tube, which was then wrapped in a thermoplastic film. The assembly was incubated at 4 °C overnight to promote interlayer bonding, and then centrifuged at 200 *g* and 4°C for 5 min to remove trapped air bubbles. The assembly was incubated at 37 °C for 180 min, detached from the Teflon mandrel, and hydrated in 37°C PBS for 30 min. Constructs were then thermally annealed at 60°C in PBS for 4 hrs. All constructs were cross-linked in 37°C PBS containing 0.5 % (w/v) glutaraldehyde for 24 hrs and rinsed for 12 hrs in PBS (Table 5.1).

Table 5.1. Synthetic Collagen Fiber Architecture in Graft Designs

Design	Fiber Spacing (mm)	Fiber Angle (°)
1†	-	-
2	0.23	30
3	0.30	30
4	0.15	30
5	0.15	15
6	0.15	22.5

† No fiber

Measurements of vascular graft fiber orientation, spacing and wall thickness. The spacing and orientation of the synthetic collagen fibers were measured from photographs of planar fiber arrays prior to embedding in protein polymer (Figure 5.1, B). Orientation was measured from digital photographs of the fiber layouts using the Inverse Fast-Fourier Transform tool from ImageJ software [88]. After completing vascular graft fabrication, samples were stained with Van Gieson for 5 min, rinsed, and photographed. After exposure to Van Gieson strain, the organization of collagen fibers could be observed on the exterior of the graft. Additionally, three rings were sectioned from each graft, photographed, and wall thickness measured at six points around the circumference of each ring.

Graft pressure-diameter responses and burst pressure. Vascular graft compliance and burst pressure were evaluated using the system diagrammed in Figure 5.2. Grafts were positioned vertically in an acrylic box and submerged in 37°C PBS. As grafts were inflated with PBS supplied by a syringe pump (Harvard Apparatus, Holliston, MA) at 4 mL/min, a 3CCD camera (Dage-MTI, Michagan City, IN) with a 10x macro video zoom lens (Edmund Optics, Barrington, NJ) recorded video at 30 frames per second and pressure was recorded with a pressure transducer (WIKA, Lawrenceville, GA). A PC equipped with data and image acquistion cards (PCI-1405 and PCI-6220, National Instruments, Austin, TX) acquired the video and pressure data. A Labview program synchronized the video and pressure data, collecting video frames and sampling the corresponding pressure measurements at 30 Hz. A MATLAB routine was used to quantify the initial graft outer diameter (D_0) and the inflated diameter (D) from every

video frame and calculated the percent change in diameter (D/D_0) corresponding to each pressure measurement. Each graft was preconditioned with 20 inflations to 250 mm Hg and video taken of the 21st inflation. Grafts were then inflated to failure while video and pressure data was recorded. Compliance (C), the percent change in outer diameter (D/D_0) per 100 mm Hg of applied pressure, was calculated as:

$$C = 1 / b \cdot 100 \quad (1)$$

where b is the slope of a line fit to the pressure vs. D/D_0 curve between 80 and 120 mm Hg.

Suture retention strength. Two 4 mm-long segments were cut from each graft and then sectioned into thirds around the circumference to generate three 4 x 4 mm squares of material. Samples were mounted in a dynamic mechanical thermal analyzer (DMTA V, Rheometric Scientific, Inc., Newcastle, DE) with a 15 N load cell in the inverted orientation, so that samples could be immersed in a jacketed beaker filled with PBS at 37 °C. Prolene suture (4-0) was passed through the sample and fastened to the actuating arm of the instrument. The sample was oriented with the suture 2 mm away from the edge, and pulled parallel to the central axis of the graft. The suture was pulled at a rate of 1 mm/sec and the maximum force measured before the suture tore out was recorded in grams-force (g-f). Five to six samples from each design were tested and the data expressed as mean ± standard deviation.

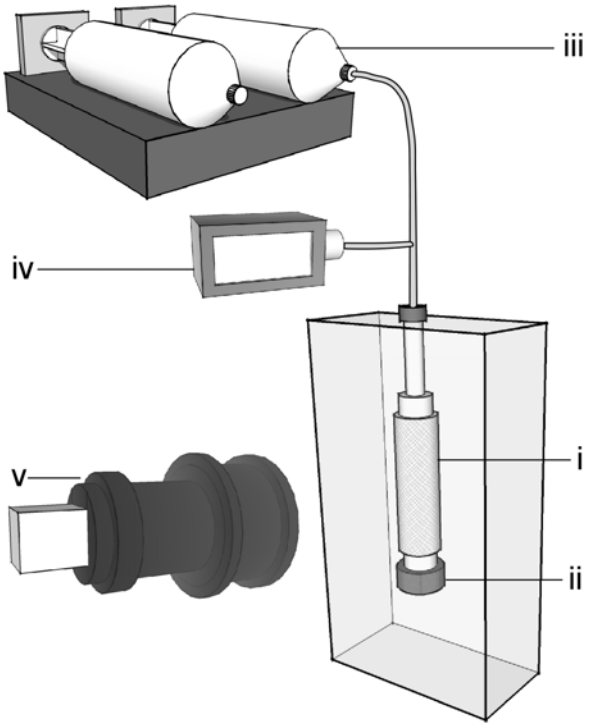

Figure 5.2. System to assess vascular graft pressure-diameter response and burst pressure. The graft (i) was suspended in PBS at 37°C with the lower end plugged with a 5 g weight (ii). As a syringe pump (iii) inflated the graft, a transducer (iv) reported the pressure, and changes to the graft diameter were monitored by video (v).

Scanning electron microscopy. Samples for scanning electron microscopy were cut with a razor blade to expose the lumenal surface and the cross-section of the graft wall. Samples were critical point dried (E3000, Energy Beam Sciences, Inc., East Granby, CT), sputter coated with gold (Emscope SC-500, Emitech, Kent, England), and examined and photographed with a DS-150 F scanning electron microscope (Topcon Co., Tokyo, Japan) operated at 15 kV.

RESULTS and DISCUSSION

Development of a fabrication scheme to create vascular graft composites with controlled fiber orientation and spacing. The fabrication scheme facilitated the

generation of vascular grafts of varying fiber content and architecture. The dimensions of graft prototypes, including fiber spacing and orientation are summarized in Table 5.2 (Figures 5.3, 5.4, 5.5). Although the angle and spacing measured from the fiber layout are close to the nominal values, photographs of the stained prototypes did suggest more variability in the final fiber arrangement. Irregularities in the fiber layout may have been introduced due to swelling of the fiber-reinforced films before rolling them into the graft, stretching of the films during graft rolling, and shrinkage of the structure during thermal annealing. Despite some irregularity, the mechanical properties presented below demonstrated a repeatable dependence on fiber layout.

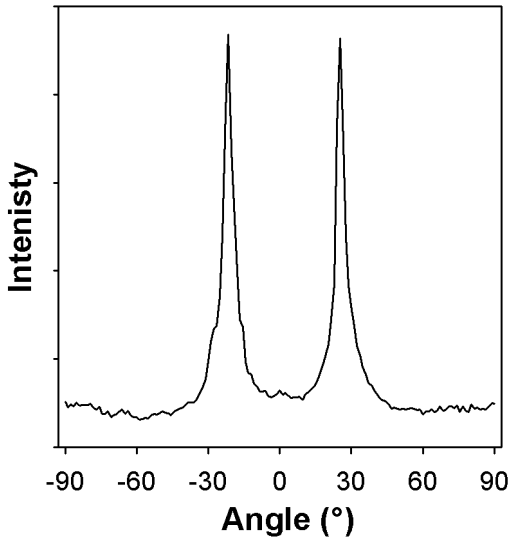

Figure 5.3. Result of Inverse Fast Fourier Transform analysis of fiber orientation. Peaks corresponding to 25.6º and –21.2º represent the primary fiber orientations in this layout, from a graft design with a fiber fraction of 7.3% and nominal angle of 22.5º.

Table 5.2. Synthetic Collagen Fiber Layout and Graft Dimensions†

Design	Fiber Spacing (mm)		Fiber Angle (º)		Fiber Volume (%)	Inner Diameter (mm)	Wall (mm)
	Nominal	Measured	Nominal	Measured			
1	-	-	-	-	0	3.36	1.08
2	0.23	0.22± 0.02	30	30.8 ± 0.3	5.0 ± 0.5	4.57 ± 0.45	0.96 ± 0.10
3	0.30	0.33 ± 0.02	30	30.2 ± 0.7	3.3 ±0.2	5.02 ± 0.19	0.93 ± 0.10
4	0.15	0.17 ± 0.02	30	30.0 ± 1.0	6.4 ± 0.8	4.77 ± 0.39	0.87 ± 0.07
5	0.15	0.15 ± 0.01	15	14.9 ± 1.0	6.5 ± 0.4	4.82 ± 0.26	0.89 ± 0.10
6	0.15	0.14 ± 0.02	22.5	23.4 ± 1.6	7.3 ± 1.0	4.56 ± 0.15	0.84 ± 0.08

†Values represent the mean and standard deviation from three prototypes of each graft design. Design 1 did not contain collagen fiber. Graft diameter is the pressurized inner diameter at 120 mm Hg. The fiber volume fraction was calculated from the mean graft dimensions, fiber dimensions, and fiber spacing. Error in the fiber volume is propagated from the standard deviation of the fiber spacing measurement and other sources of error were ignored. Inner diameter values were calculated by subtracting twice the wall thickness from the outer diameter of the graft.

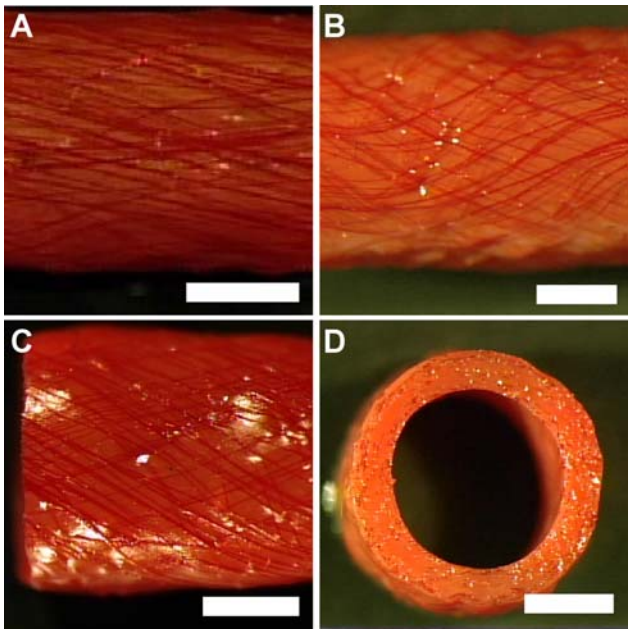

Figure 5.4. Vascular grafts fabricated with 15 (A), 22.5 (B), and 30° (C) collagen fiber layouts. Collagen fibers are stained red with with von Gieson. Cross-sectional view of a prototype (D). Scale bar 2 mm.

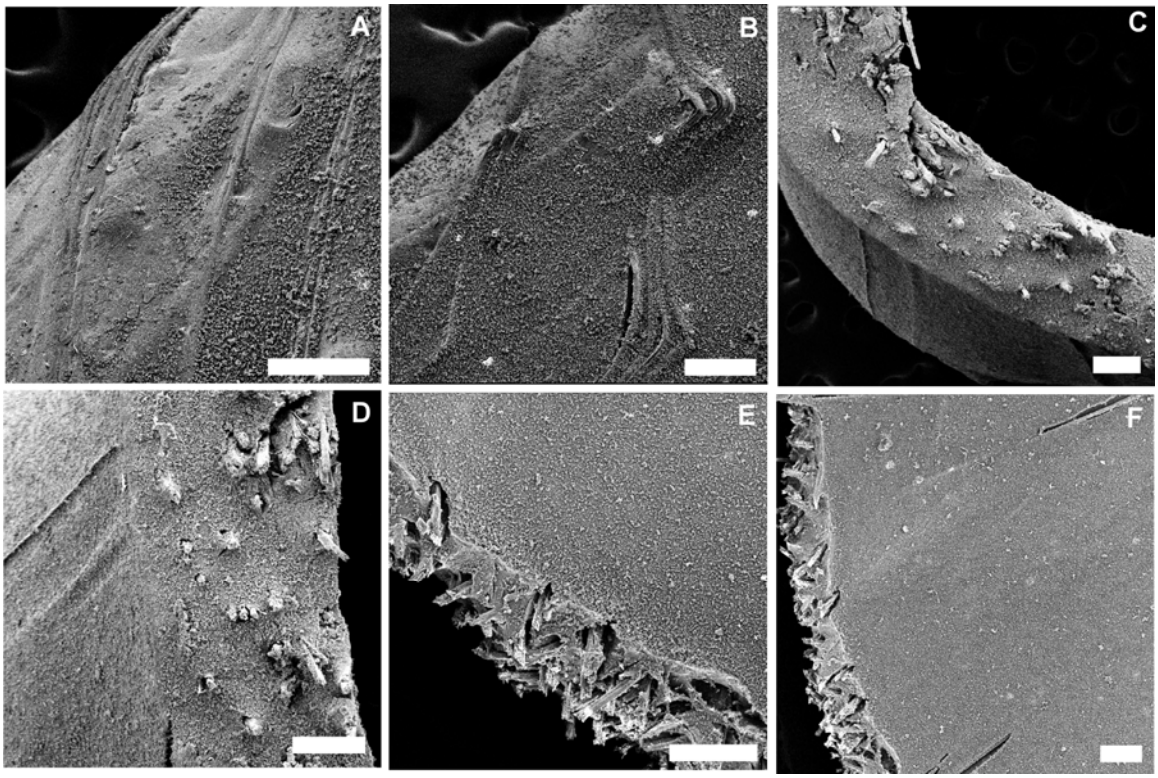

Figure 5.5. Scanning electron microscopy of a prototype of design 6. Synthetic collagen fibers appeared close to the surface of the graft exterior (A, B). Delineations or seams between the six layers of the wrapped film did not appear in the cross-sections of the graft wall (C, D). Compared to the graft exterior, collagen fibers did not appear as close to the surface of the lumen (E, F) with rare exception (grooves visible in F). Scale bar 200 μm.

Fiber architecture dictates mechanical behavior of composite vascular grafts.

Mechanical responses, including burst pressure, compliance, and suture retention strength are summarized in Table 5.3. Representative burst data is illustrated in Figure 5.6, and the relationship between mechanical behavior of the vascular graft and fiber angle and spacing is presented in Figure 5.7. Thermal annealing enhanced burst pressure and suture retention while reducing compliance, consistent with our prior observations that thermal annealing can increase the strength and Young's modulus of this protein polymer [135].

At a fixed fiber orientation (30°), decreasing average fiber spacing lead to increased fiber density with enhanced burst pressure and suture retention, but lower overall compliance. Likewise, with fiber spacing fixed and fiber angle increased, burst pressure and suture retention increased, but compliance decreased. Given the trade-offs of thermal annealing, fiber orientation, and fiber spacing, Design 6, with a fiber orientation of 22.5 and volume fraction of 7.3%, was selected as the best match for target mechanical properties.

Compliance matching in vascular bypass technology may reduce intimal hyperplasia and lead to increased patency [136-138]. Notably, arterial compliance varies broadly with age, sex, diet, smoking, and position in the vascular tree, ranging between 3 and 25 %/100 mm-Hg [139, 140]. This range highlights the advantage of platforms with the capacity to tailor compliance. Design 6 approached the compliance of several native arteries (Table 5.3).

Table 5.3. Mechanical Responses of Composite Vascular Grafts and Arteries

	Design Number or literature comparison	Burst Pressure (mm Hg)	Compliance (% / 100 mm Hg)	Suture Retention (g-f)
Current Study	1	239	4.8	35
	2	1409 ± 141	3.6 ± 1.8	121 ± 31
	2a	649 ± 74	8.4 ± 1.4	70 ± 18
	3	755 ± 227	8.4 ± 3.4	95 ± 23
	4	2760 ± 360	2.8 ± 0.5	192 ± 20
	5	893 ± 126	7.1 ± 1.2	124 ± 24
	6	1483 ± 143	5.1 ± 0.8	173 ± 4
	Target	> 1000	5 – 9	180
Engineered	Dahl, et al [87]	803 ± 105	3.5 ± 0.2	-
	L'Heureux, et al [85]	3468 ± 500	1.5 ± 0.3	162 ± 15
Native Arteries	Porcine common carotid artery [87]	3320 ± 413	18.7 ± 4.1	-
	Human common carotid artery [140]	-	18 - 26	-
	Human saphenous vein [85]	1680-2273	0.7-1.5	196 ± 2
	Human saphenous vein [141]	-	5.0 ± 6.7	-
	Human artery (range) [85]	2031-4225	4.5 – 6.2	200 ± 119
	Human common femoral artery [142]	-	8.3 ± 1.8	-
	Human proximal superficial femoral artery [142]	-	7.2 ± 1.5	-
	Human distal superficial femoral artery [142]	-	6.3 ± 0.8	-
	Human midgenicular popliteal artery [142]	-	6.1 ± 1.1	-
	Human radial artery [139]	-	3 – 4	-
	Human external iliac artery [141]	-	8.0 ± 5.9	-
	Dog femoral artery [143]	-	6.8	-

†Design 2a refers to design 2, fabricated without the thermal annealing step.

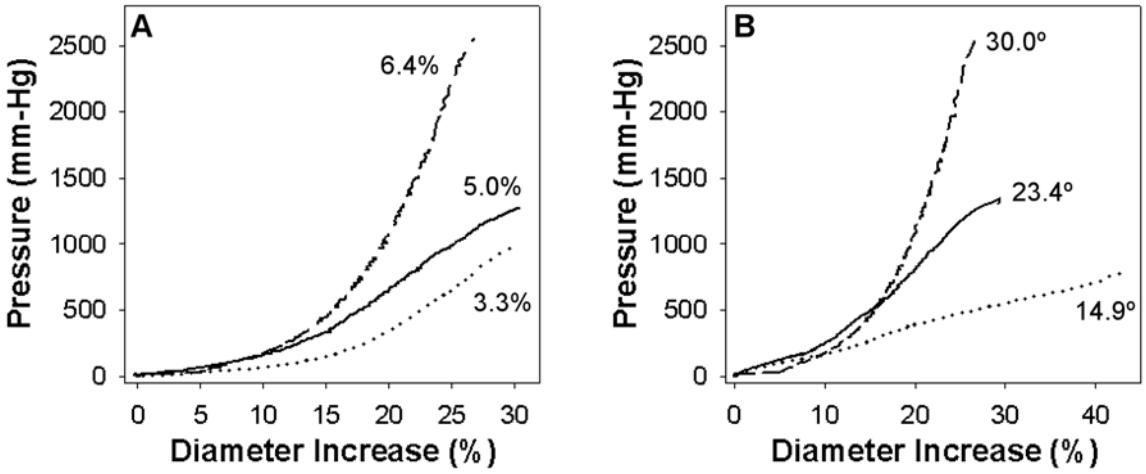

Figure 5.6. Representative pressure-diameter responses for composite vascular grafts. (A) Increasing fiber density at a fixed 30º fiber angle yielded prototypes with enhanced burst pressure. (B), Increasing fiber angle at a fixed fiber fraction of 6 to 7% yielded prototypes with decreased compliance.

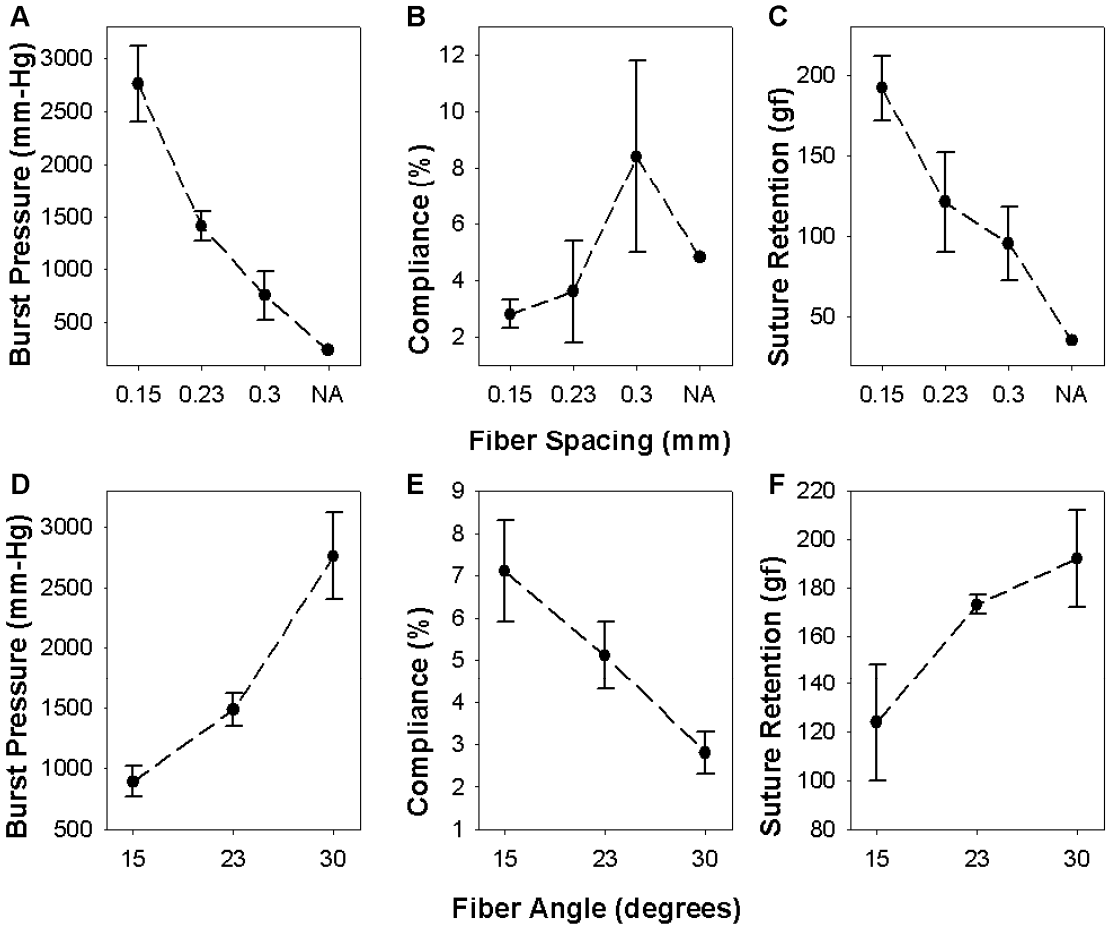

Figure 5.7. Dependence of suture retention, compliance, and bursting strength on fiber spacing (A, B, C) and angle (D, E, F). In plots A, B, and C, NA indicates data for design 1, without fiber reinforcement.

Burst pressures of native vein and artery (2000-3000+ mm-Hg) are often cited as benchmarks for bypass grafts although even in a hypertensive emergency, blood pressure rarely exceeds 240 mm-Hg. Instead of representing anticipated conditions in vivo, the high strength of native vessel probably reflects a proxy measurement for the capacity of native vessels to resist fatigue in the face of hypertension, arteriosclerosis, or aneurysm. In the case of bypass grafts, high bursting strength suggests a greater resistance to damage from suture-line stress, biaxial stress, and fatigue. Grafts designed to biodegrade and remodel require even greater bursting strength to compensate for the anticipated structural alterations. Here we selected 1000 mm-Hg as a target well above physiologic conditions, in consideration of data demonstrating the biostability of a physically crosslinked elastin-mimetic triblock even in the absence of chemical crosslinks [2].

Comparison of small-diameter vascular graft bursting to tensile failure of APPLES. The protein fiber composite grafts did not display the same set of failure patterns observed for APPLES in Chapter 3. Counter intuitively, APPLES designs without collagen fiber displayed higher ultimate tensile stress than fiber reinforced designs. This observation was explained by two factors. First, after the fiber network failed, the samples strained non-uniformly. The local strain and stress in the region of fiber failure was probably much higher than the overall strain in the sample, leading to failure at an artificially low level of measured ultimate tensile stress. Second, failure of the fibers left voids in the elastin analogue that may have caused failure at lower stress compared to the relatively flawless elastin analogue without fiber.

The protein fiber composite grafts displayed a more predictable trend, with lower fiber volume fraction consistently resulting in lower burst strength. The pattern of fiber

network yielding before graft burst was not observed; instead bursting and fiber failure were indistinguishable and apparently simultaneous. This difference is most likely caused by the greater compliance and reduced strength of the elastin analogue used in the vascular graft. Indeed, early graft prototypes were fabricated from the same molding conditions used to fabricate APPLES, and grafts without fiber burst at pressures around 900 mm Hg with compliances from 0.14 to 0.97 % / 100 mm Hg. In comparison, when the elastin analogue was molded according to the protocol in this chapter, burst pressure was 239 mm Hg and compliance was 4.8 % / 100 mm Hg. Therefore, the set of failure modes observed in Chapter 3 were not observed for the graft. These failure modes depended on separate fiber yielding and matrix failure, but in the case of the graft the elastin analogue was relatively weak and did not sustain additional loading after fiber network failure.

CONCLUSIONS

We constructed a series of protein-based, small-diameter vascular grafts and assessed the mechanical performance. The angle and density of fiber modulated the suture retention strength, bursting strength, and compliance of the grafts. Iterative adjustment of the fiber layout demonstrated the capacity to meet our mechanical targets, providing a platform from which the additional challenges of small-diameter vascular bypass can be addressed.

CHAPTER 6

CONCLUSIONS AND FUTURE DIRECTIONS

In the first phase of this project, the scalable production of synthetic collagen fiber, we presented a decoupled process for the spinning of collagen fiber and subsequent assembly of fibrillar ultrastructure. Fiber with an elliptical cross-section of 53 ± 14 by 21 ± 3 μm and an ultimate tensile strength of 90 ± 19 MPa was produced at 60 meters per hour from a sterile-filtered monomeric collagen solution. The spinning concentration, flowrate, and needle size could be adjusted to control the size of the spun fiber. Micro-differential scanning calorimetry demonstrated that the triple helical macromolecular structure was preserved after spinning. Second harmonic generation analysis suggested fibrillar structure and transmission electron microscopy confirmed the presence of banded, self-assembled fibrils of 53 ± 14 nm diameter, largely aligned with the fiber axis. Six week subcutaneous murine implants of glutaraldehyde crosslinked bundles demonstrated little degradation, but infiltration of macrophages. Uncrosslinked bundles present after six weeks but displayed more degradation, with macrophages localized largely around the bundle perimeter. Collectively, this study resulted in the scalable production of collagen fiber with a self-assembled fibrillar structure and sufficient strength for use in flexible composite tissue substitutes.

In Chapter 3, a strategy for the fabrication of anisotropic protein polymer lamellar elastic structures was developed. Sheets consisting of eight fiber-reinforced lamellae and exterior capping lamellae without fiber were constructed with controlled fiber orientation and volume fraction. Scanning electron microscopy, transmission electron microscopy, and digital volumetric imaging confirmed the structure of the flexible biocomposites.

The effect of fiber orientation and volume fraction on Young's Modulus, yield stress, ultimate tensile stress, strain-to-failure, and resilience was evaluated in uniaxial tension. The addition of collagen fiber and the alignment of fiber with the direction of applied force tended to increase Young's Modulus, resilience, and yield stress. This analysis demonstrated a semi-automated fabrication strategy for flexible biomaterial composites with defined resilience, modulus, and yield stress.

The development of a microcrimping method in Chapter 4 produced elastin-like protein polymer lamellae reinforced with undulating collagen fibers. Three potential profiles for the microridge crimping template were investigated, triangular, rectangular, and chamfered rectangular. The chamfered rectangle design was preferred due to the stability of the microridge against collapse, the relatively large overhead space for crimping, and the minimal damage caused by the fiber contacting region. The wavelength of fiber crimp in a hydrated lamella was 143 ± 5 μm. Alteration of the pre-extension parameter demonstrated the capacity to adjust the degree of crimping from 3.1% to 9.4%, corresponding to mechanical modulus transitions at 4.6% and 13.3% strain. Cyclic mechanical loading of up to 1000 cycles did not substantially alter the crimp morphology of embedded fibers. This report represents the first process for microcrimping of synthetic collagen fibers that we are aware of, and demonstrates the capacity of elastin-like protein embedded fiber arrays to display a defined mechanical transition point response.

Chapter 5 described the application of the materials and fabrication strategies developed above to the generation of small diameter vascular grafts. Six prototype vascular graft designs were fabricated with an inner diameter of 4 mm, wall thicknesses

of 0.9 mm, fiber volume fractions ranging from 3 to 7%, and fiber orientations of 15, 22.5, and 30º relative to the axial direction. The structure of the graft wall was examined with scanning electron microscopy. A system to perform pressure-diameter analysis at defined levels of axial force was developed and implemented to study the effects of fiber volume fraction and orientation on graft mechanics. Different design variations displayed burst pressures as high as 2760 ± 360 mm Hg, compliance as high as 8.4 ± 1.4 % / 100 mm Hg, and suture retention strengths up to 192 ± 20 g-f. The optimal design, with a fiber orientation of 22.5º and fiber volume fraction of 7.3%, simultaneously satisfied target mechanical properties with suture retention strength of 173 ± 4 g-f, bursting strength of 1483 ± 143 mm Hg, and compliance of 5.1 ± 0.8 %/100 mm Hg .

In summary, the design and fabrication of flexible biocomposites for soft tissue substitution has been investigated. A new technique for the scalable production of synthetic collagen fiber was introduced. Recombinant, elastin-like protein polymer lamellae were reinforced with defined densities and orientations of collagen fiber and the capacity to tailor the Young's modulus, resilience, compliance, bursting strength and other mechanical properties of multilamellar sheet and tube structures was demonstrated. A novel approach to generate microcrimped collagen fiber arrays was developed and the mechanics of these structures in were analyzed in uniaxial tension. Collectively, this research represents significant progress toward the design and fabrication of synthetic extracellular matrices with defined mechanical properties.

FUTURE DIRECTIONS

Several additional studies may enhance the concepts and prototypes developed in this thesis. Regarding the synthetic collagen fiber, these include:

- *Increased production rate.* Although the rate of fiber production facilitated the fabrication of the composite structures in Chapters 3 to 5, faster production would be of practical benefit. It may be possible to enhance production rate by increasing the flowrates of collagen and wet spinning buffer during fiber spinning, using a larger diameter coagulation column to reduce clogging, and recycling the wet spinning buffer.
- *Assembly of larger collagen fibrils.* Studies to adjust the FIB composition or treatment time to elevate fibril diameter or length could improve the mechanical performance of the fiber [144]. Alternatives to the use of transmission electron microscopy to assess fibril structure, such as second harmonic generation or confocal reflectance microscopy, would aid these studies.
- *Assembly of collagen fibrils prior to fiber spinning.* In the current system, a solution of collagen monomers is spun into fiber and then incubated for 48 hr to motivate the assembly of banded collagen fibrils. An alternative approach is to trigger the assembly of fibrils before forming the collagen into a fiber, and then wet spin a dispersion of fibrils instead of collagen monomers. This would increase the production rate because the 48 hr incubation step could be avoided, and may also facilitate the spinning of fiber consisting of fibrils with improved length or diameter.

- *More biocompatible crosslinking chemistry.* The use of glutaraldehyde as a crosslinking agent limits the biocompatibility of the fiber. Alternative crosslinking agents could be sought, although this area has been widely explored, and a compromise between strength and biocompatibility may be required.

There are also several areas for future work regarding the anisotropic protein polymer lamellar elastin sheets (APPLES) presented in Chapter 3:

- *Alternative processing conditions for the elastin analogue to enhance compliance and resilience.* The fabrication conditions developed in Chapter 5, including molding of the elastin protein polymer between polycarbonate or glass surfaces instead of absorbent polyurethane, and thermal annealing, could be applied to enhance the compliance and resilience of the elastin analogue. These processing conditions may also lower the strength of the elastin analogue. The volume fraction of collagen fiber could be raised to enhance the resilience and strength of the sheet.
- *Increased ultimate tensile stress.* The APPLES were stronger than many soft tissues, but notably weaker than aortic heart valve leaflet or the crosslinked bovine pericardium used in bioprosthetic valves. Increased fiber volume fractions or alternative elastin analogues could be explored to enhance strength.
- *Addition of living cells or drugs.* Further investigation may also establish the potential for the materials to serve as a cell scaffolds or to release growth factors or other drugs.

Opportunities to improve the microcrimping concept presented in Chapter 4 include:

- *Enhanced strength.* Although the microcrimped fiber lamella matched or exceeded the strength of several native tissues, future research could include an analysis of the tensile failure of the microcrimped lamella. The tendency of the ultimate tensile strength to decrease with increasing degree of crimp was not explained by the current research. The reduced ultimate stress may be due to microridge contact. Notably, the strain-to-failure values of the microcrimped lamellae were in accordance with expectations, but the Young's modulus after the transition point strain of was below expectations.
- *Multilamellar crimped structures.* Although crimped fiber lamellae have been created following the lamination protocol described in Chapter 3, the mechanics and structure of these laminates has not been investigated. Additionally, the generation of multilamellar crimped structures provides the opportunity to investigate the combined effect of crimp and fiber angle on tensile mechanics.

The application of advanced fiber reinforcing strategies or an alternative elastin analogue could further enhance the vascular grafts developed in Chapter 5:

- *Advanced fiber reinforcing strategies*. In addition to the fiber pattern employed in Chapter 5, collagen could be added as microcrimped fiber, non-continuous fiber, or 2D collagen fiber layouts generated by alternative means. These alternatives may lead to further optimization of compliance and strength.

REFERENCES

1. Wright, E., et al., *Thermoplastic elastomer hydrogels via self-assembly of an elastim-mimetic triblock polypeptide.* Advanced Functional Materials, 2002. **12**(2): p. 149-154.

2. Sallach, R., *Recombinant Elastin-Mimetic Protein Polymers as Design Elements for an Arterial Substitute*, in *Wallace H. Coulter Department of Biomedical Engineering*. 2008, Georgia Institute of Technology: Atlanta.

3. Nagapudi, K., et al., *Viscoelastic and mechanical behavior of recombinant protein elastomers.* Biomaterials, 2005. **26**(23): p. 4695-706.

4. Sallach, R.E., et al., *Micelle density regulated by a reversible switch of protein secondary structure.* J Am Chem Soc, 2006. **128**(36): p. 12014-9.

5. Nagapudi, K., et al., *Protein-Based Thermoplastic Elastomers.* Macromolecules, 2005. **38**: p. 345-354.

6. Jordan, S.W., et al., *The effect of a recombinant elastin-mimetic coating of an ePTFE prosthesis on acute thrombogenicity in a baboon arteriovenous shunt.* Biomaterials, 2007. **28**(6): p. 1191-7.

7. Silver, F.H., I. Horvath, and D.J. Foran, *Viscoelasticity of the vessel wall: the role of collagen and elastic fibers.* Crit Rev Biomed Eng, 2001. **29**(3): p. 279-301.

8. Milnor, W., *Hemodynamics*. 1982, Baltimore: Williams and Wilkins. 390.

9. Gosline, J.M. and R.E. Shadwick, *The mechanical properties of fin whale arteries are explained by novel connective tissue designs.* J Exp Biol, 1996. **199**(Pt 4): p. 985-97.

10. Wolinsky, H. and S. Glagov, *Nature of species differences in the medial distribution of aortic vasa vasorum in mammals.* Circ Res, 1967. **20**(4): p. 409-21.

11. Clark, J.M. and S. Glagov, *Transmural organization of the arterial media. The lamellar unit revisited.* Arteriosclerosis, 1985. **5**(1): p. 19-34.

12. Wolinsky, H. and S. Glagov, *A lamellar unit of aortic medial structure and function in mammals.* Circ Res, 1967. **20**(1): p. 99-111.

13. Wolinsky, H. and S. Glagov, *Structural Basis for the Static Mechanical Properties of the Aortic Media.* Circ Res, 1964. **14**: p. 400-13.

14. O'Connell, M.K., et al., *The three-dimensional micro- and nanostructure of the aortic medial lamellar unit measured using 3D confocal and electron microscopy imaging.* Matrix Biol, 2008. **27**(3): p. 171-81.

15. Cataloglu, A., R.E. Clark, and P.L. Gould, *Stress analysis of aortic valve leaflets with smoothed geometrical data.* J Biomech, 1977. **10**(3): p. 153-8.

16. Missirlis, Y. and C. Armeniades, *Ultrastructure of the human artic valve.* Acta Anatomica, 1977. **98**: p. 199-205.

17. Thubrikar, M., *The Aortic Valve*. 1990, Boca Raton: CRC Press, Inc. 221.

18. Vesely, I., *The role of elastin in aortic valve mechanics.* Journal of Biomechanics, 1998. **31**: p. 115-123.

19. Schoen, F.J. and R.J. Levy, *Founder's Award, 25th Annual Meeting of the Society for Biomaterials, perspectives. Providence, RI, April 28-May 2, 1999. Tissue heart valves: current challenges and future research perspectives.* J Biomed Mater Res, 1999. **47**(4): p. 439-65.

20. Vesely, I., *The evolution of bioprosthetic heart valve design and its impact on durability.* Cardiovasc Pathol, 2003. **12**(5): p. 277-86.

21. Vesely, I., *The role of elastin in aortic valve mechanics.* J Biomech, 1998. **31**(2): p. 115-23.

22. Vesely, I., A. Lozon, and E. Talman, *Is zero-pressure fixation of bioprosthetic valves truly stress free?* J Thorac Cardiovasc Surg, 1993. **106**(2): p. 288-98.

23. Vesely, I., D. Boughner, and T. Song, *Tissue buckling as a mechanism of bioprosthetic valve failure.* Ann Thorac Surg, 1988. **46**(3): p. 302-8.

24. Broom, N.D., *The stress/strain and fatigue behaviour of glutaraldehyde preserved heart-valve tissue.* J Biomech, 1977. **10**(11/12): p. 707-24.

25. Kielty, C., I. Hopkinson, and M. Grant, *Collagen: the collagen family: structure, assembly, and organization in the extracellular matrix*, in *Connective tissue and its heritable disorders. Molecular, genetic, and medical aspects*, P. Royce and B. Steinmann, Editors. 1993, Wiley-Liss, Inc.: New York. p. 103-147.

26. Friess, W., *Collagen--biomaterial for drug delivery.* Eur J Pharm Biopharm, 1998. **45**(2): p. 113-36.

27. Silver, F.H. and R.L. Trelstad, *Type I collagen in solution. Structure and properties of fibril fragments.* J Biol Chem, 1980. **255**(19): p. 9427-33.

28. Fagien, S., *Facial soft-tissue augmentation with injectable autologous and allogeneic human tissue collagen matrix (autologen and dermalogen).* Plast Reconstr Surg, 2000. **105**(1): p. 362-73; discussion 374-5.

29. Yang, C., et al., *The application of recombinant human collagen in tissue engineering.* BioDrugs, 2004. **18**(2): p. 103-19.

30. Lynn, A.K., I.V. Yannas, and W. Bonfield, *Antigenicity and immunogenicity of collagen.* J Biomed Mater Res B Appl Biomater, 2004. **71**(2): p. 343-54.

31. Sabelman, E., *Biology, Biotechnology, and Biocompatibility of Collagen*, in *Biocompatibility of Tissue Analogues*, D. Williams, Editor. 1985, CRC Press: Boca Raton, FL. p. 27-66.

32. Ichii, T., et al., *Fibrillar collagen specifically regulates human vascular smooth muscle cell genes involved in cellular responses and the pericellular matrix environment.* Circ Res, 2001. **88**(5): p. 460-7.

33. Chu, C., *Chemical structure and manufacturing processes*, in *Wound closure biomaterials and devices*, C. Chu, J. Fraunhofer, and H. Greisler, Editors. 1996, CRC Press: Boca Raton, FL

34. Hirko, M., et al., *Biological properties of suture materials*, in *Wound closure biomaterials and devices*, C. Chu, J. Fraunhofer, and H. Greisler, Editors. 1996, CRC Press: Boca Raton, FL

35. Salo, T. and D. Waugh, Preparation of collagenous materials, USPTO 2598608, issued 1946

36. Griset, E., et al., Method of producing a collagen strand, 3114593, issued 1964

37. Reynolds, B.L., *Reconstituted collagen and chromic catgut suture for colon anastomoses in dogs.* JAMA, 1966. **195**(10): p. 807-12.

38. Kato, Y.P., et al., *Mechanical properties of collagen fibres: a comparison of reconstituted and rat tail tendon fibres.* Biomaterials, 1989. **10**(1): p. 38-42.

39. Wang, M.C., G.D. Pins, and F.H. Silver, *Collagen fibres with improved strength for the repair of soft tissue injuries.* Biomaterials, 1994. **15**(7): p. 507-12.

40. Pins, G., et al., *Effects of static axial strain on the tensile properties and failure mechanisms of self-assembled collagen fibers.* J Appl Polym Sci, 1997. **63**: p. 1429-1440.

41. Zeugolis, D.I., R.G. Paul, and G. Attenburrow, *Factors influencing the properties of reconstituted collagen fibers prior to self-assembly: Animal species and collagen extraction method.* J Biomed Mater Res A, 2007.

42. Pins, G.D., et al., *Self-assembly of collagen fibers. Influence of fibrillar alignment and decorin on mechanical properties.* Biophys J, 1997. **73**(4): p. 2164-72.

43. Kato, Y.P. and F.H. Silver, *Formation of continuous collagen fibres: evaluation of biocompatibility and mechanical properties.* Biomaterials, 1990. **11**(3): p. 169-75.

44. Cavallaro, J., P. Kemp, and K. Kraus, *Collagen fabrics as biomaterials.* Biotechnology and Bioengineering, 1994. **43**: p. 781-791.

45. Fofonoff, T. and E. Bell, Apparatus and method for spinning and processing collagen fiber, USPTO 5562946, issued 1996

46. Silver, F.H. and R.L. Trelstad, *Type I collagen in solution-structure and properties of fibril fragments.* Journal of Biological Chemistry, 1980. **255**: p. 9427-33.

47. Pins, G.P., et al., *Self-assembly of collagen fibers. Influence of fibrillar alignment and decorin on mechanical properties.* Biophysical Journal, 1997. **73**: p. 2164-2172.

48. Pins, G.P., et al., *Effects of static axial strain on the tensile properties and failure mechanisms of self-assembled collagen fibers.* Journal of Applied Polymer Science, 1997. **63**: p. 1429-1440.

49. Zeugolis, D.I., G.R. Paul, and G. Attenburrow, *Cross-linking of extruded collagen fibers-A biomimetic three-dimensional scaffold for tissue engineering applications.* J Biomed Mater Res A, 2008.

50. Zeugolis, D.I., G.R. Paul, and G. Attenburrow, *Engineered extruded collagen fibers for biomedical applications.* J Appl Polym Sci, 2008. **108**: p. 2886-2894.

51. Zeugolis, D.I., R.G. Paul, and G. Attenburrow, *Post-self-assembly experimentation on extruded collagen fibres for tissue engineering applications.* Acta Biomater, 2008.

52. Koster, S., et al., *An in situ study of collagen self-assembly processes.* Biomacromolecules, 2008. **9**(1): p. 199-207.

53. Zeugolis, D.I., et al., *Electro-spinning of pure collagen nano-fibres - just an expensive way to make gelatin?* Biomaterials, 2008. **29**(15): p. 2293-305.

54. Leikina, E., et al., *Type I collagen is thermally unstable at body temperature.* Proc Natl Acad Sci U S A, 2002. **99**(3): p. 1314-8.

55. Wallace, D.G., et al., *Multiple denaturational transitions in fibrillar collagen.* Biopolymers, 1986. **25**(10): p. 1875-95.

56. Campagnola, P.J. and L.M. Loew, *Second-harmonic imaging microscopy for visualizing biomolecular arrays in cells, tissues and organisms.* Nat Biotechnol, 2003. **21**(11): p. 1356-60.

57. Brown, E., et al., *Dynamic imaging of collagen and its modulation in tumors in vivo using second-harmonic generation.* Nat Med, 2003. **9**(6): p. 796-800.

58. Zipfel, W.R., et al., *Live tissue intrinsic emission microscopy using multiphoton-excited native fluorescence and second harmonic generation.* Proc Natl Acad Sci U S A, 2003. **100**(12): p. 7075-80.

59. Chu, S., et al., *Thickness dependence of optical second harmonic generation in collagen fibrils.* Optics Express, 2007. **15**(19): p. 12005-12010.

60. Williams, R.M., W.R. Zipfel, and W.W. Webb, *Interpreting second-harmonic generation images of collagen I fibrils.* Biophys J, 2005. **88**(2): p. 1377-86.

61. Parry, D.A. and A.S. Craig, *Quantitative electron microscope observations of the collagen fibrils in rat-tail tendon.* Biopolymers, 1977. **16**(5): p. 1015-31.

62. Cavallaro, J., Method of strength enhancement of collagen constructs, USPTO 5178012, issued 1998

63. Guido, S. and R.T. Tranquillo, *A methodology for the systematic and quantitative study of cell contact guidance in oriented collagen gels. Correlation of fibroblast orientation and gel birefringence.* J Cell Sci, 1993. **105 (Pt 2)**: p. 317-31.

64. Cheng, X., et al., *An electrochemical fabrication process for the assembly of anisotropically oriented collagen bundles.* Biomaterials, 2008. **29**(22): p. 3278-88.

65. Guo, C. and L.J. Kaufman, *Flow and magnetic field induced collagen alignment.* Biomaterials, 2007. **28**(6): p. 1105-14.

66. Hughes, K., T. Hutson, and J. Fink, Collagen Orientation, 4,544,516, issued 1985

67. Amyot, F., et al., *Thin films of oriented collagen fibrils for cell motility studies.* J Biomed Mater Res B Appl Biomater, 2008. **86B**(2): p. 438-43.

68. Lanfer, B., et al., *Aligned fibrillar collagen matrices obtained by shear flow deposition.* Biomaterials, 2008. **29**(28): p. 3888-95.

69. Shi, Y. and I. Vesely, *Fabrication of mitral valve chordae by directed collagen gel shrinkage.* Tissue Eng, 2003. **9**(6): p. 1233-42.

70. Shi, Y., L. Rittman, and I. Vesely, *Novel geometries for tissue-engineered tendonous collagen constructs.* Tissue Eng, 2006. **12**(9): p. 2601-9.

71. L'Heureux, N., et al., *In vitro construction of a human blood vessel from cultured vascular cells: a morphologic study.* J Vasc Surg, 1993. **17**(3): p. 499-509.

72. Hirai, J., et al., *Highly oriented, tubular hybrid vascular tissue for a low pressure circulatory system.* ASAIO J, 1994. **40**(3): p. M383-8.

73. Kanda, K. and T. Matsuda, *Mechanical stress-induced orientation and ultrastructural change of smooth muscle cells cultured in three-dimensional collagen lattices.* Cell Transplant, 1994. **3**(6): p. 481-92.

74. Law, J.K., et al., *An evaluation of purified reconstituted type 1 collagen fibers.* J Biomed Mater Res, 1989. **23**(9): p. 961-77.

75. Gentleman, E., et al., *Mechanical characterization of collagen fibers and scaffolds for tissue engineering.* Biomaterials, 2003. **24**(21): p. 3805-13.

76. Kato, Y.P., et al., *Regeneration of Achilles tendon with a collagen tendon prosthesis. Results of a one-year implantation study.* J Bone Joint Surg Am, 1991. **73**(4): p. 561-74.

77. Dunn, M.G., P.N. Avasarala, and J.P. Zawadsky, *Optimization of extruded collagen fibers for ACL reconstruction.* J Biomed Mater Res, 1993. **27**(12): p. 1545-52.

78. Khouw, I.M., et al., *The foreign body reaction to a biodegradable biomaterial differs between rats and mice.* J Biomed Mater Res, 2000. **52**(3): p. 439-46.

79. Roach, M.R. and A.C. Burton, *The reason for the shape of the distensibility curves of arteries.* Can J Biochem Physiol, 1957. **35**(8): p. 681-90.

80. Gosline, J., et al., *Elastic proteins: biological roles and mechanical properties.* Philos Trans R Soc Lond B Biol Sci, 2002. **357**(1418): p. 121-32.

81. Broom, N.D., *Simultaneous morphological and stress-strain studies of the fibrous components in wet heart valve leaflet tissue.* Connect Tissue Res, 1978. **6**(1): p. 37-50.

82. Sacks, M.S. and A.P. Yoganathan, *Heart valve function: a biomechanical perspective.* Philos Trans R Soc Lond B Biol Sci, 2007. **362**(1484): p. 1369-91.

83. Poh, M., et al., *Blood vessels engineered from human cells.* Lancet, 2005. **365**(9477): p. 2122-4.

84. Weinberg, C.B. and E. Bell, *A blood vessel model constructed from collagen and cultured vascular cells.* Science, 1986. **231**(4736): p. 397-400.

85. L'Heureux, N., et al., *Human tissue-engineered blood vessels for adult arterial revascularization.* Nat Med, 2006. **12**(3): p. 361-5.

86. Long, J.L. and R.T. Tranquillo, *Elastic fiber production in cardiovascular tissue-equivalents.* Matrix Biol, 2003. **22**(4): p. 339-50.

87. Dahl, S.L., et al., *Mechanical properties and compositions of tissue engineered and native arteries.* Ann Biomed Eng, 2007. **35**(3): p. 348-55.

88. Abramoff, M., P. Magelhaes, and S. Ram, *Image Processing with ImageJ.* Biophotonics International, 2004. **11**(7): p. 36-42.

89. Hermanson, G.T., *Bioconjugate Techniques*. 1 ed. 1996, San Diego, CA: Academic Press.

90. Chou, T., *Microsctructural Design of Fiber Composites*. 1992, Cambridge: Cambridge University Press.

91. Sekitani, T., et al., *A rubberlike stretchable active matrix using elastic conductors.* Science, 2008. **321**(5895): p. 1468-72.

92. Vaia, R. and J. Baur, *Materials science. Adaptive composites.* Science, 2008. **319**(5862): p. 420-1.

93. Peel, L., *Fabrication and Mechanics of Fiber Reinforced Elastomers*, in *Department of Mechanical Engineering*. 1998, Brigham Young University: Provo, UT. p. 210.

94. Chou, T. and K. Takahashi, *Non-linear elastic behaviour of flexible fibre composites.* Composites, 1987. **18**(1): p. 25-34.

95. Mallick, P., *Fiber-reinforced composites: materials, manufacturing, and design*. 3rd ed. 2008, Boca Raton, FL: CRC Press.

96. Korenkov, M., et al., *Biomechanical and morphological types of the linea alba and its possible role in the pathogenesis of midline incisional hernia.* Eur J Surg, 2001. **167**(12): p. 909-14.

97. Gilbert, T.W., et al., *Fiber kinematics of small intestinal submucosa under biaxial and uniaxial stretch.* J Biomech Eng, 2006. **128**(6): p. 890-8.

98. Sacks, M.S. and D.C. Gloeckner, *Quantification of the fiber architecture and biaxial mechanical behavior of porcine intestinal submucosa.* J Biomed Mater Res, 1999. **46**(1): p. 1-10.

99. Gathercole, L.J. and A. Keller, *Crimp morphology in the fibre-forming collagens.* Matrix, 1991. **11**(3): p. 214-34.

100. Kubo, H., et al., *Creation of myocardial tubes using cardiomyocyte sheets and an in vitro cell sheet-wrapping device.* Biomaterials, 2007. **28**(24): p. 3508-16.

101. Diamant, J., et al., *Collagen; ultrastructure and its relation to mechanical properties as a function of ageing.* Proc R Soc Lond B Biol Sci, 1972. **180**(60): p. 293-315.

102. Canham, P.B., et al., *Effect of pressure on circumferential order of adventitial collagen in human brain arteries.* Can J Physiol Pharmacol, 1992. **70**(2): p. 296-305.

103. Berkovitz, B.K., *Collagen crimping in the intra-articular disc and articular surfaces of the human temporomandibular joint.* Arch Oral Biol, 2000. **45**(9): p. 749-56.

104. de Campos Vidal, B., *Image analysis of tendon helical superstructure using interference and polarized light microscopy.* Micron, 2003. **34**(8): p. 423-32.

105. Freed, A.D. and T.C. Doehring, *Elastic model for crimped collagen fibrils.* J Biomech Eng, 2005. **127**(4): p. 587-93.

106. Hilbert, S.L., et al., *Simultaneous assessment of bioprosthetic heart valve biomechanical properties and collagen crimp length.* J Biomed Mater Res, 1996. **31**(4): p. 503-9.

107. Dahms, S.E., et al., *Composition and biomechanical properties of the bladder acellular matrix graft: comparative analysis in rat, pig and human.* Br J Urol, 1998. **82**(3): p. 411-9.

108. Sodian, R., et al., *Early in vivo experience with tissue-engineered trileaflet heart valves.* Circulation, 2000. **102**(19 Suppl 3): p. III22-9.

109. Mohan, D. and J.W. Melvin, *Failure properties of passive human aortic tissue. I--uniaxial tension tests.* J Biomech, 1982. **15**(11): p. 887-902.

110. Zilla, P., D. Bezuidenhout, and P. Human, *Prosthetic vascular grafts: wrong models, wrong questions and no healing.* Biomaterials, 2007. **28**(34): p. 5009-27.

111. Heyligers, J.M., et al., *Improving small-diameter vascular grafts: from the application of an endothelial cell lining to the construction of a tissue-engineered blood vessel.* Ann Vasc Surg, 2005. **19**(3): p. 448-56.

112. Kannan, R.Y., et al., *Current status of prosthetic bypass grafts: a review.* J Biomed Mater Res B Appl Biomater, 2005. **74**(1): p. 570-81.

113. Xue, L. and H.P. Greisler, *Biomaterials in the development and future of vascular grafts.* J Vasc Surg, 2003. **37**(2): p. 472-80.

114. Wengerter, K. and H. Dardik, *Biological vascular grafts.* Semin Vasc Surg, 1999. **12**(1): p. 46-51.

115. Sciacca, V., G. Walter, and H.M. Becker, *Biogenic grafts in arterial surgery--long-term results (I. The homologous vein--II. The modified heterologous bovine carotid artery--III. The human umbilical vein).* Thorac Cardiovasc Surg, 1984. **32**(3): p. 157-64.

116. Dardik, H., *The second decade of experience with the umbilical vein graft for lower-limb revascularization.* Cardiovasc Surg, 1995. **3**(3): p. 265-9.

117. Rosenburg, N., et al., *Tanned cllagen arterial prosthesis of bovine carotid origin in man. Preliminary studies of enzyme-treated heterografts.* Annals of Surgery, 1966. **164**(2): p. 247-256.

118. Hurt, A.V., et al., *Bovine carotid artery heterografts versus polytetrafluoroethylene grafts. A prospective, randomized study.* Am J Surg, 1983. **146**(6): p. 844-7.

119. Silver, F.H., P.B. Snowhill, and D.J. Foran, *Mechanical behavior of vessel wall: a comparative study of aorta, vena cava, and carotid artery.* Ann Biomed Eng, 2003. **31**(7): p. 793-803.

120. Leidner, J., et al., *A novel process for the manufacturing of porous grafts: process description and product evaluation.* J Biomed Mater Res, 1983. **17**(2): p. 229-47.

121. Hellener, G., D. Cohn, and G. Marom, *Elastic response of filament wound arterial prostheses under internal pressure.* Biomaterials, 1994. **15**(14): p. 1115-21.

122. Teo, W. and S. Ramakrishna, *A review on electrospinning design and nanofibre assemblies.* Nanotechnology, 2006. **17**: p. R89–R106.

123. Smith, M.J., et al., *Suture-reinforced electrospun polydioxanone-elastin small-diameter tubes for use in vascular tissue engineering: a feasibility study.* Acta Biomater, 2008. **4**(1): p. 58-66.

124. Tomaszewski, W. and M. Szadkowski, *Investigation of Electrospinning with the Use of a Multi-jet Electrospinning Head.* Fibers and Textiles in Eastern Europe, 2005. **13**(4): p. 22-26.

125. Li, M., et al., *Co-electrospun poly(lactide-co-glycolide), gelatin, and elastin blends for tissue engineering scaffolds.* J Biomed Mater Res A, 2006. **79**(4): p. 963-73.

126. Buttafoco, L., et al., *Electrospinning collagen and elastin for tissue engineering small diameter blood vessels.* J Control Release, 2005. **101**(1-3): p. 322-4.

127. Buttafoco, L., et al., *Electrospinning of collagen and elastin for tissue engineering applications.* Biomaterials, 2006. **27**(5): p. 724-34.

128. Sell, S.A., et al., *Electrospun polydioxanone-elastin blends: potential for bioresorbable vascular grafts.* Biomed Mater, 2006. **1**(2): p. 72-80.

129. Huang, L., et al., *Engineered collagen-PEO nanofibers and fabrics.* J Biomater Sci Polym Ed, 2001. **12**(9): p. 979-93.

130. Barocas, V.H., T.S. Girton, and R.T. Tranquillo, *Engineered alignment in media equivalents: magnetic prealignment and mandrel compaction.* J Biomech Eng, 1998. **120**(5): p. 660-6.

131. Doi, K., Y. Nakayama, and T. Matsuda, *Novel compliant and tissue-permeable microporous polyurethane vascular prosthesis fabricated using an excimer laser ablation technique.* J Biomed Mater Res, 1996. **31**(1): p. 27-33.

132. Sonoda, H., et al., *Coaxial double-tubular compliant arterial graft prosthesis: time-dependent morphogenesis and compliance changes after implantation.* J Biomed Mater Res A, 2003. **65**(2): p. 170-81.

133. L'Heureux, N., et al., *A completely biological tissue-engineered human blood vessel.* FASEB J, 1998. **12**(1): p. 47-56.

134. Hinds, M.T., et al., *Development of a reinforced porcine elastin composite vascular scaffold.* J Biomed Mater Res A, 2006. **77**(3): p. 458-69.

135. Sallach, R., et al., *A permanent change in protein mechanical responses can be produced by thermally induced microdomain mixing* Submitted as a Research Article to Journal of Biomaterials Science: Polymer Edition, 2008.

136. Bassiouny, H.S., et al., *Anastomotic intimal hyperplasia: mechanical injury or flow induced.* J Vasc Surg, 1992. **15**(4): p. 708-16; discussion 716-7.

137. Zarins, C.K. and D.P. Giddens, *Relationship between anastomotic hemodynamics and intimal thickening.* J Vasc Surg, 1991. **13**(5): p. 738-40.

138. Sottiurai, V.S., et al., *Distal anastomotic intimal hyperplasia: histopathologic character and biogenesis.* Ann Vasc Surg, 1989. **3**(1): p. 26-33.

139. Hayoz, D., et al., *Conduit artery compliance and distensibility are not necessarily reduced in hypertension.* Hypertension, 1992. **20**(1): p. 1-6.

140. Juonala, M., et al., *Risk factors identified in childhood and decreased carotid artery elasticity in adulthood: the Cardiovascular Risk in Young Finns Study.* Circulation, 2005. **112**(10): p. 1486-93.

141. Tai, N.R., et al., *Compliance properties of conduits used in vascular reconstruction.* Br J Surg, 2000. **87**(11): p. 1516-24.

142. Tai, N.R., et al., *In vivo femoropopliteal arterial wall compliance in subjects with and without lower limb vascular disease.* J Vasc Surg, 1999. **30**(5): p. 936-45.

143. Sonoda, H., et al., *Compliant design of artificial graft: compliance determination by new digital X-ray imaging system-based method.* J Biomed Mater Res, 2002. **60**(1): p. 191-5.

144. Christiansen, D.L., E.K. Huang, and F.H. Silver, *Assembly of type I collagen: fusion of fibril subunits and the influence of fibril diameter on mechanical properties.* Matrix Biol, 2000. **19**(5): p. 409-20.